Title
Modeling Ferroelectric Materials and Synthetic Jet Actuators

Author
Sheng, Michael

Publication Date
2023

Peer reviewed|Thesis/dissertation

UNIVERSITY OF CALIFORNIA

Los Angeles

Modeling Ferroelectric Materials and Synthetic Jet Actuators

A dissertation submitted in partial satisfaction of the

requirements for the degree Doctor of Philosophy

in Mechanical Engineering

by

Michael Thomas Sheng

2023

ABSTRACT OF THE DISSERTATION

Modeling Ferroelectric Materials and Synthetic Jet Actuators

by

Michael Thomas Sheng

Doctor of Philosophy in Mechanical Engineering

University of California, Los Angeles, 2023

Professor Gregory P. Carman, Co-Chair

Professor Christopher S. Lynch, Co-Chair

Ferroelectric materials like $BaTiO_3$ and PZT are known for their ability to strongly couple electrical and mechanical energy, which makes them widely used as transducers, sensors, or actuators. There is an ongoing search for better performing materials to optimize device performance. Single crystal relaxor ferroelectrics like PMN-PT and PIN-PMN-PT near the morphotropic phase boundary (MPB) have garnered attention for their large electromechanical properties relative to PZT. A better understanding of the underlying physics will help in the search for next generation materials and optimizing device design. This dissertation focuses on modeling: 1) phase transformations in ferroelectrics materials and 2) novel piezoelectric synthetic jet actuators (SJAs). Ferroelectric material models are known to significantly overpredict the coercive field. This is attributed to a combination of domain wall motion and the presence of metastable wells in the Landau-Devonshire energy function. These metastable wells also prevent current models from capturing important phase transition behavior. An improved energy function for

rhombohedral PIN-PMN-PT near the MPB with better thermodynamic stability was developed and used to investigate the effect energy fluctuations have on phase transformations. Results showed that accounting for fluctuations produced closer predictions to experimental observations, including the lower coercive field for switching and the forward and reverse phase transformations during loading and unloading. Two methods to implement these fluctuations in phase field models were assessed. Static local fields were preferred over time-varying noise due to convergence and reproducibility concerns with the latter. For SJAs, current models are unable to efficiently and accurately model novel SJAs that deviate significantly from an ideal Helmholtz resonator. A hybrid finite-element and lumped-element modeling approach was developed to provide more flexibility to explore novel material and geometric designs. This hybrid model reduced reliance on fitting parameters through FEM and a formula to estimate the loss coefficient was proposed. Predicted performance of thin cavity SJAs using the hybrid approach was shown to be in much better agreement with experiments than the prior models. This work provides a deeper understanding of modeling ferroelectric materials and SJAs, and the developed models can be used to help guide material and device design.

The dissertation of Michael Thomas Sheng is approved.

Robert N. Candler

Lihua Jin

Gregory P. Carman, Committee Co-Chair

Christopher S. Lynch, Committee Co-Chair

University of California, Los Angeles

2023

To my mother and father,

Li-Li and Chu-Chih Sheng,

who have given me so much

throughout my life.

Table of Contents

List of Figures

List of Tables

Acknowledgments

I would first like to thank my doctoral advisor, Professor Christopher Lynch, for his guidance and support throughout my studies. When I began my master's program in 2017, the thought of doing a PhD felt beyond my capabilities and I had given up my dreams for one long before. I am truly grateful for the opportunity Professor Lynch presented me to fulfil this dream by accepting me into his lab as his doctoral student. He gave me freedom to explore and was kind and patient throughout my successes and blunders. I would next like to thank Professor Gregory Carman who was like a second advisor. I especially appreciate the motivation and encouragement given this past year that helped me to keep on writing. I would also like to thank Professor Robert Candler and Professor Lihua Jin for agreeing to serve on my committee and spending their time to review my work.

Next, I would like to thank my collaborators David, Anthony, and Professor Miki of Actasys, Inc. for their help providing me with the experimental data used as the foundation of my synthetic jet actuator modeling work. The collaboration between Actasys, Inc. and UCLA was supported by the National Aeronautics and Space Administration under the Small Business Innovation Research (SBIR) program (Contract 80NSSC18C0028). I would like to thank the financial support of the National Science Foundation (NSF) Engineering Research Center (ERC) for Translational Applications of Nanoscale Multiferroic Systems (TANMS) under the Cooperative Agreement Award (No. EEC-1160504). TANMS was fundamental to my development as a researcher.

Next, I would like to thank all my lab mates who helped make my best of days better and worst of days more bearable. I thank Peng for bringing me up to speed on the phase field modeling work I inherited. Auni, for watching over and organizing activities for the lab group. This helped

give this group an identity. Yu-Ching, Michael, and Mahsa: I especially look back fondly on all the times we spent together. There were countless conversations, lunches, and activities through which we bonded. Scott, for all the discussions and help from working out theory to modeling in MATLAB and COMSOL to writing papers and reports. I would also like to thank Matthew, Emily, Jesse, Ruoda, and Victor of Professor Carman's group. I had spent the first two years of the pandemic working remotely, and I did not realize how refreshing the company of others during work could be. I am glad to have gotten the chance to get to know them more over the past year.

I would also like to thank my family and friends. They have been a huge support network for me throughout all these years. I thank my father Chu-Chih for his support, both financial and emotional, and for reminding me of all the Aunties and Uncles at my home church rooting and praying for me. I especially would like to acknowledge the late Uncle Harn who would frequently check up on my progress and give me advice for my studies. I thank my brother Jonathan for being a rock I can depend on during my time at UCLA. The fact that we were both in LA meant there was someone I could always reach out to if I ever needed help. I thank my beloved mother Li-Li for all the memories of love and joy she planted in my heart. These memories have been a constant source of strength for me to persevere to the end. I also would like to thank my grandmother A-ma and other relatives in Taiwan and over the world who believed in me and have been looking forward to my graduation. There have been so many others who helped me through my journey, there is no way I can name all the people here.

Above all, I would like to thank God who has always been watching over me. My faith has been tried and tested many times during these six years, but I have been loved and blessed through it all.

Preface

This dissertation contains my research on synthetic jet actuators and ferroelectric phase field modeling during my doctoral studies at UCLA. Looking back, I often worried whether my research would be good enough for a PhD. Now I realize I should have been more confident in the value of my contributions. Even if my final dissertation looks quite different from what I imagined early on in my degree, I learned that valuable research can still result from overcoming the obstacles encountered along the way.

My work on synthetic jet actuators started under the Center for Advanced Multifunctional Material Systems (CAMMS) at UCLA and was part of a collaboration led by Actasys, Inc. Aside from CAMMS-UCLA, this project included groups from Oak Ridge National Laboratory (ORNL) and Princeton University. Each group was tasked to develop a model focused on the physics pertaining to the group's expertise to reduce the complexity of the problem (Princeton: thermodynamics, ORNL: fluid dynamics, and CAMMS-UCLA: electromechanics). Instead of full multiphysics models that were computationally cost prohibitive, the idea was to split the physics into separate models except as inputs/outputs such as displacements and pressure between models that would then be used to iteratively to converge on the coupled solution. As the project reached completion, I realized that these models would be of limited use to companies like Actasys if they do not have access to the supercomputers ORNL used for the fluid dynamics simulations. This motivated me to develop an alternative modeling approach which is shared in this dissertation. Chapter 5 is a reworked version of my submitted manuscript to AIAA Journal with the permission of the American Institute of Aeronautics and Astronautics, Inc.:

Sheng, M. T., Keller, S. M., Mickalauskas, A., Menicovich, D., Amitay, M., & Lynch, C. S. (2023). Hybrid Lumped-element and Finite-element Model for Novel Synthetic Jet Actuator Shapes. *AIAA Journal.* In Press.

After CAMMS-UCLA's contract with Actasys was completed, I joined the Engineering Research Center for Translational Applications of Multiferroic Nanoscale Systems (TAMNS) and shifted focus from modeling ferroelectric devices at the macroscopic scale to modeling ferroelectric materials at the mescoscopic scale. This work builds on the ferroelectric phase field model for rhombohedral PIN-PMN-PT developed by Peng Lv. After testing the phase-field model's capabilities, we found two issues: 1) the model would unexpectedly crash due to singularity errors under the high loading conditions and 2), the model was unable to return to the original lowest energy phase after a load was applied and released to induce a forward and reverse phase transformation. These two issues eventually became another focus for my dissertation work. Chapters 3 and 4 form the basis of a manuscript currently in preparation:

Sheng, M. T., Keller, S. M., & Lynch, C. S. Improved Landau energy function for PIN-PMN-PT and the importance of fluctuations on modeling phase transitions. Manuscript In Preparation.

While my work on synthetic jet actuator and ferroelectric phase field models capture different physics (multiphysics coupled structural vibrations and mesoscale heterogeneous material behavior), both focused on identifying and addressing gaps where modeling predictions failed to reproduce experimental observations.

Vita

Education

2018 M.S., Mechanical Engineering

University of California, Los Angeles, USA

2016 B.S., Mechanical Engineering

University of California, Los Angeles, USA

Employment History

2017-2022 Graduate Student Researcher and Teaching Assistant

University of California, Los Angeles, USA

2020 Graduate Student Summer Intern

Sandia National Laboratories, USA

Publications

Sheng, M. T., Keller, S. M., Mickalauskas, A., Menicovich, D., Amitay, M., & Lynch, C. S. (2023). Hybrid Lumped-element and Finite-element Model for Novel Synthetic Jet Actuator Shapes. *AIAA Journal.* In Press.

Moreno, K.*, Murugesan, A.*, **Sheng, M*.**, Alqawasmi, L., Khraishi, T. A., & Hubbard, N. B. (2021, August). Correlation of Reduced-Order Models of a Threaded Fastener in Multi-Axial Loading. In *International Design Engineering Technical Conferences and Computers and Information in Engineering Conference* (Vol. 85468, p. V009T09A004). American Society of Mechanical Engineers. (*Co-first authors)

Xiang, Y., Liang, K., Keller, S., Guevara, M., **Sheng, M.**, Yan, Z., Zhou, P., Qi, Y., Ma, Z., Liu, Y., Srinivasan, G., Carman, G. P., & Lynch, C. S. (2020). Thickness-dependence of magnetic anisotropy and domain structure in Ni thin films grown on a PMN-PT substrate. *Smart Materials and Structures*, *29*(9), 095019.

Xu, R., Golinveaux, F. S., **Sheng, M.**, Xu, Z., Feng, Y., & Lynch, C. S. (2019). Effects of compressive stress on electric-field-induced phase transition of antiferroelectric ceramics. *Journal of Applied Physics*, *125*(20), 204104.

In preparation

Sheng, M. T., Keller, S. M., & Lynch, C. S. Improved Landau energy function for PIN-PMN-PT and the importance of fluctuations on modeling phase transitions. Manuscript In Preparation.

Presentations

Moreno, K., Murugesan, A., **Sheng, M.***, Alqawasmi, L., Khraishi, T. A., & Hubbard, N. B. (2021, August 17-19). *Correlation of Reduced-Order Models of a Threaded Fastener in Multi-Axial Loading* [Conference presentation]. ASME *2021 International Design Engineering Technical Conferences and Computers and Information in Engineering Conference,* online. (*Presenting Author)

Chapter 1: Introduction

Piezoelectric and ferroelectric materials have found use in a wide range of applications including sensors, transducers, and actuators. There has been a constant hunt over the past century for better properties to improve the performance of these devices. A better understanding of the underlying physics can help in the search for the next generation of ferroelectric materials. Phase-field models based on Landau theory are a powerful tool for investigating the effects of microstructural phenomena at the mesoscale. However, there have been various observations reported in literature that either are not able to be accurately modeled (e.g., phase transitions) or show unexpected behavior (e.g., nonuniform strain). This work seeks to answer the following research questions with regards to modeling ferroelectric material and piezoelectrically-driven synthetic jet actuators.

For ferroelectric material modeling, the main questions concern the:

- Discrepancy between predicted and measured coercive fields.
- Difficulty/inability of models of capturing certain phase transformation behavior.

For synthetic jet actuators devices, the main questions concern the:

- Discrepancy between modeled and measured device performance for thin SJAs.
- Predictive ability of the models (due to reliance on fitting parameters to experiments).

This chapter overview of the dissertation is provided to help guide readers. Chapter 2 provides a brief background and history of piezoelectric and ferroelectric materials. Chapters 3, 4 and 5 each include a brief and focused literature review. Chapters 3 and 4 cover developing a new energy function for PIN-PMN-PT with improved thermodynamic stability and using it to

investigate the effect of energy fluctuations and barriers on phase transformations. Chapter 4 specifically deals with the implementation of energy fluctuations in a phase field model. Chapter 5 moves away from material modeling on the mesoscale and into device modeling using bulk ferroelectric properties. This chapter covers developing a reduced-order synthetic jet actuators model for novel diaphragm and cavity designs. Chapter 6 concludes by summarizing the dissertation work and highlighting its key contributions.

Chapter 2: Background

I. History and Definitions

A brief overview of the history and terminology of piezoelectricity and ferroelectricity is provided in this chapter. For more information regarding the early history and development of ferroelectrics in the 20th century, readers are referred to Haertlings's article *Ferroelectric Ceramics: History and Technology* [1] or Lines and Glass' book *Principles and Applications of Ferroelectric and Related Materials* [2].

A. Early History

The direct piezoelectric effect (change in polarization in response to applied stress) was first discovered by Paul-Jacques and Pierre Curie in 1880 in various crystals—such as tourmaline, quartz, and Rochelle salt. The converse piezoelectric effect (mechanical deformation in response to an applied electric field) was theorized by Gabriel Lippman from fundamental thermodynamic principles and immediately confirmed by the Curies in 1881.

Piezoelectricity was mainly an academic curiosity until its first major application in sonar in 1917 during World War I. Its use and success in sonar generated new interest in piezoelectric based devices. In 1921, Valasek discovered what is now known as ferroelectricity in Rochelle salt. Rochelle salt, chemically sodium potassium tartate tetrahydrate, had a measurable remanent polarization which could be reversed with the application of an external field. This material had an extremely large dielectric and piezoelectric response in and near the ferroelectric region. (Lines and Glass). Various theories for the origin of ferroelectricity emerged based on water and hydrogen dipoles. Still, the physics behind ferroelectricity remained relatively obscured until the discovery of ferroelectricity in perovskite-structured barium titanate in 1944. The simplicity of barium

titanate's structure and stability of its ferroelectric phase relative to previously known ferroelectrics made it ideal for investigation. This led to rapid progress in understanding the physics behind ferroelectricity and the development of well-known perovskite type ferroelectrics including the solid solution lead zirconium titanate (PZT) system reported in 1952.

B. Piezoelectricity

The etymology for piezoelectricity comes from the combination from Ancient Greek *piezo* meaning "to press or squeeze" and electricity. Piezoelectricity specifically refers to the linear and reversible electromechanical coupling as an electrical or pressure load is applied. The electrical and mechanical coupling of the piezoelectric effect can be described in strain-charge form:

$$\boldsymbol{\varepsilon} = \boldsymbol{s^E \sigma} + \boldsymbol{d^T E} \tag{2-1}$$

$$\boldsymbol{D} = \boldsymbol{d\sigma} + \boldsymbol{kE} \tag{2-2}$$

where ε is the strain, s is the compliance, σ is the stress, d (and d^T) are the (transposed) piezoelectric coupling coefficients, E is electric field, D is the electric displacement, and k permittivity.

The stress-charge form rearranges the strain-charge form and uses:

$$\boldsymbol{\sigma} = \boldsymbol{c^E \varepsilon} - \boldsymbol{e^T E} \tag{2-3}$$

$$\boldsymbol{D} = \boldsymbol{e\varepsilon} + \boldsymbol{kE} \tag{2-4}$$

where c is the stiffness (inverse of compliance), and e is another form of the piezoelectric coupling coefficient.

Note that in some works and disciplines including the IEEE standard on piezoelectricity, an alternate notation is used. For example, the strain and stress are often respectively denoted by a capital S and capital T.

For dielectric materials, the electric displacement consists of two contributions:

$$\boldsymbol{D} \equiv k_0 \boldsymbol{E} + \boldsymbol{P} \tag{2-5}$$

where first term is the contribution due to an electric field and the second term is a contribution from the polarization. Polarization is a measure of the density of electric dipole moment p in a dielectric material. The polarization can be thought of as an average of the dipole moments in a given volume V.

$$\boldsymbol{P} = \frac{\Sigma \mathbf{p}}{\mathrm{V}} \tag{2-6}$$

The dipole moment between two point charges of opposite charge is

$$\mathbf{p} = \mathrm{q}\mathbf{d}_{\boldsymbol{q}} \tag{2-7}$$

where q is the charge and d_q is the displacement vector pointing from the negative to the positive charges.

C. Ferroelectricity

A subset of piezoelectric materials are also ferroelectric. Whereas piezoelectricity specifically refers to electromechanical behavior in the linear regime, ferroelectric materials also exhibits nonlinear behavior and has irreversible losses outside the linear regime. Even without an external field, ferroelectric materials have a spontaneous and reversible polarization. Ferroelectricity is not directly named after iron (ferro-), but rather parallels ferromagnetism which has similar behaviors. For example, both ferroelectrics and ferromagnets display hysteresis behavior. Figure 2-1 shows a simple schematic of a P-E hysteresis loop. There is a spontaneous or remanent polarization P_s even after the external field is removed. This polarization direction can be reversed if the external field reaches the coercive field E_c in the opposing direction.

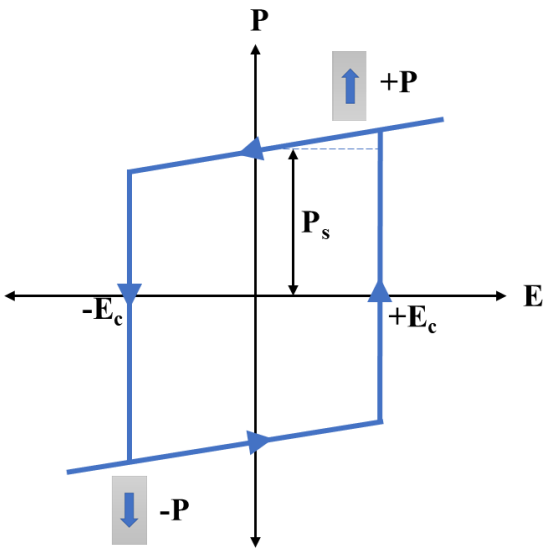

Figure 2-1: Example of P-E hysteresis plot showing spontaneous and reversible polarization.

II. Crystallography

A. Perovskite

Many well-known ferroelectrics like the oxide $BaTiO_3$ and solid solution PZT have a Perovskite crystal structure. Perovskite-type crystals have the form ABO_3 and are named after the mineral Perovskite. In the unit cell shown in Figure 2-2, the A lattice sites correspond to the unit cells' corners, the B lattice site corresponds to the body center, and the O sites correspond to the face centers. Solid solutions like PZT are mixtures of simpler oxides, so for PZT the B site is occupied by either a Zr^{4+} or Ti^{4+} cation.

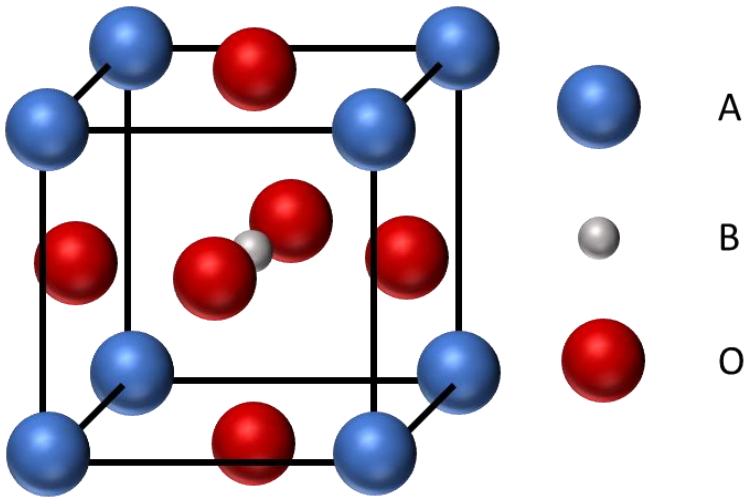

Figure 2-2: Schematic of ABO_3 Perovskite-type structure.

Figure 2-3 shows cases of how polarization arises through some offset of one or more ions from the center. If the crystal is centrosymmetric like in Figure 2-3a, there will be no polarization. However, if some of the ions are offset like in Figure 2-3b and Figure 2-3c, the offset charges will create local electric dipole moments and give the material an overall polarization. Often the more the ions are displaced from the center (or neutral) state, the stronger the overall polarization will be. This type of ferroelectric is considered displacive, meaning the polarization comes from ion displacements. Note that this involves shifts in the positions of all of the ions within each unit cell. Other types of ferroelectricity exist, such as order-disorder and electronic (spin-based or charge-based), but are not within the scope of this dissertation.

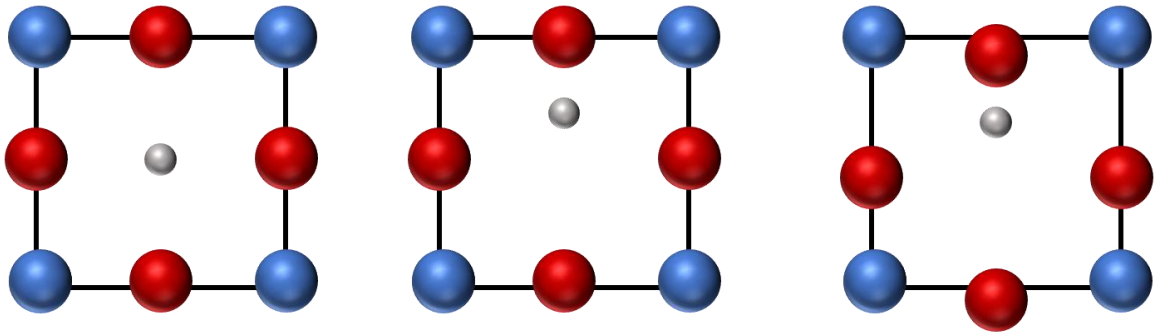

Figure 2-3: Polarization in the cases of a) no offset, b) offset of B site, and c) offset of both B and O sites.

B. Piezoelectricity, Pyroelectricity, and Ferroelectricity in Crystals

Crystals are classified into 32 symmetry point groups. Only a subset of these groups can display piezoelectric behavior, and a smaller subset of those groups is ferroelectric. For a material to exhibit piezoelectricity, the crystal must be non-centrosymmetric. There are 21 non-centrosymmetric and 11 centrosymmetric point groups. Of these 21 groups, 20 are piezoelectric (meaning it can be polarized through stress). Of these 20, 10 are pyroelectric (meaning it can be spontaneously polarized). A subgroup of these pyroelectric crystals is ferroelectric (meaning the polarization direction can be reversed). These relationships are summarized by the flow chart in Figure 2-4.

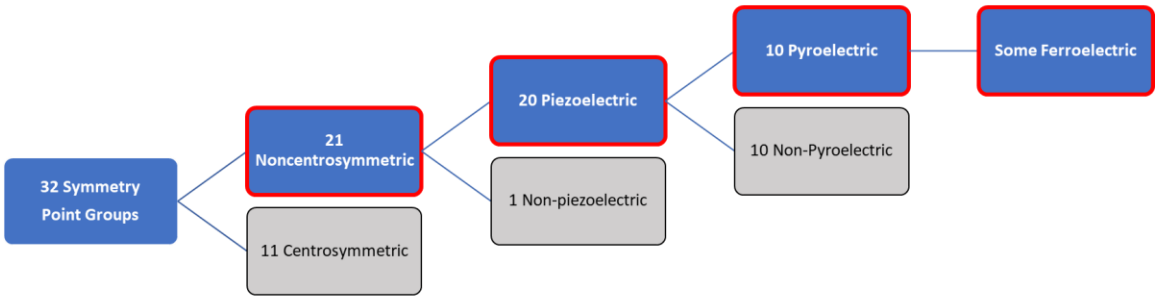

Figure 2-4: Piezoelectricity, pyroelectricity, and ferroelectricity flow chart relationship.

A single material may be able to express itself in different point groups depending on the environmental conditions. For example, single crystal $BaTiO_3$ is cubic and non-ferroelectric at high temperatures above its Curie temperature. As the material is cooled, the crystal transitions phases through ferroelectric tetragonal, ferroelectric orthorhombic, and ferroelectric rhombohedral.

III. Properties and Example Applications

Due to the strong electromechanical coupling of some piezoelectric and ferroelectric materials, they may be strong candidates as transducers, actuators, or sensors needed in many applications. There are many parameters to consider for deciding which ferroelectric materials are appropriate for a given application. In addition to logistical considerations such as cost, material properties such as the permittivity, stiffness, piezoelectric coupling, coercive field, loss tangent, and phase transition temperatures will determine which materials can satisfy the desired design goals.

The coercive field is one important factor. Ferroelectrics like PZT can be broadly classified as hard or soft depending on the coercive field. Hard piezoelectrics have higher coercivity, whereas soft piezoelectrics have lower coercivity. Hard piezoelectrics tend to be more stable under high

mechanical and electrical loads with lower losses, whereas soft piezoelectrics tend to have higher piezoelectric coefficients.

A. Example Applications

Two example applications are described below:

1. Piezoelectric Unimorph

The piezoelectric coefficient d_{ij} is a measure of how much the material will strain (j=1-6, using Voigt notation) due to an electric field along i (i=1,2, or 3). For example, a 3-3 mode means that strain component being used is parallel to the electric field, and a 3-1 mode means that the strain component being used is perpendicular to the electric field.

Other forms of deformation can be achieved depending on boundary conditions. For example, Figure 2-5 shows a schematic of a piezoelectric unimorph. If an electric field is applied across the piezoelectric layer, there will be an elastic mismatch between the substrate and piezoelectric layers causing the beam to bend.

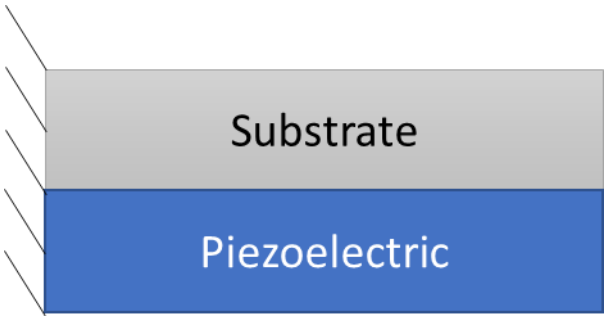

Figure 2-5: Schematic of bound piezoelectric and substrate layers forming a piezoelectric unimorph.

2. Multiferroic Composite

Another application is to form a multiferroic composite. Most materials have low magnetoelectric coupling, however, it was demonstrated that strong magnetoelectric coupling can be achieved with multiferroic composites [3]. Figure 2-6 shows an example schematic of a multiferroic magnetostrictive-ferroelectric composite. The ferroelectric layer provides electrical and mechanical coupling, and the magnetostrictive layer provides mechanical and magnetic coupling. When the two layers are combined, the composite material can result in high magnetoelectric coupling.

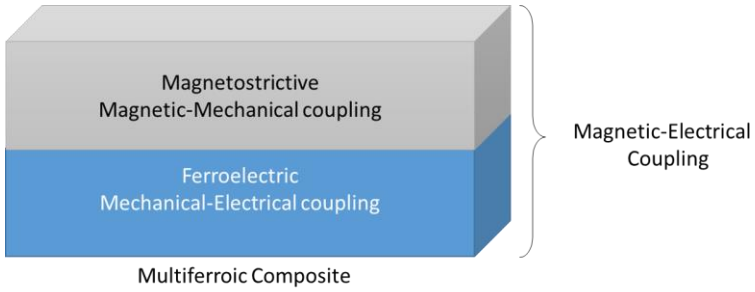

Figure 2-6: Schematic of multiferroic composite coupling magnetostrictive and ferroelectric material.

B. Developments

There has been an ongoing search for better-performing materials. Single crystal relaxor ferroelectrics like PMN-PT and PIN-PMN-PT have garnered attention for their large electromechanical properties relative to polycrystalline ferroelectrics like PZT. There has also been renewed interest in finding high performing Pb-free alternatives due to concerns of lead toxicity to the environment [4–6]. In either case, a better understanding of the underlying mechanisms can help guide material development.

Models have been developed to describe piezoelectricity and ferroelectricity at multiple length scales, from using bulk properties all the way down to atoms of a crystal lattice. Polycrystalline ceramics contain numerous grains separated by grain boundaries. Within each grain the crystal lattice is continuous. A crystal consists of atoms forming a repeating structure and can either be single domain or multidomain.

Bulk property models are used for the macroscale, while microscale models can incorporate grain, defects, and grain boundary effects. At the atomic scale models include density functional theory (DFT) and molecular dynamics (MD). For the mesoscale (between atomic and microscopic scales), phase field models based on Landau theory are used to model domains and domain walls. This dissertation work used models at the mesoscale (to investigate phase transformations) and the macroscale (using bulk properties for SJA devices).

IV. References

[1] Haertling, G. H. “Ferroelectric Ceramics: History and Technology.” *Ferroelectricity: The Fundamentals Collection*, Vol. 818, 1994, pp. 157–178. https://doi.org/10.1002/9783527618002.ch6.

[2] Lines, M. E., and Glass, A. M. Basic Concepts. In *Principles and Applications of Ferroelectrics and Related Materials*, Oxford University Press, 2001, pp. 1–23.

[3] Ryu, J., Priya, S., Uchino, K., and Kim, H.-E. “Magnetoelectric Effect in Composites of Magnetostrictive and Piezoelectric Materials.” *Journal of Electroceramics*, Vol. 8, 2002, pp. 107–119. https://doi.org/10.1023/A.

[4] Beveren, W. Van. “Lead-Free Piezoceramics.” Vol. 432, No. November, 2004, pp. 2–5. https://doi.org/10.1038/nature03008.1.

[5] Shvartsman, V. V., and Lupascu, D. C. “Lead-Free Relaxor Ferroelectrics.” *Journal of the American Ceramic Society*, Vol. 95, No. 1, 2012, pp. 1–26. https://doi.org/10.1111/j.1551-2916.2011.04952.x.

[6] Zhang, S., Malič, B., Li, J. F., and Rödel, J. “Lead-Free Ferroelectric Materials: Prospective Applications.” *Journal of Materials Research*, Vol. 36, No. 5, 2021, pp. 985–995. https://doi.org/10.1557/s43578-021-00180-y.

Chapter 3: Improved energy function for PIN-PMN-PT and the effect of fluctuations on phase transformations

I. Introduction

Ferroelectrics are widely used as transducers, sensors, and actuators due to their strong electromechanical coupling. In recent decades, $PbTiO_3$-based relaxor ferroelectric crystals, such as PMN-PT and PIN-PMN-PT, have garnered great interest due to their ultrahigh electromechanical properties, particularly those located near a morphotropic phase boundary. Relaxor ferroelectrics are typically characterized by a broad dielectric permittivity peak that is both temperature- and frequency-dependent. Furthermore, while the susceptibility follows the Curie-Weiss law at high temperatures, the deviation increases at lower temperatures [1]. However, the low coercive field E_c, low Curie point, and/or low rhombohedral-tetragonal phase transition temperature of PZN-PT and PMN-PT limit their operating temperature and electric fields. To overcome these limitations, the ternary $x\ PbIn_{1/2}Nb_{1/2}O - (1-x-y)\ PbMg_{1/3}Nb_{2/3}O_3 - y\ PbTiO_3$ has been developed, which exhibits increased phase transition temperatures and coercive fields while retaining excellent piezoelectric properties. These advancements have positioned the ternary material at the forefront of electroacoustic technologies [2,3].

Landau-Devonshire energy functions have been successfully developed to describe various ferroelectric materials and their properties. These energy functions have been used in phase field models to investigate the microstructure behavior of perovskite-based ferroelectrics as well as for domain engineering [3]. Domain engineering involves cutting and poling the crystal into domain structures such that the performance is optimized for a particular mode. This has been applied to various ferroelectric materials including $BaTiO_3$, PZN-PT, and PMN-PT [4–6]. Devonshire was

the first to apply Landau's theory on phase transformations to ferroelectric $BaTiO_3$ crystals and developed a 6^{th}-order polynomial energy function to describe the structural free energy of the crystal as a function of polarization. Bell and Cross [7] modified this energy function to model field-driven phase changes. Later, Amin et al. [8] developed a 6th-order energy function capable of modeling various compositions of PZT, while Haun et al. [9] developed a 6^{th}-order energy function for single-domain $PbTiO_3$.

After the discovery of the monoclinic ferroelectric phase in PZT by Noheda [10], Vanderbilt and Cohen [11] showed that higher-ordered energy functions were necessary to account for additional phases. An 8^{th}-order energy function is the minimum to describe three phases, while the triclinic phase required going up to the 12^{th} order. Li et al. [12] developed an 8th-order energy function for $BaTiO_3$ that reproduced the R-O-T-C transition temperatures and was also applicable for a thin film under compressive biaxial strains. Wang et al. [13] added additional temperature-dependent terms to provide a better description of dielectric properties at temperatures around the Curie temperature. Heitman and Rosetti [14] developed methods to reproduce morphotropic phase boundary effects for PZT.

Zhang [15] developed a 6^{th} order energy function based on PMN-PT to investigate the coexistence of tetragonal and rhombohedral phases. As a 6^{th} order polynomial, this energy function cannot simultaneously describe the tetragonal, orthorhombic, and rhombohedral phases. Lv et al. [16] developed a 10^{th} order energy function for a relaxor ferroelectric that describes the dielectric, piezoelectric, and ferroelectric properties of a PIN-PMN-PT composition near the morphotropic phase boundary that undergoes cubic to tetragonal to orthorhombic to rhombohedral phase transformations while cooling. However, this energy function is thermodynamically unstable at high polarization values. While the instability did not present an issue for Lv's investigation of

domain formation and domain wall evolution [17,18], it results in unrealistic behavior under certain electric and/or mechanical loads.

The development of higher order energy functions has enabled phase field modeling of many microstructural interactions, but there are still challenges in accurately modeling phase transitions and switching. Phase-field models have been implemented using various computational methods including the semi-implicit Fourier spectral method [19], finite difference method, and finite element method (FEM) [20,21]. Phenomena such as domain formation [22,23] and switching [24,25] have been simulated and also used to study the effects such as mechanical strain, defects, grains, and domain walls [21,26–28].

There are discrepancies between the measured and predicted coercive fields from the energy functions. Discrepancies between modeled and observed coercive fields exist and are attributed to metastable wells in the energy function and thermal fluctuations in real materials. While this is commonly assumed, the effects of energy fluctuations and metastable states are often neglected in phase-field modeling [29]. Kingsland et al. [30] used atomistic first principle simulations and found that the nearly an order magnitude difference between theoretical predictions and observed measurements may be due to strong residual depolarizing fields based on defects in the crystal lattice. Indergand et al. [28] found the addition of stochastic noise to the phase field model provided a more accurate prediction of the coercive field for bulk polycrystalline PZT promoted the formation of needle-like domains in regions of high heterogeneity or stress concentration.

This chapter presents an improved 10^{th} order energy function for a composition of PIN-PMN-PT near the MPB by following Lv's method of coefficient determination. Instead of using a single fitting parameter to adjust for changes in the dielectric permittivities for a composition

closer to the MPB, each permittivity had its own fitting parameter. The energy function using this proposed set of coefficients is more thermodynamically stable than that of Lv. Analysis and discussion follow on the effect metastability and energy fluctuations have on phase transformations.

II. Energy Function

A. Landau-Devonshire Energy

Landau theory assumes that the free energy $F - F_0$ of a system can be described analytically. For example, if a system's symmetry is broken at some critical temperature, then the Landau free energy can be described by a series expansion about some order parameter η, which characterizes the asymmetry. A plot of the free energy above and below the critical point is shown in Figure 3-1. Above T_c, the energy is minimized when the order parameter is zero. Below T_c, new energy minima appear giving a spontaneous and non-zero η_s.

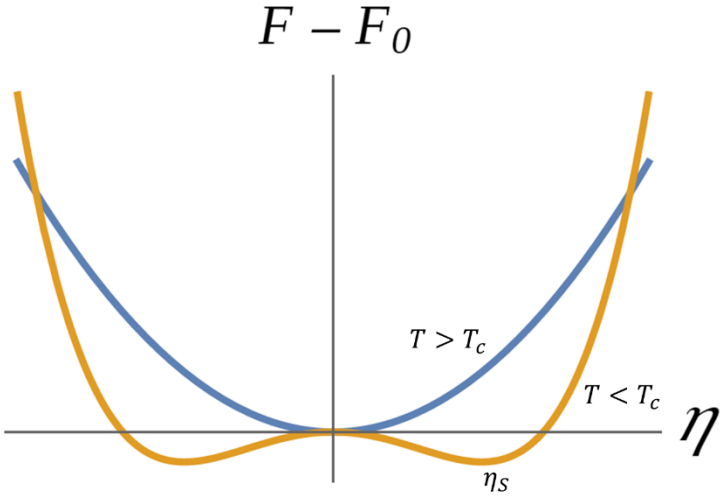

Figure 3-1: Example of the free energy $F - F_0$ as a function of the order parameter η described by Landau theory at temperatures above and below some critical temperature T_c.

For ferroelectrics, the order parameter is polarization, and the critical temperature is also known as the Curie temperature. The crystal is cubic above the Curie temperature and there is no spontaneous polarization. The free energy, the Landau-Devonshire energy, has the following form in index notation:

$$f_{LD} = \alpha_{ij} P_i P_j + \alpha_{ijkl} P_i P_j P_k P_l + \cdots + \alpha_{i\ldots r} P_i \ldots P_r \tag{3-1}$$

where α_{ij} are the Landau coefficients and P_i is the polarization.

For thermodynamic stability, the highest order coefficients should all be:

$$\alpha_{i\ldots r} > 0 \tag{3-2}$$

Using material symmetries, the indices of the coefficients are often rewritten with reduced indices:

$$f_{LD} = \alpha_i P_i^2 + \alpha_{ij} P_i^2 P_j^2 + \cdots \tag{3-3}$$

This energy describes the structural free energy of the crystal lattice as a function of the polarization, with the unpolarized cubic phase under zero stress as the reference energy state. Typically, higher order coefficients can allow for more material characteristics to be modeled or expand its applicability. Higher order terms are necessary to accommodate additional phases within a single energy function.

The following 10th order energy function was fitted to experimental data from literature and used to model the spontaneous tetragonal, orthorhombic, and rhombohedral phases with a single function [16]:

$$
\begin{aligned}
f_{LD}(P_1, P_2, P_3) = {} & \alpha_1(P_1^2 + P_2^2 + P_3^2) + \alpha_{11}(P_1^4 + P_2^4 + P_3^4) + \alpha_{12}(P_1^2P_2^2 + P_1^2P_3^2 + P_2^2P_3^2) \\
& + a_{111}(P_{1^6} + P_{2^6} + P_{3^6}) + \alpha_{112}\left(P_1^2(P_2^4 + P_3^4) + P_2^2(P_1^4 + P_3^4) + P_3^2(P_1^4 + P_2^4)\right) \\
& + \alpha_{123}(P_1^2P_2^2P_3^2) + \alpha_{1111}(P_1^8 + P_2^8 + P_3^8) \\
& + \alpha_{1112}\left(P_1^6(P_2^2 + P_3^2) + P_2^6(P_1^2 + P_3^2) + P_3^6(P_1^2 + P_2^2)\right) \\
& + \alpha_{1122}(P_1^4P_2^4 + P_1^4P_3^4 + P_2^4P_3^4) + \alpha_{1123}(P_1^2P_2^2P_3^4 + P_1^2P_2^4P_3^2 + P_1^4P_2^2P_3^2) \\
& + \alpha_{11111}(P_1^{10} + P_2^{10} + P_3^{10}) \\
& + \alpha_{11112}\left(P_1^8(P_2^2 + P_3^2) + P_2^8(P_1^2 + P_3^2) + P_3^8(P_1^2 + P_2^2)\right) \\
& + \alpha_{11122}\left(P_1^6(P_2^4 + P_3^4) + P_2^6(P_1^4 + P_3^4) + P_3^6(P_1^4 + P_2^4)\right) \\
& + \alpha_{11223}(P_1^4P_2^4P_3^2 + P_1^4P_2^2P_3^4 + P_1^2P_2^4P_3^4) \\
& + \alpha_{11123}(P_1^2P_2^2P_3^6 + P_1^2P_2^6P_3^2 + P_1^6P_2^2P_3^2)
\end{aligned}
\tag{3-4}
$$

where α_i through α_{ijklm} are the fifteen Landau coefficients and P_i are the orthogonal components of polarization using the pseudo-cubic unit cell as the reference coordinate system. The energy of the unpolarized and unstrained crystal is used as the reference energy, so the elastic energy is not included in the function above.

Figure 3-2 is a plot of the energy density of polarizations in the $(1\bar{1}0)$ diagonal plane using Lv's set of coefficients. This plane was chosen since it can describe the tetragonal, orthorhombic and rhombohedral phases. The plot uses polarizations $P_{12} = (P_1 + P_2)/\sqrt{2}$ and P_3 as the axes. The energy function is thermodynamically unstable at higher polarizations as shown in Figure 3-2. When the examining energy landscape for values of P_{12} and P_3 between -0.5 and +0.5 C/m^2, there are no instabilities. However, when the bounds are extended to -1.0 and +1.0 C/m^2, the plot

becomes unstable after 0.6-0.7 C/m^2 and goes to negative infinity due to the negative higher order terms.

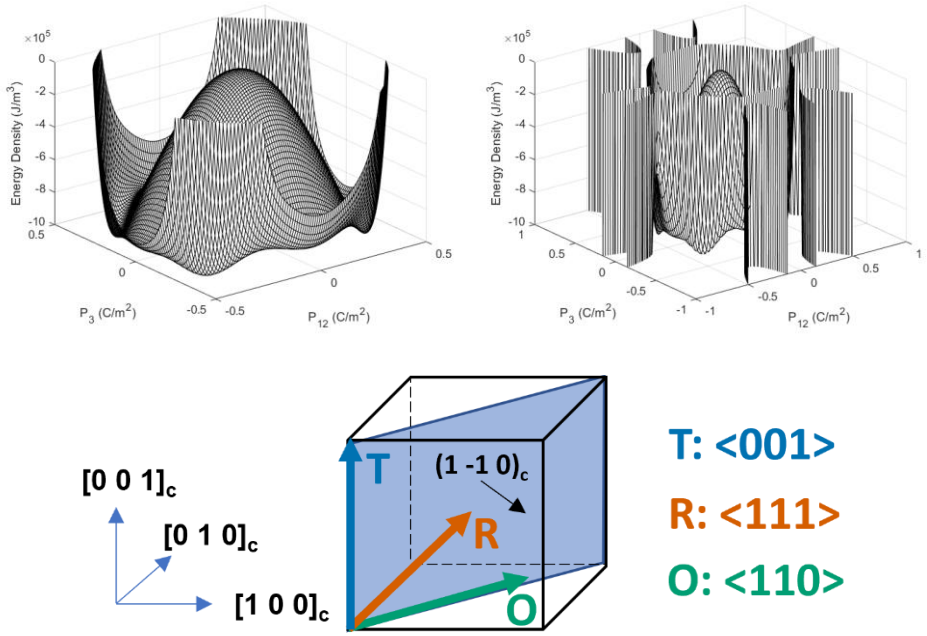

Figure 3-2: Lv's Energy function landscape at room temperature with polarizations P_{12} and P_3 bounded between top left: [-0.5,0.5] and top right: [-1,1]. Top right image shows that the energy function is unstable at higher polarizations. The polarizations that describe this energy landscape is contained in the plane shown in the bottom image.

The energy function can be rewritten in a phase structures' local coordinate system as defined by Table 3-1. The local coordinate system is defined such that the x_3 and poling direction are the same. For the single domain phases (labeled 1T, 1O and 1R), this would also be the spontaneous direction of the polarization.

Table 3-1: Phase structure, variants, and their corresponding poling direction and local coordinate system.

Structure	Poling Direction	Local Coordinate System x_1 - x_2 - x_3	Variants
1T	[001]	[100] - [010] - [001]	[001]
1O	[110]	$[\bar{1}10]$ - [001] - [110]	[110]
1R	[111]	$[1\bar{1}0]$ - $[11\bar{2}]$ - [111]	[111]
2R	[110]	$[\bar{1}10]$ - [001] - [110]	[111], $[11\bar{1}]$
4R	[001]	[100] - [010] - [001]	[111], $[1\bar{1}1]$, $[\bar{1}11]$, $[\bar{1}\bar{1}1]$

The transformed polarization vector $\boldsymbol{P}^A$ written for a local coordinate system that corresponds to a phase (A: T, O, or R) can be found by applying a rotation to the polarization in the $\boldsymbol{P}$ vector:

$$\boldsymbol{P}^A = \begin{bmatrix} P_1^A \\ P_2^A \\ P_3^A \end{bmatrix} = R_A \begin{bmatrix} P_1 \\ P_2 \\ P_3 \end{bmatrix} = R_A \boldsymbol{P} \tag{3-5}$$

where R_A is the rotation matrix between the global pseudo-cubic coordinate system and the corresponding local coordinate system where x_3 aligns with the poling direction of each phase.

The rotation matrices for the tetragonal, orthorhombic, and rhombohedral phases are:

$$R_T = \begin{bmatrix} 1 & 0 & 0 \\ 0 & 1 & 0 \\ 0 & 0 & 1 \end{bmatrix} \tag{3-6}$$

$$R_O = \begin{bmatrix} -\frac{\sqrt{2}}{2} & \frac{\sqrt{2}}{2} & 0 \\ 0 & 0 & 1 \\ \frac{\sqrt{2}}{2} & \frac{\sqrt{2}}{2} & 0 \end{bmatrix} \tag{3-7}$$

$$R_R = \begin{bmatrix} \frac{\sqrt{2}}{2} & -\frac{\sqrt{2}}{2} & 0 \\ \frac{\sqrt{6}}{6} & \frac{\sqrt{6}}{6} & \frac{\sqrt{6}}{3} \\ \frac{\sqrt{3}}{3} & \frac{\sqrt{3}}{3} & \frac{\sqrt{3}}{3} \end{bmatrix} \tag{3-8}$$

In the corresponding local coordinate system, the energy function for the spontaneous tetragonal, orthorhombic, and rhombohedral phases are:

$$f_{LD}^{T}\left(P_S^T(T)\right) = \alpha_1 {P_S^T}^2 + \alpha_{11} {P_S^T}^4 + \alpha_{111} {P_S^T}^6 + \alpha_{1111} {P_S^T}^8 + \alpha_{11111} {P_S^T}^{10} \tag{3-9}$$

$$\begin{aligned} f_{LD}^{O}\left(P_S^O(T)\right) = {P_S^O}^2\alpha_1 + \frac{1}{2}\alpha_{11}{P_S^O}^4 + \frac{1}{4}\alpha_{12}{P_S^O}^4 + \frac{1}{4}\alpha_{111}{P_S^O}^6 + \frac{1}{4}\alpha_{112}{P_S^O}^6 + \frac{1}{8}\alpha_{1111}{P_S^O}^8 \\ + \frac{1}{8}\alpha_{1112}{P_S^O}^8 + \frac{1}{16}\alpha_{1122}{P_S^O}^8 + \frac{1}{16}\alpha_{11111}{P_S^O}^{10} + \frac{1}{16}\alpha_{11112}{P_S^O}^{10} \\ + \frac{1}{16}\alpha_{11122}{P_S^O}^{10} \end{aligned} \tag{3-10}$$

$$\begin{aligned} f_{LD}^{R}\left(P_S^R(T)\right) = {P_S^R}^2\alpha_1 + \frac{1}{3}\alpha_{11}{P_S^R}^4 + \frac{1}{3}\alpha_{12}{P_S^R}^4 + \frac{1}{9}\alpha_{111}{P_S^R}^6 + \frac{2}{9}\alpha_{112}{P_S^R}^6 + \frac{1}{27}\alpha_{123}{P_S^R}^6 \\ + \frac{1}{27}\alpha_{1111}{P_S^R}^8 + \frac{2}{27}\alpha_{1112}{P_S^R}^8 + \frac{1}{27}\alpha_{1122}{P_S^R}^8 + \frac{1}{27}\alpha_{1123}{P_S^R}^8 + \frac{1}{81}\alpha_{11111}{P_S^R}^{10} \\ + \frac{2}{81}\alpha_{11112}{P_S^R}^{10} + \frac{2}{81}\alpha_{11122}{P_S^R}^{10} + \frac{1}{81}\alpha_{11123}{P_S^R}^{10} + \frac{1}{81}\alpha_{11223}{P_S^R}^{10} \end{aligned} \tag{3-11}$$

B. Material Properties

This work uses the same base data used in [16] to determine coefficients of the energy function for a composition of PIN-PMN-PT near the MPB that is rhombohedral at room temperature (typically 32%-33% PT content). This data is listed in Table 3-2. Several assumptions

were made to obtain the data used to characterize a composition near the MPB that is rhombohedral at room temperature. As the temperature is increased, the composition near the MPB transitions from the rhombohedral phase to orthorhombic phase to tetragonal phase to cubic phase. Data for a single composition is needed but not available, so a qualitative composition and temperature equivalence was used fill in gaps in the available data in literature. As the PT% content is increased, the spontaneous phase at room temperature will change from rhombohedral to orthorhombic or tetragonal. Approximations of unavailable properties were based on single domain data from other PIN-PMN-PT compositions at room temperature. For example, while the composition of interest is rhombohedral at room temperature, the "spontaneous" tetragonal and orthorhombic phases' properties are assumed to be similar to compositions with higher or lower PT content that naturally occur as tetragonal or orthorhombic at room temperature. Similarly, the tetragonal and orthorhombic properties at elevated temperatures are also assumed to be on a similar order of magnitude.

The transition temperatures $T_{RO} = 93°C$ and $T_{OT} = 118°C$ were based on PIN-PMN-0.32PT with PIN content between 0.25 and 0.35 [2]. The tetragonal phase's spontaneous polarization P_S^T and dielectric permittivities e_{33}^T and e_{11}^T were based on PIN-PMN-PT with PT% content on the order of 38-42% [31]. The (psuedo)-orthorhombic phase's dielectric permittivities e_{33}^O, e_{11}^O, and e_{22}^O were based on composition around 0.27PIN-0.40PMN-0.33PT [32]. The rhombohedral dielectric permittivities were based on 0.24PIN-0.49PMN-0.27PT [33]. Other parameters such as the Curie constant C, Curie-Weiss temperature T_0, orthorhombic phase's spontaneous polarization P_S^O, and rhombohedral phase's spontaneous polarization P_S^O were estimated according to [16].

Instead of using a single fitting parameter to account for the change in the dielectric permittivity of a different composition and temperature. Separate fitting parameters for each permittivity were needed to obtain an energy function that was thermodynamically stable with the additional constraints.

Table 3-2: Material Properties for Coefficient Determination

Quantities	-	-	Quantities	-	-
C	1.48×10^6	$°C$	T_2^*	25	$°C$
T_0	182	$°C$	$P_s^O(T_2^*)$	0.455	C/m^2
T_C	192	$°C$	$e_{33}^O(T_2^*)$	$1500 \times K_3^O$	-
T_1^*	25	$°C$	$e_{11}^O(T_2^*)$	$8070 \times K_1^O$	-
$P_s^T(T_1^*)$	0.43	C/m^2	$e_{22}^O(T_2^*)$	$30000 \times K_2^O$	-
$e_{33}^T(T_1^*)$	$1090 \times K_3^T$	-	T_3^*	25	$°C$
$e_{11}^T(T_1^*)$	$15000 \times K_1^T$	-	$P_S^R(T_3)$	0.47	C/m^2
T_{OT}	118	$°C$	$e_{33}^R(T_3^*)$	$650 \times K_3^R$	-
T_{RO}	93	$°C$	$e_{11}^R(T_3^*)$	$5800 \times K_1^R$	-

C. Coefficient Determination

There are 15 coefficients for a 10th order Landau-Devonshire energy function. Coefficients are assumed to be temperature independent except for α_1. Though relaxor behavior deviates from the Curie-Weiss Law, the first coefficient is still approximated by:

$$\alpha_1 = \frac{T - T_0}{2e_0 C} \tag{3-12}$$

where T is the temperature, T_0 is the Curie-Weiss temperature, $e_0$is the permittivity of free space, and C is the Curie constant. T_0 is typically slightly lower than T_C.

Coefficients were determined numerically by solving three systems of equations sequentially. Determined coefficients were used in subsequent sets to reduce the number of unknowns solved for at one time. Two coefficients, α_{11111} and α_{11122}, were not necessary to fit

the energy function to the properties listed in Table 3-2 and were set to zero for convenience. Additionally, all the other highest-order coefficients followed an additional constraint:

$$\alpha_{ijklm} > 0 \tag{3-13}$$

to ensure the energy function is thermodynamically stable. Since α_{11111} was set to zero, α_{1111} must also be positive for stability.

The systems of equations were constructed using three types of relationships:

1. Energy Equivalence

The spontaneous energies of two phases A and B are assumed to be equivalent during their phase transition at temperature T_{AB}:

$$f_{LD}^{A}\left(0,0,P_S^A(T_{AB})\right) = f_{LD}^{B}\left(0,0,P_S^B(T_{AB})\right) \tag{3-14}$$

For example, $f_{LD}^{R}\left(0,0,P_S^R(T_{RO})\right) = f_{LD}^{O}\left(0,0,P_S^O(T_{RO})\right)$ at the rhombohedral-orthorhombic transition temperature T_{RO}.

2. Local Minima

A spontaneous phase occurs at a local energy minimum. As a local minimum, the first derivative satisfies:

$$\frac{\partial f_{LD}^{A}}{\partial P_3^A}(0,0,P_S^A) = 0 \tag{3-15}$$

3. Dielectric Coefficient

The dielectric coefficient e_{ij}^{A} is related to the second derivative of the energy function by:

$$\frac{1}{e_{ij}^{A} e_0} = \frac{\partial^2 f_{LD}^{A}(0,0,P_S^A)}{\partial P_i^A \partial P_j^A} \tag{3-16}$$

The coefficients α_{11}, α_{111}, and α_{1111}were determined by a set of equations based on the tetragonal phase. Coefficients α_{12}, α_{112}, α_{1112}, α_{1122}, and α_{11112} were determined by a set of equations based on the tetragonal and orthorhombic phases. The remaining coefficients α_{123}, α_{1123}, α_{11223}, and α_{11123} were determined by a set of equations based on the orthorhombic and rhombohedral phases. See the Appendix of this chapter for more information.

III. Proposed Energy Function

A. Fitting Parameters and Resulting Landau Coefficients

Table 3-3 lists the values of the fitting parameters K_i^A, corresponding the dielectric permittivity ε_{ii}^A, that result in a stable energy function with two specified phase transitions between room temperature and the Curie point. Since the value of dielectric permittivity used is based on a different PIN-PMN-PT composition, the fitting parameter accounts for the variation due to compositional differences. Most multipliers indicate an increase in the permittivity closer to the MPB aside for ε_{22}^O. The resulting Landau coefficients are listed in Table 3-4

Table 3-3: Dielectric permittivity adjustments for composition closer to MPB.

Parameter	Value
K_3^T	1.5
K_1^T	1.5
K_3^O	1.4
K_1^O	1.6
K_2^O	0.7
K_3^R	2.15
K_1^R	1.5

Table 3-4: Landau Coefficients of 10th order energy function. T is temperature in $°C$.

	Coefficient	Units		Coefficient	Units
α_1	$3.816 \times 10^4\ (T - 182)$	$C^{-2}\ m^2\ N$	α_{1122}	-1.534×10^9	$C^{-8}\ m^{14}\ N$
α_{11}	-1.212×10^7	$C^{-4}\ m^6\ N$	α_{1123}	-2.234×10^{10}	$C^{-8}\ m^{14}\ N$
α_{12}	-2.641×10^7	$C^{-4}\ m^6\ N$	α_{11112}	8.571×10^8	$C^{-10}\ m^{18}\ N$
α_{111}	9.428×10^7	$C^{-6}\ m^{10}\ N$	α_{11223}	6.518×10^{10}	$C^{-10}\ m^{18}\ N$
α_{112}	3.881×10^8	$C^{-6}\ m^{10}\ N$	α_{11123}	7.496×10^{10}	$C^{-10}\ m^{18}\ N$
α_{123}	2.916×10^9	$C^{-6}\ m^{10}\ N$	α_{11111}	0	$C^{-10}\ m^{18}\ N$
α_{1111}	3.180×10^7	$C^{-8}\ m^{14}\ N$	α_{11112}	0	$C^{-10}\ m^{18}\ N$
α_{1112}	-3.388×10^8	$C^{-8}\ m^{14}\ N$			

Nine of the thirteen non-zero Landau coefficients are different from Lv's coefficients. More importantly, the highest order coefficients α_{ijklm} (as well as α_{1111} since $\alpha_{11111} = 0$) are all non-negative. This results in a thermodynamically stable energy function. In this case, the energy goes to positive infinity for large polarization values.

B. Simulated Properties

Figure 3-3 shows the energy density for polarizations in the $(1\bar{1}0)$ diagonal plane plotted as a function of $P_{12} = (P_1 + P_2)/\sqrt{2}$ and P_3 at room temperature using the set of coefficients listed in

Table 3-4. In contrast to figure 2, the energy landscape does not result in singularities at higher polarizations. There are 8 local minima depicted, corresponding to the variants of the tetragonal, orthorhombic, and rhombohedral phases contained in the $(1\bar{1}0)$ diagonal plane. At room temperature, the rhombohedral phase is the most energy favorable, while the tetragonal and orthorhombic phases are considered metastable states. Phases are separated by some energy barrier, typically determined by the closest saddle point.

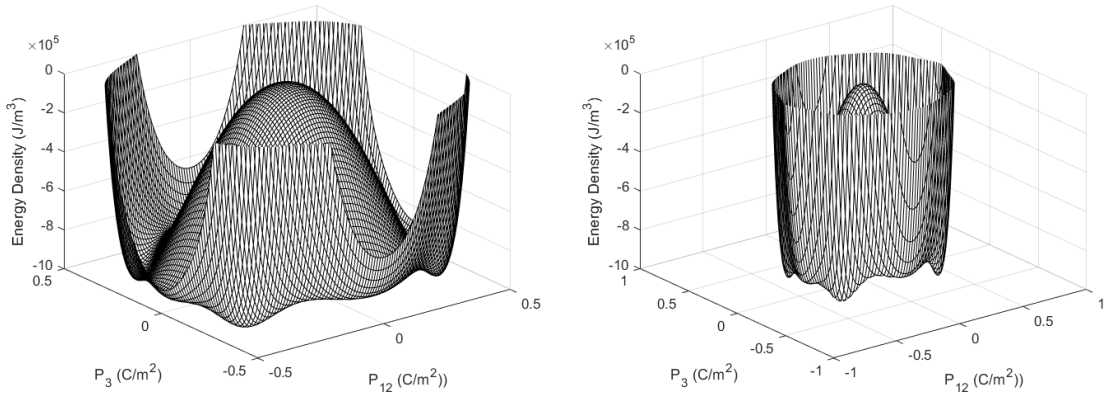

Figure 3-3: Energy landscape of the proposed energy function from this work at room temperature. Energy density is plotted against polarizations P_{12} and P_3 bounded between left: [-0.5,0.5] and right: [-1,1].

Figure 3-4 shows the energy density of the three ferroelectric phases plotted as a function of temperature. The rhombohedral phase depicted by the solid red line is the lowest energy state until transition temperature $T_{RO} = 93°$, after which it becomes the orthorhombic phase depicted by the dashed green line. The tetragonal phase depicted by the dotted blue line becomes the most energy favorable after $T_{OT} = 118°$ until it becomes the (paraelectric) cubic phase at Curie temperature $T_C = 192°$.

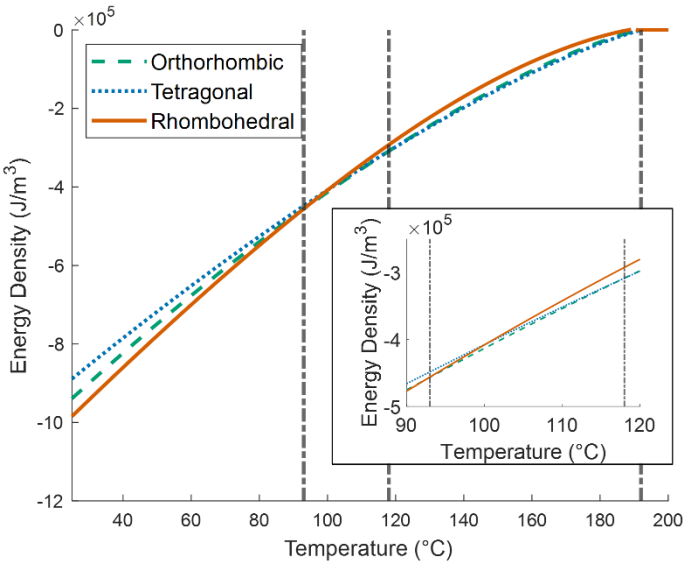

Figure 3-4: Energy density of the orthorhombic, tetragonal, and rhombohedral phases as a function of temperature. The R-O and O-T phase transitions are designated by the black dash-dotted line. (O: dashed green, T: dotted blue, and R: solid red.)

Figure 3-5 shows the polarizations corresponding to the three phases as a function of temperature from room temperature to 200°C. Vertical lines correspond to temperatures T_{RO}, T_{OT}, and T_C. The sharp drop to zero polarization corresponds to the complete disappearance of a particular phase's well from the energy landscape. For this energy function, the rhombohedral well disappears at 191° C, the orthorhombic well disappears at 195° C, and the tetragonal well disappears at 196°C.

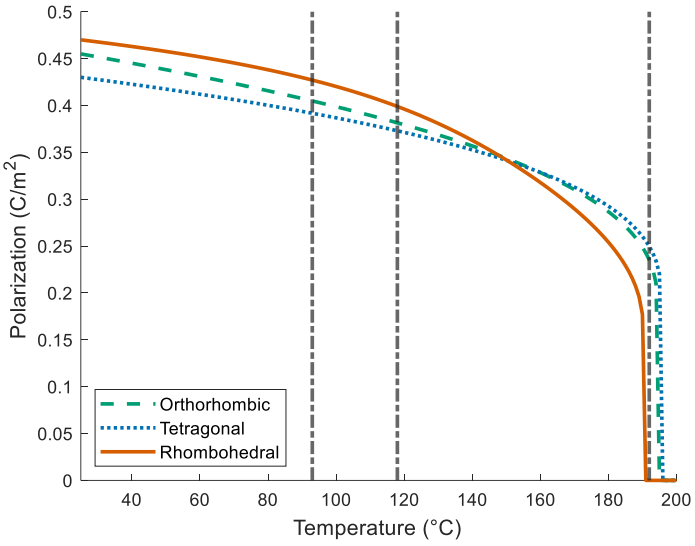

Figure 3-5: Polarizations corresponding to the rhombohedral, orthorhombic, and tetragonal phases plotted as a function of temperature.

Figure 3-6 plots the dielectric permittivities e_{ii}^{A}, where A refers to the phase and i refers to the x_i direction defined by the phase's local coordinate system. For both the tetragonal and rhombohedral phases, the dielectric permittivity in the two transverse directions e_{11} and e_{22} are identical in the phases' local coordinate systems. The dielectric properties associated with the present energy function show similar trends with Lv's energy function and are on the same order of magnitude. The vertical grey lines correspond to temperatures T_{RO}, T_{OT}, and T_C from left to right respectively.

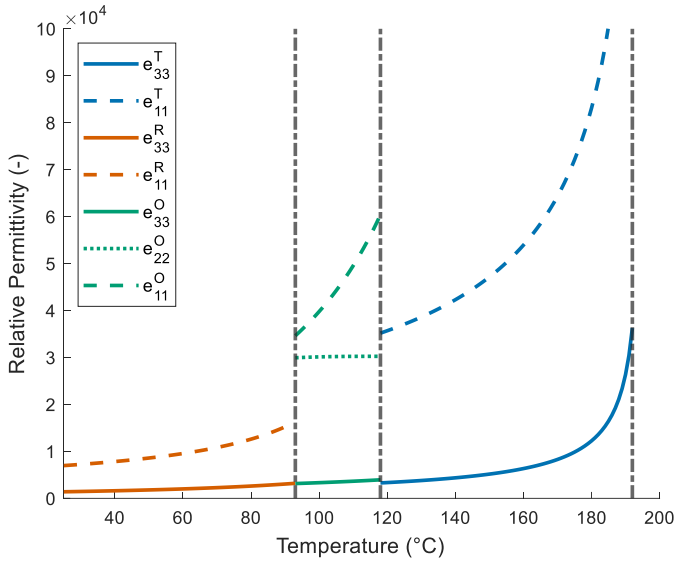

Figure 3-6: Relative permittivities e_{ii}^{A} ($i = 1, 2, 3$ and A: T, O, or R) plotted as a function of temperature.

IV. Switching and Phase Transitions

The energy barrier for domain switching or phase transition is the difference in energy between a the bottom of a variant's energy well and a neighboring saddle point. The application of an electrical and/or mechanical load will tilt the energy landscape. Energy wells will either deepen or diminish depending on the applied load(s). Domain switching or phase transitions will occur at some critical load. If random fluctuations are not considered, this will occur when a well disappears and the variant becomes unstable. At this point, the material will transition to a more energy favorable state.

A. Total Energy During Loading

The total energy is the sum of the Landau-Devonshire energy f_{LD}, gradient energy f_{grad}, electrical energy f_{elas}, and elastic energy f_{elas}:

$$f_{total} = f_{LD} + f_{grad} + f_{elec} + f_{elas} \tag{3-17}$$

This analysis will be focused on single domain crystals, so the gradient energy is assumed to be zero.

The electric energy due to an electric field $\boldsymbol{E} = (E_1, E_2, E_3)$ is

$$f_{elec} = -P_i E_i - \frac{1}{2} e_0 E_{ii}^2 \tag{3-18}$$

The first term is the change in potential energy due to the electric field acting on the material. The second term is from the free space occupied by the material. Since the second term is not dependent on the polarization and affects the whole energy landscape equally, this term is dropped from the following analysis.

The elastic energy is:

$$f_{elas} = \frac{1}{2} C_{ijkl} \varepsilon_{ij}^{el} \varepsilon_{kl}^{el} \tag{3-19}$$

where C_{ijkl} are components of the stiffness tensor, and ε_{ij}^{el} are components of the elastic strain. Here, the elastic strain is the total strain minus the spontaneous strain due to polarization:

$$\varepsilon_{ij}^{el} = \varepsilon_{ij}^{tot} - \varepsilon_{ij}^{0} = \varepsilon_{ij}^{tot} - Q_{ijkl} P_k P_l \tag{3-20}$$

where ε_{ij}^{tot} is the total strain and Q_{ijkl} are components of the electrostrictive tensor.

1. Loading Cases

The energies of four loading cases are considered below: 1) Applied electric field, 2) applied strain, 3) applied stress, and 4) applied stress and electric field.

1. Applied Electric Field:

Under applied electric field $\boldsymbol{E} = (E_1, E_2, E_3)$ with stress-free conditions, the energy of the system is described by the Helmholtz Energy:

$$f_{total}\left(P_i, E_i^{app}\right) = f_{LD}(P_i) - P_i E_i^{app} \tag{3-21}$$

2. Applied Strain

The free energy of the system under applied strain and applied stress will have different slightly different forms.

Under an applied total strain ε_{ij}^{tot}, the work done is $\sigma_{ij}\varepsilon_{ij}^{tot}$ and the energy of the system is:

$$f_{total} = f_{LD}(P_i) + \frac{1}{2}C_{ijkl}\varepsilon_{ij}^{el}\varepsilon_{kl}^{el} - \sigma_{ij}\varepsilon_{ij}^{tot} \tag{3-22}$$

where C_{ijkl} are components of the stiffness tensor and σ_{ij} are components of the stress tensor. Substitute the elastic strain and distribute:

$$f_{elas} = \frac{1}{2}C_{ijkl}\varepsilon_{ij}^{el}\varepsilon_{kl}^{el} = \frac{1}{2}C_{ijkl}(\varepsilon_{ij}^{tot} - Q_{ijmn}P_mP_n)(\varepsilon_{kl}^{tot} - Q_{klop}P_oP_p) \tag{3-23}$$

$$f_{elas} = \frac{1}{2}C_{ijkl}(\varepsilon_{ij}^{tot}\varepsilon_{kl}^{tot} + Q_{ijmn}P_mP_nQ_{klop}P_oP_p - \varepsilon_{kl}^{tot}Q_{ijmn}P_mP_n - \varepsilon_{ij}^{tot}Q_{klop}P_oP_p) \tag{3-24}$$

The last two terms are equivalent due to the symmetry of C_{ijkl} and can be combined.

$$f_{elas} = \frac{1}{2}C_{ijkl}(\varepsilon_{ij}^{tot}\varepsilon_{kl}^{tot} + Q_{ijmn}P_mP_nQ_{klop}P_oP_p - 2\varepsilon_{kl}^{tot}Q_{ijmn}P_mP_n) \tag{3-25}$$

$$= \frac{1}{2}C_{ijkl}\varepsilon_{ij}^{tot}\varepsilon_{kl}^{tot} + \frac{1}{2}C_{ijkl}Q_{ijmn}Q_{klop}P_mP_nP_oP_p - C_{ijkl}\varepsilon_{kl}^{tot}Q_{ijmn}P_mP_n \tag{3-26}$$

Thus the energy of the system with work $\sigma_{ij}\varepsilon_{ij}^{tot}$ can be described by

$$f_{total} = f_{LD}(P_i) + \frac{1}{2}C_{ijkl}\varepsilon_{ij}^{tot}\varepsilon_{kl}^{tot} + \frac{1}{2}C_{ijkl}Q_{ijmn}Q_{klop}P_mP_nP_oP_p - C_{ijkl}\varepsilon_{kl}^{tot}Q_{ijmn}P_mP_n - \sigma_{ij}\varepsilon_{ij}^{tot} \tag{3-27}$$

The stress σ_{ij} is found in terms the total strain and polarization by minimizing the energy with respect to the total strain:

$$\frac{\partial f\left(P_i, \varepsilon_{ij}^{tot}\right)}{\partial \varepsilon_{ij}^{tot}} = C_{ijkl}\varepsilon_{kl}^{tot} - C_{ijkl}Q_{klmn}P_mP_n - \sigma_{ij} = 0 \tag{3-28}$$

$$\sigma_{ij} = C_{ijkl}(\varepsilon_{kl}^{tot} - Q_{klmn}P_mP_n) \tag{3-29}$$

Using this,

$$f_{total} = f_{LD}(P_i) + \frac{1}{2}C_{ijkl}\varepsilon_{ij}^{tot}\varepsilon_{kl}^{tot} + \frac{1}{2}C_{ijkl}Q_{ijmn}Q_{klop}P_mP_nP_oP_p - C_{ijkl}\varepsilon_{kl}^{tot}Q_{ijmn}P_mP_n - C_{ijkl}(\varepsilon_{kl}^{tot} - Q_{klmn}P_mP_n)\varepsilon_{ij}^{tot} \tag{3-30}$$

$$f_{total}\left(P_i, \varepsilon_{ij}^{tot}\right) = f_{LD}(P_i) - \frac{1}{2}C_{ijkl}\varepsilon_{ij}^{tot}\varepsilon_{kl}^{tot} + \frac{1}{2}C_{ijkl}Q_{ijmn}Q_{klop}P_mP_nP_oP_p \tag{3-31}$$

The total energy of the system due to a prescribed strain can now described by as a function of P_i and ε_{ij}^{tot}.

3. Applied Stress

For the case of applied stress σ_{ij}^{app},

$$f_{total} = f_{LD} + f_{elas} - \sigma_{ij}^{app}\varepsilon_{ij}^{tot} = f_{LD}(P_i) + \frac{1}{2}C_{ijkl}\varepsilon_{ij}^{el}\varepsilon_{kl}^{el} - \sigma_{ij}^{app}\varepsilon_{ij}^{tot} \tag{3-32}$$

where $\sigma_{ij}\varepsilon_{ij}^{tot}$ is the work done on the system by a fixed stress when the strain changes.

Substituting the elastic strain as before:

$$f_{total} = f_{LD} + \frac{1}{2}C_{ijkl}\left(\varepsilon_{ij}^{tot} - \varepsilon_{ij}^{0}\right)(\varepsilon_{kl}^{tot} - \varepsilon_{kl}^{0}) - \sigma_{ij}^{app}\varepsilon_{ij}^{tot} \tag{3-33}$$

Minimize the energy with respect to strain and solve for ε_{ij}^{tot} in terms of σ_{ij}^{app} and P_i

$$\frac{\partial f_{total}}{\partial \varepsilon_{ij}^{tot}} = \frac{1}{2} C_{ijkl}(\varepsilon_{kl}^{tot} - \varepsilon_{kl}^{0}) + \frac{1}{2} C_{ijkl}\left(\varepsilon_{ij}^{tot} - \varepsilon_{ij}^{0}\right) - \sigma_{ij}^{app} = 0 \tag{3-34}$$

$$C_{ijkl}(\varepsilon_{kl}^{tot} - \varepsilon_{kl}^{0}) = \sigma_{ij}^{app} \tag{3-35}$$

Convert C_{ijkl}, σ_{ij} and ε_{ij} to Voigt notation:

$$C_{ij}\left(\varepsilon_{j}^{tot} - \varepsilon_{j}^{0}\right) = \sigma_{i}^{app} \tag{3-36}$$

Multiply by the compliance

$$S_{ki}C_{ij}\left(\varepsilon_{j}^{tot} - \varepsilon_{j}^{0}\right) = S_{ki}\sigma_{i}^{app} \tag{3-37}$$

$$\delta_{kj}\left(\varepsilon_{j}^{tot} - \varepsilon_{j}^{0}\right) = S_{ki}\sigma_{i}^{app} \tag{3-38}$$

$$(\varepsilon_{k}^{tot} - \varepsilon_{k}^{0}) = S_{ki}\sigma_{i}^{app} \tag{3-39}$$

$$\varepsilon_{k}^{tot} = S_{ki}\sigma_{i}^{app} + \varepsilon_{k}^{0} \tag{3-40}$$

Converting back from Voigt notation

$$\varepsilon_{kl}^{tot} = S_{klij}\sigma_{ij}^{app} + \varepsilon_{kl}^{0} \tag{3-41}$$

$$\varepsilon_{kl}^{tot} = S_{ijkl}\sigma_{ij}^{app} + Q_{ijkl}P_iP_j \tag{3-42}$$

where S_{ijkl} are components of the compliance tensor.

Substitute this back into Equation 3-33:

$$f_{total} = f_{LD}(P_i) + \frac{1}{2}\sigma_{kl}\left(S_{ijkl}\sigma_{ij} + Q_{ijkl}P_iP_j - Q_{ijkl}P_iP_j\right) - \sigma_{ij}^{app}\left(S_{ijkl}\sigma_{kl}^{app} + Q_{ijkl}P_kP_l\right) \tag{3-43}$$

Combining like terms:

$$f_{total}\left(P_i, \sigma_{ij}^{app}\right) = f_{LD}(P_i) - \frac{1}{2}S_{ijkl}\sigma_{ij}^{app}\sigma_{kl}^{app} - \sigma_{ij}^{app}Q_{ijkl}P_kP_l \tag{3-44}$$

4. Applied Stress and Electric Field

The energy of the system that describes both applied stress and electric field can be obtained by combining the results from Equations 3-21 and 3-44 together:

$$f\left(P_i, E_i, \sigma_{ij}^{app}\right) = f_{LD}(P_i) - \frac{1}{2} S_{ijkl} \sigma_{ij}^{app} \sigma_{kl}^{app} - \sigma_{ij}^{app} Q_{ijkl} P_k P_l - P_i E_i^{app} \tag{3-45}$$

2. Example: Loading in <001> without Electric Field

Consider uniaxial loading along the <001> direction without an electric field.

$$\sigma_{11}^{app} = \sigma_{22}^{app} = \sigma_{12}^{app} = \sigma_{23}^{app} = \sigma_{13}^{app} = 0, \sigma_{33}^{app} \neq 0 \tag{3-46}$$

Equation 3-45 becomes:

$$\begin{aligned} f\left(P_i, \sigma_{ij}^{app}\right) &= f_{LD}(P_i) - \frac{1}{2} S_{3333} \sigma_{33}^{app} \sigma_{33}^{app} - \sigma_{33}^{app} Q_{33kl} P_k P_l \\ f\left(P_i, \sigma_{ij}^{app}\right) &= f_{LD}(P_i) - \frac{1}{2} S_{3333} \sigma_{33}^{app} \sigma_{33}^{app} \\ &\quad - \sigma_{33}^{app} (Q_{3311} P_1^2 + Q_{3322} P_2^2 + Q_{3333} P_3^2 + 2Q_{3312} P_1 P_2 + 2Q_{3313} P_1 P_3 \\ &\quad + 2Q_{3323} P_2 P_3) \end{aligned} \tag{3-47}$$

This can be rewritten as:

$$\begin{aligned} f\left(P_i, \sigma_{ij}^{app}\right) &= f_{LD}(P_i) - \frac{1}{2} S_{3333} \sigma_{33}^{app} \sigma_{33}^{app} \\ &\quad - \sigma_{33}^{app} (Q_{11}(P_1^2 + P_2^2 + P_3^2) + 2Q_{12}(P_1 P_2 + P_1 P_3 + P_2 P_3)) \end{aligned} \tag{3-48}$$

Rewriting the energy specifically in the (110) plane where $P_1 = P_2 = P_{12}/\sqrt{2}$:

$$\begin{aligned} f\left(P_i, \sigma_{ij}^{app}\right) &= f_{LD}(P_i) - \frac{1}{2} S_{3333} \sigma_{33}^{app} \sigma_{33}^{app} \\ &\quad - \sigma_{33}^{app} \left(Q_{11}(P_1^2 + P_2^2 + P_3^2) + Q_{12}\left(P_{12}^2 + 2\sqrt{2} P_{12} P_3\right)\right) \end{aligned} \tag{3-49}$$

B. Energy Barrier and Stability

Each energy well corresponds to a phase/variant and has some energy barrier separating it from a neighboring well. For one phase or variant to transition to another, it needs to overcome said energy barrier.

1. Minima Identification and Energy Barrier Calculation

To determine the height of an energy barrier systematically, the critical points of the free energy function f_{total} must be identified.

Critical points can be identified by setting the energy stationary:

$$\left[\frac{\partial f}{\partial P_i}\right] = 0 \tag{3-50}$$

Generally, critical points can be classified as a local minima, maxima, and saddle points by examining the Hessian matrix:

$$H(P_k) = \left[\frac{\partial^2 f(P_k)}{\partial P_i \partial P_j}\right] \tag{3-51}$$

If the Hessian is positive definite (all eigenvalues are positive), then critical point is a local minimum. If the Hessian is negative definite (all eigenvalues negative), then the critical point is a local maximum. If the Hessian has both positive and negative eigenvalues, then the critical point is a saddle point. Otherwise, the test is inconclusive.

If the energy is written as a function of two variables P_{12} and P_3, then the critical points satisfy:

$$\begin{bmatrix} \dfrac{\partial f}{\partial P_{12}} \\ \dfrac{\partial f}{\partial P_3} \end{bmatrix} = 0 \tag{3-52}$$

The second derivative test to classify critical point of two variables (P_{12}, P_3):

1. If $\det H(P_{12}, P_3) = \frac{\partial^2 f}{\partial P_{12}^2}\frac{\partial^2 f}{\partial P_3^2} - \left(\frac{\partial^2 f}{\partial P_{12}\partial P_3}\right)^2 > 0$ and $\frac{\partial^2 f}{\partial P_{12}^2} > 0$, then (P_{12}, P_3) is a local minimum.
2. If $\det H(P_{12}, P_3) > 0$ and $\frac{\partial^2 f}{\partial P_{12}^2} < 0$, then (P_{12}, P_3) is a local maximum.
3. If $\det H(P_{12}, P_3) < 0$, then (P_{12}, P_3) is a saddle point.
4. If $\det H(P_{12}, P_3) = 0$, then the test is inconclusive.

The height of an energy barrier between A and B is the difference between the energy of at the phase's local minimum and the energy at a neighboring maximum or saddle point $f_{saddle/max}^{AB}$:

$$f_{barrier}^{A\to B} = f_{saddle/max}^{AB} - f_{\min}^{A} \tag{3-53}$$

Similarly, the energy barrier between

$$f_{bar}^{B\to A} = f_{saddle/max}^{AB} - f_{\min}^{B} \tag{3-54}$$

Note that the energy barrier from A to B is not the same as the energy barrier from B to A.

Figure 3-7 shows the energy landscape from Figure 3-3 with the critical points represented by red points. A depiction of the energy barriers from the rhombohedral phase to the neighboring tetragonal $f_{bar}^{R\to T}$ and orthorhombic phases $f_{bar}^{R\to O}$ is shown by the blue double arrows.

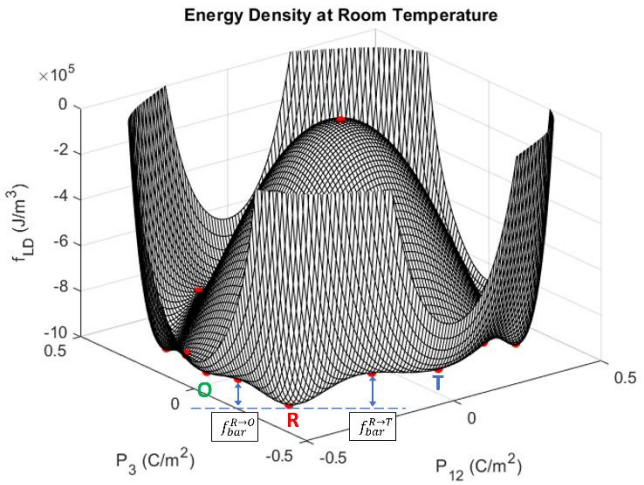

Figure 3-7: The critical points of the energy function are represented by red points on the energy landscape. The energy barriers of the rhombohedral phase to the neighboring tetragonal and orthorhombic phases are depicted by the blue double arrows.

Energy fluctuations or biases allow the material to overcome the energy barrier necessary for phase transformation. The effect of energy fluctuations was investigated by assuming a level of fluctuation energy f_{fluc}. For each well, the height of the energy barrier $f_{barrier}^{A\to B}$ is compared to f_{fluc}. If the energy barrier is greater than the fluctuation energy, then there is insufficient energy to transition from A to B. If the energy barrier is less than or equal to the fluctuation energy, then there is sufficient energy to transition from A to B. For the purposes of the following analysis, a well is considered "stable" if the fluctuation energy is less than the lowest energy barrier to exit that well.

C. Simulations of Applied Electric Field

The hysteresis behavior while loading is simulated for selected loading cases with and without fluctuations/biases. In the following plots, the points each correspond to what the model describes as stable phases. These points outline the hysteresis behavior of the material. Green

represents the orthorhombic phase, red represents the rhombohedral phase, and blue represents the tetragonal phase. Because there may be multiple stable wells and phases, the path of the hysteresis loop depends not only on the applied loads but the history as well.

1. E_{12} Along [110] Direction for Stress-free Crystal

The hysteresis behavior of the crystal while applying an electric field in the [110] direction is simulated following Equation 3-21. Here, $E_3 = 0$.

$$f_{total} = f_{LD}(P_{12}, P_3) - P_{12}E_{12} \tag{3-55}$$

$$\frac{\partial f_{total}}{\partial P_{12}} = \frac{\partial f_{LD}}{\partial P_{12}} - E_{12} = 0 \tag{3-56}$$

$$\frac{\partial f_{total}}{\partial P_3} = \frac{\partial f_{LD}}{\partial P_3} = 0 \tag{3-57}$$

Figure 3-8 plots the polarization P_{12} of the rhombohedral, orthorhombic, and tetragonal phases as an electric field is applied in the E_{12} [110] direction. Energy fluctuations that may cause the material to escape from a metastable well are not accounted for in this plot. Points correspond to stable phases between -3 and +3 MV/m, evaluated at 0.1 MV/m increments. The figure shows this energy function has a coercive field for switching between rhombohedral variants around +/- 1 MV/m. The coercive field for phase transition from the rhombohedral to orthorhombic phase occurs around +/- 1.8 MV/m. The transition to return from the orthorhombic phase to the rhombohedral phase is around -/+ 1.6MV/m. The tetragonal phase becomes unstable after the field exceeds +/- 0. 2 MV/m.

In this case, if the crystal starts in the rhombohedral phase, it can switch and revert between the rhombohedral variants as an electric field is cycled. However, if a sufficiently high electric field is applied and the rhombohedral phase transitions to the orthorhombic phase. The crystal will not revert to the original rhombohedral variant even after the applied field is completely released

and entirely skips the original rhombohedral variant because the metastable orthorhombic well remains stable. This is despite the rhombohedral phase being more energy favorable. This presents an issue for modeling devices that require the model to return to the original phase when releasing the applied load.

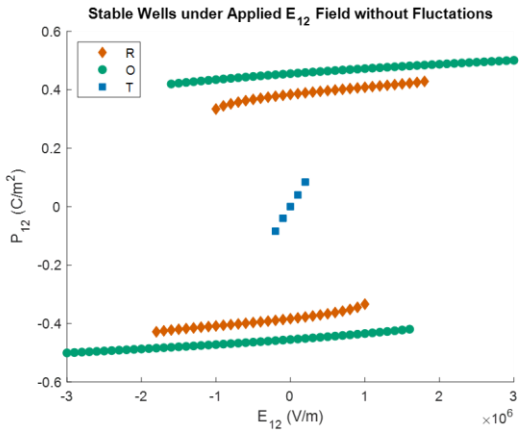

Figure 3-8: The P_{12} component of stable polarization plotted as a function the electric field applied in the E_{12} [110] direction ignoring energy fluctuations.

Figure 3-9 similarly plots the polarization P_{12} of the three phases, but also considers the effect of energy fluctuations on the order of 10-40 kJ/m^3. As the magnitude of the fluctuations increases, the number of stable wells decrease. This causes switching and phase transformations to occur earlier in the hysteresis loop. The tetragonal phase can be completely unstable depending on the fluctuation energy. The coercive field for switching between two R variants occurs at a lower magnitude, from around +/- 1MV/m to +/- 0.5-0.8 MV/m depending on the magnitude of the energy fluctuations. The field required to switch from rhombohedral to orthorhombic also decreases from around +/- 1.8 MV/m to less than +/- 1 MV/m. The orthorhombic to rhombohedral transition is no longer completely skipped and may return to the original phase when the load is released. With higher fluctuations, there is a band of electric fields where the fluctuations exceed

the energy barriers of all the phases. This may correspond with the region of phase coexistence observed in some ferroelectrics experimentally [34].

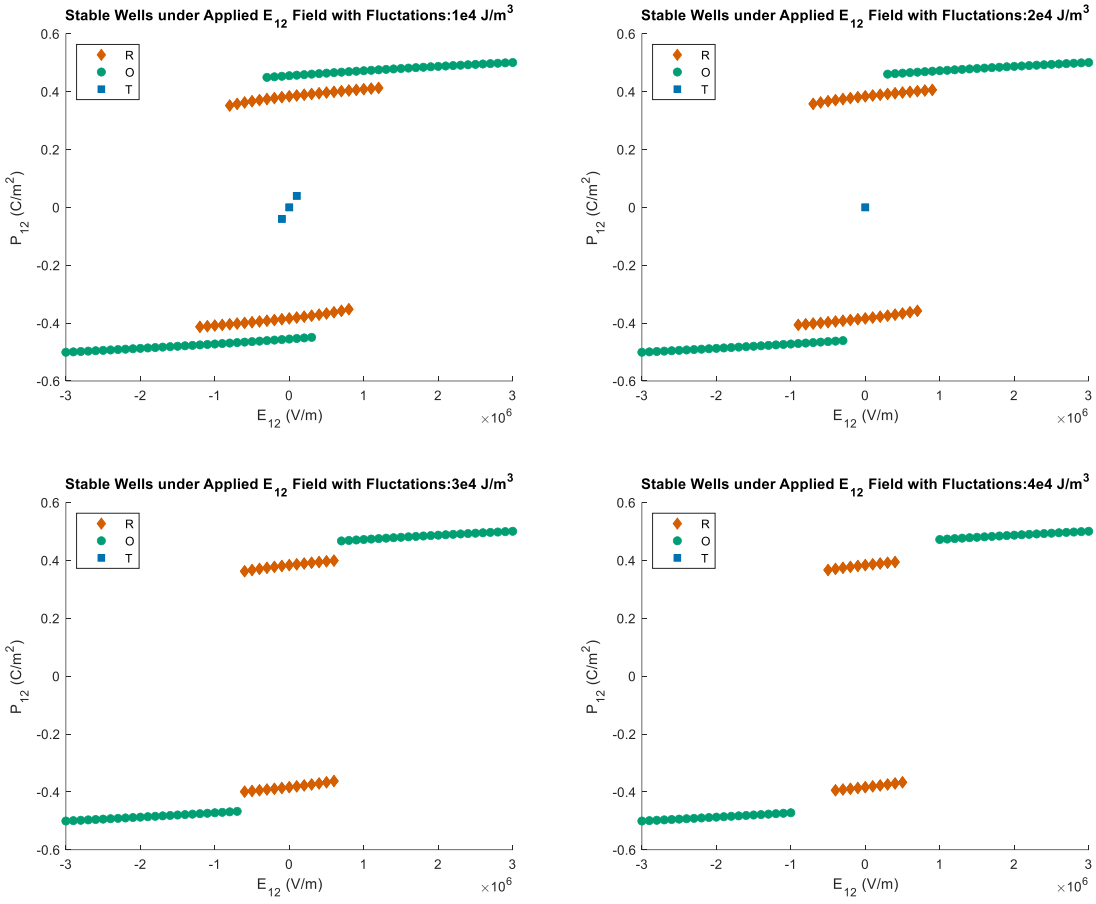

Figure 3-9: The P_{12} component of stable polarization plotted as a function the electric field applied in the E_{12} [110] direction considering energy fluctuations for 10-40 kJ/m^3.

2. E_3 Along [001] Direction for Stress-free Crystal

The hysteresis behavior of the crystal while applying an electric field in the [001] direction is simulated. Figure 3-10 plots the polarization P_3 of the rhombohedral, orthorhombic, and tetragonal phases as an electric field E_3 is applied in the [001] direction without considering energy fluctuations. The figure shows this energy function has a coercive field for switching between rhombohedral variants around +/- 0.61 MV/m. The coercive field for phase transition from the

rhombohedral to tetragonal phase occurs around +/- 1.9 MV/m. The transition to return from the tetragonal phase to the rhombohedral phase is around -/+ 0.9 MV/m. The orthorhombic phase becomes unstable after the field exceeds around +/- 0. 2 MV/m.

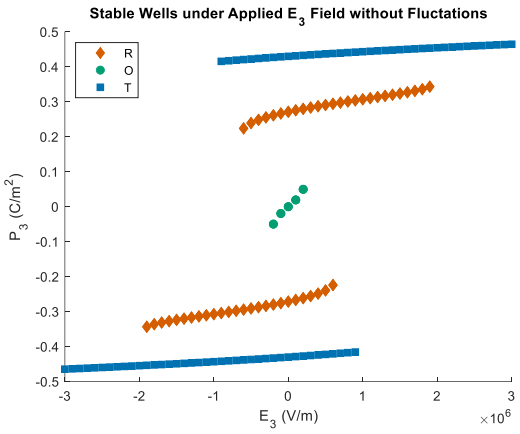

Figure 3-10: The P_3 component of stable polarization plotted as a function the electric field applied in the E_3 [001] direction ignoring energy fluctuations.

Figure 3-11 plots the polarization P_3 of the three phases considering the effect of energy fluctuations between 10-40 kJ/m^3. After accounting for fluctuation/bias, the coercive field for switching between two R variants occurs at a lower magnitude, from around +/- 0.6 MV/m to +/- 0.1-0.5 MV/m depending on the magnitude of the energy fluctuations. The field required to switch from rhombohedral to tetragonal also decreases from around +/- 1.9 MV/m to +/- 0.9 MV/m. The tetragonal to rhombohedral transition changes from -/+ 0.9 MV/m to +/- 0.3 MV/m.

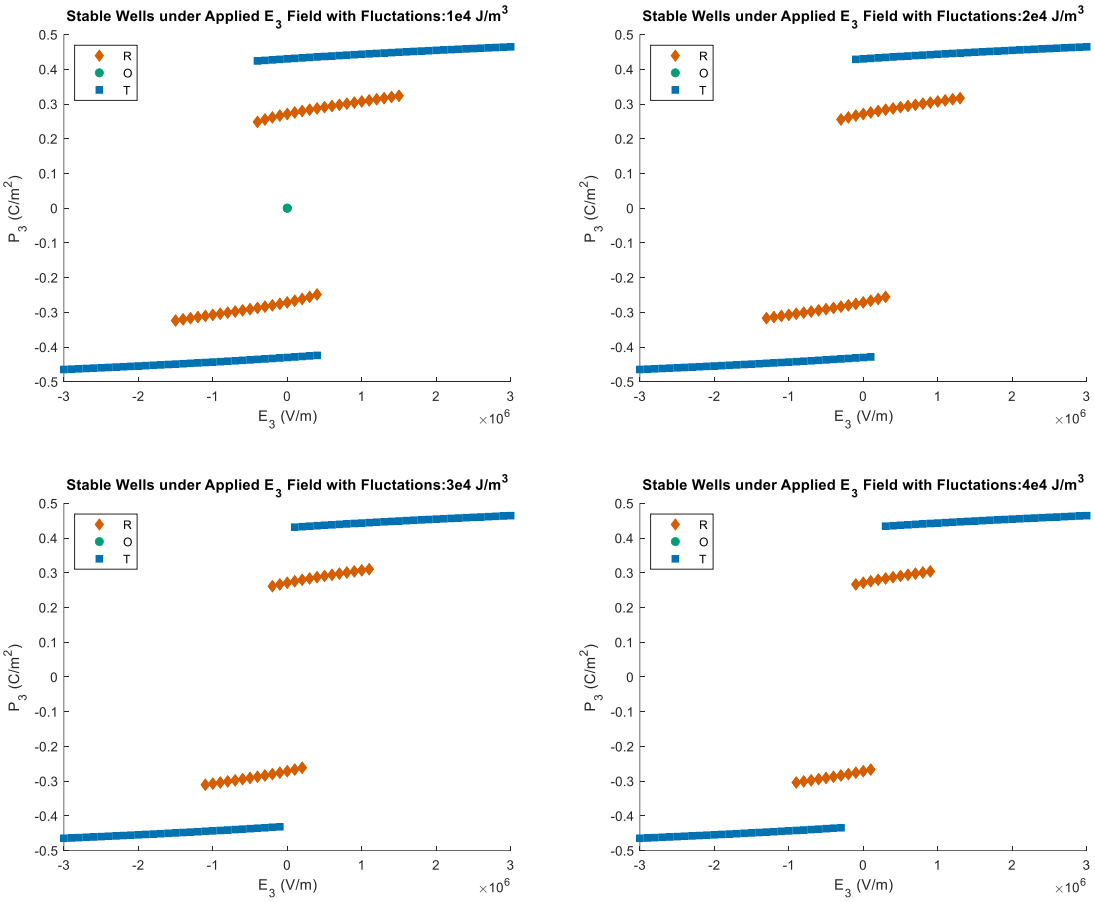

Figure 3-11: The P_3 component of stable polarization plotted as a function the electric field applied in the E_3 [001] direction considering energy fluctuations between 10-40 kJ/m^3.

V. Conclusion

The effects of energy fluctuations were shown to have a significant effect on the modeling of ferroelectric switching and phase transformations using a Landau-Devonshire energy function developed for single domain PIN-PMN-PT.

For this analysis, a new energy function with improved stability was required for the higher loading conditions needed to induce phase transformations. A proposed set of Landau coefficients was found through extensive fitting to experimental data following a similar process as Lv. Constraints on the highest order coefficients were introduced along with additional fitting

parameters for each dielectric permittivity. These fitting parameters were necessary to account for the composition differences between the composition of interest (rhombohedral near the MPB) and the reference data.

There are several challenges for accurately modeling switching and phase transformation. Models are known to get trapped in metastable states and overpredict the coercive field needed for switching compared to experiments due to the energy barrier between two phases. Real materials are assumed to be able to escape these wells due to thermal fluctuations or defects, but these fluctuation effects are often neglected in models. Since models without fluctuations can still capture switching behavior, this overprediction is often deemed acceptable.

However, certain phase transitions that are observed experimentally may be completely bypassed by the model due to a metastable well. This work showed that the bypassed phase transitions can be recovered by accounting for the energy fluctuations or biases, and that energy fluctuations or local biases can be used to tune the hysteresis loop to match measured behaviors previously unable to be modeled.

VI. Appendix

A. Process for Coefficient Determination

Rewrite the Landau energy function f_{LD} into the local coordinate system for each phase (1T, 1O, 1R):

$$f_{LD}(P_1, P_2, P_3) = f_{LD}^{T}(P_1^T, P_2^T, P_3^T) \tag{3-A-1}$$

$$f_{LD}(P_1, P_2, P_3) \rightarrow f_{LD}^{O}(P_1^O, P_2^O, P_3^O) \tag{3-A-2}$$

$$f_{LD}(P_1, P_2, P_3) \rightarrow f_{LD}^{R}(P_1^R, P_2^R, P_3^R) \tag{3-A-3}$$

The local coordinate system is defined such that the spontaneous polarization should be aligned with in the local x_3-direction. For relationships applicable for all three phases, a general superscript will be used. For example, in f_{LD}^{A}, A refers to any of the T, O, or R phases.

There are 15 coefficients for a 10th order Landau-Devonshire energy function. It is numerically inefficient to solve for all coefficients at the same time, so the coefficients were determined by numerically solve solving three systems of equations sequentially. Determined coefficients were used in subsequent sets to reduce the number of unknowns solved for at one time. Two coefficients, α_{11111} and α_{11122}, were not necessary to fit the energy function to the properties listed in Table 3-2 and were set to zero for convenience. Additionally, all the highest-order coefficients followed an additional constraint:

$$\alpha_{ijklm} \geq 0 \tag{3-A-4}$$

to ensure the energy function is thermodynamically stable.

The following systems of equations were constructed using three types of relationships:

1. Energy Equivalence

The spontaneous energies of two phases A and B are assumed to be equivalent during their phase transition at temperature T_{AB}:

$$f_{LD}^{A}\left(0,0,P_S^A(T_{AB})\right) = f_{LD}^{B}\left(0,0,P_S^B(T_{AB})\right) \tag{3-A-5}$$

For example, $f_{LD}^{R}\left(0,0,P_S^R(T_{RO})\right) = f_{LD}^{O}\left(0,0,P_S^O(T_{RO})\right)$ at the rhombohedral-orthorhombic transition temperature T_{RO}.

2. Local Minima

A spontaneous phase occurs at a local energy minimum. As a local minimum, the first derivative satisfies:

$$\frac{\partial f_{LD}^{A}}{\partial P_3^A}(0,0,P_S^A) = 0 \tag{3-A-6}$$

3. Dielectric Coefficient

The dielectric coefficient e_{ij}^{A} is related to the second derivative of the energy function by:

$$\frac{1}{e_{ij}^{A} e_0} = \frac{\partial^2 f_{LD}^{A}(0,0,P_S^A)}{\partial P_i^A \partial P_j^A} \tag{3-A-7}$$

A multiplier k_{ij}^{A} was used to get each e_{ij}^{A} to account for increased permittivity for compositions closer to the MPB. This multiplier also functioned as a fitting parameter to adjust the resulting energy function to match the expected phase transformations.

It is possible for a set of coefficients to have multiple solutions. In this case, the spontaneous polarization is used to determine which set coefficients to use in later steps. The polarization chosen should result in a smooth and gradual decrease in polarization as temperature is increased. Choosing an incorrect solution may result in later systems of equations to have no solution.

Coefficients are assumed to be temperature independent except for α_1. This first coefficient is approximated by the Curie-Weiss Law:

$$\alpha_1 = \frac{T - T_0}{2e_0 C} \tag{3-A-8}$$

where T is the temperature, T_0 is the Curie-Weiss temperature, $e_0$is the permittivity of free space, and C is the Curie constant. T_0 is typically slightly lower than T_C.

The coefficients α_{11}, α_{111}, and $\alpha_{1111}$are determined by the following set of equations based on the tetragonal phase:

$$\frac{\partial f_{LD}^T}{\partial P_3^T}\left(0,0,P_S^T(T_1)\right) = 0 \tag{3-A-9}$$

$$\frac{1}{e_{33}^T(T_1)e_0} = \frac{\partial^2 f_{LD}^T}{\partial (P_3^T)^2}\left(0,0,P_S^T(T_1)\right) \tag{3-A-10}$$

$$f_{LD}^T\left(0,0,P_S^T(T_C)\right) = 0 \tag{3-A-11}$$

$$\frac{\partial f_{LD}^T}{\partial P_3^T}\left(0,0,P_S^T(T_C)\right) = 0 \tag{3-A-12}$$

The first two equations respectively correspond to the energy minima and longitudinal dielectric coefficient e_{33}^T for a spontaneous tetragonal phase at temperature T_1. The third equation corresponds to the energy equivalence of the tetragonal and the reference cubic phases at the Curie temperature T_C, while the final equation corresponds to the energy minima of the cubic/tetragonal phase at T_C. There are now four equations and four unknowns. The unknowns α_{11}, α_{111}, α_{1111}, and $P_S^T(T_C)$ are solved for numerically.

With these known coefficients, the spontaneous polarization for the tetragonal phase at the orthorhombic-tetragonal phase transition $P_S^T(T_{OT})$ can be determined via:

$$\frac{\partial f_{LD}^T}{\partial P_3^T}\left(0,0,P_S^T(T_{OT})\right) = 0 \tag{3-A-13}$$

$P_S^T(T_{OT})$ is used to solve the next set of equations.

The coefficients α_{12}, α_{112}, α_{1112}, α_{1122}, and α_{11112} are determined by the following set of equations based on the tetragonal and orthorhombic phases:

$$\frac{1}{e_{11}^T(T_1)e_0} = \frac{\partial^2 f_{LD}^T}{\partial (P_1^T)^2}\big(0,0,P_S(T_1)\big) \tag{3-A-14}$$

$$\frac{\partial f_{LD}^O}{\partial P_3^O}\Big(0,0,P_S^O(T_2)\Big) = 0 \tag{3-A-15}$$

$$\frac{1}{e_{33}^O(T_2)e_0} = \frac{\partial^2 f_{LD}^O}{\partial (P_3^O)^2}\Big(0,0,P_S^O(T_2)\Big) \tag{3-A-16}$$

$$\frac{1}{e_{11}^O(T_2)e_0} = \frac{\partial^2 f_{LD}^O}{\partial (P_1^O)^2}\Big(0,0,P_S^O(T_2)\Big) \tag{3-A-17}$$

$$f_{LD}^O\Big(0,0,P_S^O(T_{OT})\Big) = f_{LD}^T\big(0,0,P_S^T(T_{OT})\big) \tag{3-A-18}$$

$$\frac{\partial f_{LD}^O}{\partial P_3^O}\Big(0,0,P_S^O(T_{OT})\Big) = 0 \tag{3-A-19}$$

The first equation corresponds to the transverse dielectric coefficient e_{11}^T for a spontaneous tetragonal phase at temperature T_1. The second equation corresponds to the energy minimum of the spontaneous orthorhombic phase at temperature T_2. The third and fourth equations respectively correspond to the longitudinal e_{33}^O and one of the transverse dielectric coefficients e_{11}^o at temperature T_2. The fifth equation corresponds to the energy equivalence of the spontaneous orthorhombic and tetragonal phases during phase transition at temperature T_{OT}. The final equation corresponds to the energy minimum of the spontaneous orthorhombic phase at temperature T_{OT}. With this, there are six equations and six unknowns. The unknowns α_{12}, α_{112}, α_{1112}, α_{1122}, α_{11112}, and $P_S^O(T_{OT})$ are solved for numerically.

The remaining coefficients α_{123}, α_{1123}, α_{11223}, and α_{11123} are determined by the following set of equations based on the orthorhombic and rhombohedral phases:

$$\frac{1}{e_{22}^{O}(T_2)e_0} = \frac{\partial^2 f_{LD}^{O}}{\partial (P_2^O)^2}\left(0,0,P_S^O(T_2)\right) \tag{3-A-20}$$

$$\frac{\partial f_{LD}^{R}}{\partial P_3^R}\left(0,0,P_S^R(T_3)\right) = 0 \tag{3-A-21}$$

$$\frac{1}{e_{33}^{R}(T_3)e_0} = \frac{\partial^2 f_{LD}^{R}}{\partial (P_3^R)^2}\left(0,0,P_S^R(T_3)\right) \tag{3-A-22}$$

$$\frac{1}{e_{11}^{R}(T_3)e_0} = \frac{\partial^2 f_{LD}^{R}}{\partial (P_1^R)^2}\left(0,0,P_S^R(T_3)\right) \tag{3-A-23}$$

The first equation corresponds to the other transverse dielectric coefficient e_{22}^{O} for the spontaneous orthorhombic phase at temperature T_2. The second equation corresponds to the energy minimum of the spontaneous rhombohedral phase at temperature T_3. The third and fourth equations respectively correspond to the longitudinal e_{33}^{R} and transverse e_{11}^{R} dielectric coefficients for the spontaneous rhombohedral phase at temperature T_3. With this, there are four equations and four unknowns. The coefficients α_{123}, α_{1123}, α_{11223}, and α_{11123} are solved for numerically.

The multipliers K_i^A will affect where the curves of the spontaneous energies of each phase intersects. Depending on the choice of the multipliers, the curves may intersect more than once. The parameters were chosen such that there would only be two phase transitions the interested temperature range: once at the rhombohedral-orthorhombic phase transformation temperature T_{RO} and once at the orthorhombic-tetragonal phase transformation temperature T_{OT}.

VII. References

[1] Viehland, D., Li, J. F., Jang, S. J., Cross, L. E., and Wuttig, M. "Glassy Polarization Behavior of Relaxor Ferroelectrics." *Physical Review B*, Vol. 46, No. 13, 1992, pp. 8013–8017. https://doi.org/10.1103/PhysRevB.46.8013.

[2] Sun, E., Zhang, S., Luo, J., Shrout, T. R., and Cao, W. "Elastic, Dielectric, and Piezoelectric Constants of Pb(In 1/2Nb1/2)O3-Pb (Mg1/3Nb 2/3)O3-PbTiO3 Single Crystal Poled along [011]C." *Applied Physics Letters*, Vol. 97, No. 3, 2010, pp. 30–33. https://doi.org/10.1063/1.3466906.

[3] Zhang, S., Li, F., Jiang, X., Kim, J., Luo, J., and Geng, X. "Advantages and Challenges of Relaxor-PbTiO3 Ferroelectric Crystals for Electroacoustic Transducers - A Review." *Progress in Materials Science*, Vol. 68, 2015, pp. 1–66. https://doi.org/10.1016/j.pmatsci.2014.10.002.

[4] Park, S. E., and Shrout, T. R. "Ultrahigh Strain and Piezoelectric Behavior in Relaxor Based Ferroelectric Single Crystals." *Journal of Applied Physics*, Vol. 82, No. 4, 1997, pp. 1804–1811. https://doi.org/10.1063/1.365983.

[5] Wada, S., Park, S.-E., Cross, L. E., and Shrout, T. R. "Engineered Domain Configuration in Rhombohedral PZN-PT Single Crystals and Their Ferroelectric Related Properties." *Ferroelectrics*, Vol. 221, No. 1, 1999, pp. 147–155. https://doi.org/10.1080/00150199908016449.

[6] Park, S. E., Wada, S., Cross, L. E., and Shrout, T. R. "Crystallographically Engineered BaTiO3 Single Crystals for High-Performance Piezoelectrics." *Journal of Applied Physics*, Vol. 86, No. 5, 1999, pp. 2746–2750. https://doi.org/10.1063/1.371120.

[7] Bell, A. J., and Cross, L. E. “A Phenomenological Gibbs Function for Batio3, Giving Correct e Field Dependence of All Ferroelectric Phase Changes.” *Ferroelectrics*, Vol. 59, No. 1, 1984, pp. 197–203. https://doi.org/10.1080/00150198408240090.

[8] Amin, A., Haun, M. J., Badger, B., Mckinstry, H., and Cross, L. E. “A Phenomenological Gibbs Function for the Single Cell Region of the PbZrO3:PbTiO3 Solid Solution System.” *Ferroelectrics*, Vol. 65, No. 1, 1985, pp. 107–130. https://doi.org/10.1080/00150198508008964.

[9] Haun, M. J., Furman, E., Jang, S. J., McKinstry, H. A., Cross, L. E. “Thermodynamic Theory of BiFeO 3 -PbTiO 3.” *Journal of Applied Physics*, Vol. 6, No. August 1998, 1987, p. 3331.

[10] Noheda, B., Cox, D. E., Shirane, G., Gonzalo, J. A., Cross, L. E., and Park, S. E. “A Monoclinic Ferroelectric Phase in the Pb(Zr1_xTix)O 3 Solid Solution.” *Applied Physics Letters*, Vol. 74, No. 14, 1999, pp. 2059–2061. https://doi.org/10.1063/1.123756.

[11] Vanderbilt, D., and Cohen, M. H. “Monoclinic and Triclinic Phases in Higher-Order Devonshire Theory.” *Physical Review B - Condensed Matter and Materials Physics*, Vol. 63, No. 9, 2001, pp. 1–9. https://doi.org/10.1103/PhysRevB.63.094108.

[12] Li, Y. L., Cross, L. E., and Chen, L. Q. “A Phenomenological Thermodynamic Potential for BaTiO 3 Single Crystals.” *Journal of Applied Physics*, Vol. 98, No. 6, 2005. https://doi.org/10.1063/1.2042528.

[13] Wang, Y. L., Tagantsev, A. K., Damjanovic, D., Setter, N., Yarmarkin, V. K., Sokolov, A. I., and Lukyanchuk, I. A. “Landau Thermodynamic Potential for BaTiO3.” *Journal of*

Applied Physics, Vol. 101, No. 10, 2007. https://doi.org/10.1063/1.2733744.

[14] Heitmann, A. A., and Rossetti, G. A. "Thermodynamics of Ferroelectric Solid Solutions with Morphotropic Phase Boundaries." *Journal of the American Ceramic Society*, Vol. 97, No. 6, 2014, pp. 1661–1685. https://doi.org/10.1111/jace.12979.

[15] Zhang, H., Lu, X., Wang, R., Wang, C., Zheng, L., Liu, Z., Yang, C., Zhang, R., Yang, B., and Cao, W. "Phase Coexistence and Landau Expansion Parameters for a 0.70Pb(M G1/3 N B2/3) O3-0.30PbTi O3 Single Crystal." *Physical Review B*, Vol. 96, No. 5, 2017, pp. 1–9. https://doi.org/10.1103/PhysRevB.96.054109.

[16] Lv, P., Wang, L., and Lynch, C. S. "A Phenomenological Thermodynamic Energy Function for PIN-PMN-PT Relaxor Ferroelectric Single Crystals." *Acta Materialia*, Vol. 137, 2017, pp. 93–102. https://doi.org/10.1016/j.actamat.2017.07.031.

[17] Lv, P., and Lynch, C. S. "Energetics of Domain Engineered Rhombohedral Ferroelectric Single Crystals." *Behavior and Mechanics of Multifunctional Materials and Composites 2017*, Vol. 10165, No. April 2017, 2017, p. 101650B. https://doi.org/10.1117/12.2263245.

[18] Lv, P., and Lynch, C. S. "Phase-Field Simulation of Domain Walls in Rhombohedral Ferroelectric Single Crystals." *Acta Materialia*, Vol. 155, 2018, pp. 245–252. https://doi.org/10.1016/j.actamat.2018.06.016.

[19] Chen, L. Q., and Shen, J. "Applications of Semi-Implicit Fourier-Spectral Method to Phase Field Equations." *Computer Physics Communications*, Vol. 108, Nos. 2–3, 1998, pp. 147–158. https://doi.org/10.1016/s0010-4655(97)00115-x.

[20] Schrade, D., Mueller, R., Xu, B. X., and Gross, D. "Domain Evolution in Ferroelectric

Materials: A Continuum Phase Field Model and Finite Element Implementation." *Computer Methods in Applied Mechanics and Engineering*, Vol. 196, Nos. 41–44, 2007, pp. 4365–4374. https://doi.org/10.1016/j.cma.2007.05.010.

[21] Su, Y., and Landis, C. M. "Continuum Thermodynamics of Ferroelectric Domain Evolution : Theory, Finite Element Implementation, and Application to Domain Wall Pinning." *Journal of the Mechanics and Physics of Solids*, Vol. 55, 2007, pp. 280–305. https://doi.org/10.1016/j.jmps.2006.07.006.

[22] Hu, H. L., and Chen, L. Q. "Computer Simulation of 90° Ferroelectric Domain Formation in Two-Dimensions." *Materials Science and Engineering A*, Vol. 238, No. 1, 1997, pp. 182–191. https://doi.org/10.1016/S0921-5093(97)00453-X.

[23] Hu, H.-L., and Chen, L.-Q. "Three-Dimensional Computer Simulation of Ferroelectric Domain Formation." *Journal of American Ceramic Society*, Vol. 81, 1998, pp. 492–500. https://doi.org/10.1111/j.1151-2916.1998.tb02367.x.

[24] Choudhury, S., Li, Y. L., Krill, C. E., and Chen, L. Q. "Phase-Field Simulation of Polarization Switching and Domain Evolution in Ferroelectric Polycrystals." *Acta Materialia*, Vol. 53, No. 20, 2005, pp. 5313–5321. https://doi.org/10.1016/j.actamat.2005.07.040.

[25] Zhang, W., and Bhattacharya, K. "A Computational Model of Ferroelectric Domains. Part I: Model Formulation and Domain Switching." *Acta Materialia*, Vol. 53, No. 1, 2005, pp. 185–198. https://doi.org/10.1016/j.actamat.2004.09.016.

[26] Song, Y. C., Soh, A. K., and Ni, Y. "Phase Field Simulation of Crack Tip Domain Switching

in Ferroelectrics." *Journal of Physics D: Applied Physics*, Vol. 40, No. 4, 2007, pp. 1175–1182. https://doi.org/10.1088/0022-3727/40/4/040.

[27] Wang, D., Wang, L., and Melnik, R. "Vibration Energy Harvesting Based on Stress-Induced Polarization Switching: A Phase Field Approach." *Smart Materials and Structures*, Vol. 26, No. 6, 2017. https://doi.org/10.1088/1361-665X/aa6e46.

[28] Indergand, R., Vidyasagar, A., Nadkarni, N., and Kochmann, D. M. "A Phase-Field Approach to Studying the Temperature-Dependent Ferroelectric Response of Bulk Polycrystalline PZT." *Journal of the Mechanics and Physics of Solids*, Vol. 144, 2020. https://doi.org/10.1016/j.jmps.2020.104098.

[29] Wang, J.-J., Wang, B., and Chen, L.-Q. "Understanding, Predicting, and Designing Ferroelectric Domain Structures and Switching Guided by the Phase-Field Method." *Annual Review of Materials Research*, Vol. 49, No. 1, 2019, pp. 127–152. https://doi.org/10.1146/annurev-matsci-070218-121843.

[30] Kingsland, M., Fthenakis, Z. G., and Ponomareva, I. "Role of Depolarization in the Polarization Reversal in Ferroelectrics." *Physical Review B*, Vol. 100, No. 2, 2019, p. 24114. https://doi.org/10.1103/PhysRevB.100.024114.

[31] Li, F., Zhang, S., Xu, Z., Wei, X., Luo, J., and Shrout, T. R. "Electromechanical Properties of Tetragonal Pb(In1/2Nb 1/2) O3-Pb(Mg1/3Nb2/3)O 3-PbTiO3 Ferroelectric Crystals." *Journal of Applied Physics*, Vol. 107, No. 5, 2010. https://doi.org/10.1063/1.3331407.

[32] Zhang, S., Liu, G., Jiang, W., Luo, J., Cao, W., and Shrout, T. R. "Characterization of Single Domain Pb(In0.5Nb0.5) O3-Pb(Mg1/3Nb2/3)O3-PbTiO 3 Crystals with Monoclinic Phase."

Journal of Applied Physics, Vol. 110, No. 6, 2011, pp. 0–4. https://doi.org/10.1063/1.3639316.

[33] Sun, E., Cao, W., Jian, W., and Han, P. "Complete Set of Material Properties of Single Domain 0.24Pb(In1/2Nb1/2)O3-0.49Pb(Mg1/3Nb2/3)O3-0.27PbTiO3 Single Crystal and the Orientation Effects." *Applied Physics Letters*, Vol. 99, No. 3, 2011, pp. 1–3. https://doi.org/10.1063/1.3615684.

[34] Wan, Q., Chen, C., and Shen, Y. P. "Effects of Stress and Electric Field on the Electromechanical Properties of Pb(Mg 1/3Nb 2/3)O 3-0.32PbTiO 3 Single Crystals." *Journal of Applied Physics*, Vol. 98, No. 2, 2005. https://doi.org/10.1063/1.1985979.

Chapter 4: Relaxor Ferroelectric Phase Field Model

I. Introduction

In the past century, piezoelectric and ferroelectric materials have found use in a wide range of devices as sensors, transducers, and actuators. There has been a constant hunt for better properties to improve the performance of such devices. Relaxor ferroelectrics (such as PMN-PT and PIN-PMN-PT) are known to exhibit excellent electromechanical properties for certain compositions near the morphotropic phase boundary (MPB). These compositions are a subject of great interest, and a better understanding of the underlying physics can help in the search for the next generation of relaxor ferroelectric materials. Thermodynamic energy functions (also called Landau or Landau-Devonshire energy functions) based on Landau's phase theory have been developed to describe the structural energy of ferroelectric materials as a function of polarization. Mesoscale phase-field models based on these energy functions have provided a powerful tool for investigating and understanding microstructural phenomena in ferroelectrics and guide device design.

Devonshire developed a 6^{th} order energy function for $BaTiO_3$ in 1949 that described its temperature-dependent phase transformations [1]. Since then, Landau-Devonshire energy functions have been developed for various other materials including PZT ($Pb[Zr_xTi_{1-x}]O_3$) [2], $PbTiO_3$, 0.70PMN-0.30PT ($x Pb(Mn_{1/3}Nb_{2/3})O_3$-$(1-x)PbTiO_3$) [3], and a composition of PIN-PMN-PT ($x Pb(In_{1/2}Nb_{1/2})O_3$-$y Pb(Mn_{1/3}Nb_{2/3})O_3$-$(1-x-y)PbTiO_3$) near the MPB that is rhombohedral at room temperature [4].

Phase-field models have been implemented using various computational methods including the semi-implicit Fourier spectral method [5], finite difference, and finite element method (FEM) [6,7]. Phenomena such as domain formation [8,9] and switching [10,11] have been

simulated and also used to study the effects such as mechanical strain, defects, grains, and domain walls [7,12–14].

There are discrepancies between the measured and predicted coercive fields from the energy functions. Kingsland et al. [15] used atomistic first principle simulations and found that the nearly an order magnitude difference between theoretical predictions and observed measurements may be due to strong residual depolarizing fields based on defects in the crystal lattice. Indergand et al. [14] found the addition of stochastic noise to the phase field model provided a more accurate prediction of the coercive field for bulk PZT.

Quenched fields have been observed to exist in relaxor ferroelectric materials and their relaxor characteristics are attributed to the presence of this short-range order. However, the nature of this short-range order has been debated for several decades now [16–18] and its origin is still not completely understood. The two main theories to explain the short-range order are: 1) random fields (RF) present throughout the material and 2) polar nanoregions (PNRs) within a non-polar matrix. Random field theory postulates that strong local fields can exist due to defects or uneven distribution of ions occupying the same space within the crystal lattice. Using PMN-PT as an example, these ions would be Mg^{2+} and Nb^{5+}. This has been implemented as static electric fields that vary randomly in magnitude and direction point by point in the mesh. In contrast, PNR-based models [19,20] randomly populate nanoregions within the model (corresponding to volume fraction around 0.3) that follow a different set of material properties. In contrast to both views, molecular dynamic simulations by Takenaka et al. [21,22] suggest that there is little to no non-polar matrix. Instead, there is a coexistence of dynamic and static polar nanodomains similar to the coexistence of the liquid and frozen phases in slush water.

This chapter presents an FEM-based phase-field model using a 10th energy function based on PIN-PMN-PT. The model uses the coefficients presented in Chapter 3 which provides improved stability over the previous energy function for PIN-PMN-PT necessary for some of the loading conditions considered in this work. The purpose of this work was not to weigh in on the debate of relaxor's origins, but rather on how to more accurately model phase transformations in ferroelectrics which are difficult to model due to the metastable states and energy barriers described in Chapter 3. Local variations/fluctuations are added through the addition of random and static electric fields similar to RF theory for relaxors [23], but are modified to vary region by region instead of point-by-point in the mesh. The trends in the behavior of electrically-induced and stress-induced phase transformations in works by Gallagher et al. [24] and Liu et al. [25] are reproduced. Prior phase-field modeling approaches were not able to model these experiments.

II. Methodology

This work builds on Lv and Lynch's phase field work on modeling ferroelectric relaxor rhombohedral single crystals [26] and uses the same normalization procedure to improve convergence. A more detailed formulation of FEM based phase field models can be found in Su and Landis' work [7].

A. Energies and Governing Equations

Landau phase theory assumes that the free energy of a system can be described analytically by an order parameter η_i

$$f_{Landau} = \alpha_{ij}\eta_i\eta_j + \alpha_{ijkl}\eta_i\eta_j\eta_k\eta_l + \cdots + \alpha_{ij\cdots qr}\eta_i\eta_j\cdots\eta_q\eta_r \tag{4-1}$$

For ferroelectrics, the Landau energy is also called the Landau-Devonshire energy f_{LD}, with polarization P_i as the order parameter. The Landau energy describes the structural free energy of

the crystal as a function of polarization, using the cubic phase as the reference state corresponding to zero energy.

The ferroelectric phase-field model needs to account for the gradient energy f_{grad}, elastic energy f_{elas}, and electric energy f_{elec}. The total energy density is thus:

$$f_{total} = f_{LD} + f_{grad} + f_{elas} + f_{elec} \tag{4-2}$$

A 10th order energy function was chosen to capture the phase transitions between the rhombohedral, orthorhombic, and tetragonal phases. In the following energy function, the indices (i=1,2,3) follow a Cartesian coordinate system aligned with the parent cubic phase.

$$\begin{aligned} f_{LD}(P_1,P_2,P_3) = {} & \alpha_1(P_1^2+P_2^2+P_3^2) + \alpha_{11}(P_1^4+P_2^4+P_3^4) + \alpha_{12}(P_1^2P_2^2+P_1^2P_3^2+P_2^2P_3^2) \\ & + \alpha_{111}(P_{1^6}+P_{2^6}+P_{3^6}) + \alpha_{112}\left(P_1^2(P_2^4+P_3^4)+P_2^2(P_1^4+P_3^4)+P_3^2(P_1^4+P_2^4)\right) \\ & + \alpha_{123}(P_1^2P_2^2P_3^2) + \alpha_{1111}(P_1^8+P_2^8+P_3^8) \\ & + \alpha_{1112}\left(P_1^6(P_2^2+P_3^2)+P_2^6(P_1^2+P_3^2)+P_3^6(P_1^2+P_2^2)\right) \\ & + \alpha_{1122}(P_1^4P_2^4+P_1^4P_3^4+P_2^4P_3^4) + \alpha_{1123}(P_1^2P_2^2P_3^4+P_1^2P_2^4P_3^2+P_1^4P_2^2P_3^2) \\ & + \alpha_{11111}(P_1^{10}+P_2^{10}+P_3^{10}) \\ & + \alpha_{11112}\left(P_1^8(P_2^2+P_3^2)+P_2^8(P_1^2+P_3^2)+P_3^8(P_1^2+P_2^2)\right) \\ & + \alpha_{11122}\left(P_1^6(P_2^4+P_3^4)+P_2^6(P_1^4+P_3^4)+P_3^6(P_1^4+P_2^4)\right) \\ & + \alpha_{11223}(P_1^4P_2^4P_3^2+P_1^4P_2^2P_3^4+P_1^2P_2^4P_3^4) \\ & + \alpha_{11123}(P_1^2P_2^2P_3^6+P_1^2P_2^6P_3^2+P_1^6P_2^2P_3^2) \end{aligned} \tag{4-3}$$

The coefficients found in Chapter 2 and listed in Table 4-1 below are used for the Landau energy used in the phase field model.

Table 4-1: Landau Coefficients of 10th order energy function. T is temperature in $°C$.

	Coefficient	Units		Coefficient	Units
α_1	$3.816 \times 10^4\ (T - 182)$	$C^{-2}\ m^2\ N$	α_{1122}	-1.534×10^9	$C^{-8}\ m^{14}\ N$
α_{11}	-1.212×10^7	$C^{-4}\ m^6\ N$	α_{1123}	-2.234×10^{10}	$C^{-8}\ m^{14}\ N$
α_{12}	-2.641×10^7	$C^{-4}\ m^6\ N$	α_{11112}	8.571×10^8	$C^{-10}\ m^{18}\ N$
α_{111}	9.428×10^7	$C^{-6}\ m^{10}\ N$	α_{11223}	6.518×10^{10}	$C^{-10}\ m^{18}\ N$
α_{112}	3.881×10^8	$C^{-6}\ m^{10}\ N$	α_{11123}	7.496×10^{10}	$C^{-10}\ m^{18}\ N$
α_{123}	2.916×10^9	$C^{-6}\ m^{10}\ N$	α_{11111}	0	$C^{-10}\ m^{18}\ N$
α_{1111}	3.180×10^7	$C^{-8}\ m^{14}\ N$	α_{11112}	0	$C^{-10}\ m^{18}\ N$
α_{1112}	-3.388×10^8	$C^{-8}\ m^{14}\ N$			

In index notation, the gradient energy (also known as exchange energy) can be written in terms of the gradient of the polarization field:

$$f_{grad} = \frac{1}{2} G_{ijkl} P_{i,j} P_{k,l} \tag{4-4}$$

This energy arises due to neighboring dipoles interacting with one another. The electric field of one dipole produces a force on the other. At the continuum level, if the polarization field is uniform, the forces will be balanced and the resulting gradient energy is zero. This term also influences the domain wall thickness in the model and can be understood as an energy penalty against large gradient in the polarization field. Values between 1 and 10 for the normalized gradient coefficient were used, corresponding to domain wall thickness between 1 and 10 nm in this model.

In index notation, the elastic energy is

$$f_{elas} = \frac{1}{2} C_{ijkl} \varepsilon_{ij}^{el} \varepsilon_{kl}^{el} \tag{4-5}$$

where C_{ijkl} refers to the material's stiffness and ε_{ij}^{el} refers to the elastic strain. In Voigt notation, the associated components of the stiffness matrix used in this study are $C_{11} = 120$ GPa, $C_{12} = 100$ GPa, and $C_{44} = 60$ GPa.

The elastic strain is the difference between the total strain ε_{ij} and spontaneous strain ε_{ij}

$$\varepsilon_{ij}^{el} = \varepsilon_{ij} - \varepsilon_{ij}^{0} = \varepsilon_{ij} - Q_{ijkl}P_kP_l \tag{4-6}$$

assuming that the spontaneous strain is due to electrostriction. The electrostriction coefficients used in Voigt notation are $Q_{33} = 0.066\ m^4/C^2$, $Q_{13} = -0.032\ m^4/C^2$, and $Q_{44} = 0.023\ m^4/C^2$.

In index notation, the electrical energy is

$$f_{elec} = -E_iP_i - \frac{1}{2}\kappa_0 E_{ii}^2 \tag{4-7}$$

The first term is the work of the electric field E_i acting on the polarization/dipole and the second term is the energy stored within the free space occupied by the material where κ_0 is the permittivity of free space.

Like in [26], the system is assumed to reach mechanical equilibrium instantaneously for a given polarization field and uses a quasi-static electromagnetic field approximation. Other assumptions include small deformations and rotations, negligible inertia and body force terms, and no volume charge density within the body. The resulting phase-field model has three governing equations (respectively mechanical equilibrium, Gauss's Law, and the time-dependent Ginzburg-Landau equation).

$$\begin{gathered} \sigma_{ij,j} = 0 \\ D_{i,i} = 0 \\ \frac{\partial P_i}{\partial t} = -L\left(\frac{\partial f_{total}}{\partial P_i} - \frac{\partial}{\partial x}\left(\frac{\partial f_{total}}{\partial P_{i,j}}\right)\right) \end{gathered} \tag{4-8}$$

where the stress σ_{ij} and electric displacement D_i can respectively be defined as the derivatives of the total energy with respect to the strain and electric fields:

$$\sigma_{ij} = \frac{\partial f_{total}}{\partial \varepsilon_{ij}} \tag{4-9}$$

$$D_i = -\frac{\partial f_{total}}{\partial E_i} \tag{4-10}$$

L is the mobility coefficient and is the reciprocal of the inverse mobility coefficient β. Typically, values on the order of 1×10^{-3} were used for β. The order of magnitude was reduced by 1 or 2 for some simulations to get a sharper switching or phase transition.

Some models also account for micro-stress ξ_{ji} and potential η_i [7,27,28]

$$\xi_{ji} = \frac{\partial f_{total}}{\partial P_{i,j}} \tag{4-11}$$

$$\eta_i = \frac{\partial f_{total}}{\partial P_i} \tag{4-12}$$

to develop the TDGL equation from a micro-force approach.

The FEM model solves for three independent variables (displacement u_i, electric potential ϕ, and polarization P_i) and requires certain boundary conditions to be satisfied. The boundary conditions for independent variables can be found by analyzing the surface integral terms in the variational statement found in Su and Landis' work [7]. The variational statement according to Su and Landis reads:

$$\int_V \beta_{ij}\dot{P}_j \delta P_i \, dV + \int_V \rho \ddot{u}_i \delta u_i \, dV + \int_V (\sigma_{ji}\delta\varepsilon_{ij} - D_i \delta E_i + \eta_i \delta P_i + \xi_{ji}\delta P_{i,j}) dV$$
$$= \int_V (b_i \delta u_i - q\delta\phi + \gamma_i \delta P_i) \, dV + \int_S \left(t_i \delta u_i - \omega\delta\phi + \xi_{ji} n_j \delta P_i\right) dS \tag{4-13}$$

where ω is the surface charge density, ξ_{ji} is a micro-stress tensor such that $\xi_{ji} n_j \dot{P}_i$ is the power density expended across surfaces by neighboring configurations, and γ_i is the external micro-force vector such that $\gamma_i \dot{P}_i$ is the power density expended on the material by external sources. For the purposes of determining boundary conditions, $P_{i,j}$ is considered as an independent variable in the

variational statement of the problem and $\delta\varepsilon_{ij}$ and δE_i need to be rewritten in terms of the independent variables.

For displacement, the boundary terms become:

$$\int_{\Gamma}(t_i - \sigma_{ji})\delta u_i = 0 \tag{4-14}$$

which requires the traction $t_i = \sigma_{ji}n_j$ or for the displacement u_i to be specified.

For electric potential ϕ:

$$\int_{\Gamma}(\omega - D_i n_i)\delta\phi \, d\Gamma = 0 \tag{4-15}$$

which requires the surface charge density $\omega = D_i n_i$ or for the electric potential ϕ to be specified.

For polarization:

$$\int_{\Gamma}\xi_{ji}n_j\delta P_i \, d\Gamma = 0 \tag{4-16}$$

which requires either the microforces acting normal at a boundary to be zero ($\xi_{ji}n_j = 0$) or for the polarization P_i to be specified.

The natural and essential boundary conditions are summarized in

Table 4-2 below.

Table 4-2: Summary of Boundary Conditions

Variable	Natural		Essential
u_i	$t_i - \sigma_{ji}n_j = 0$	OR	u_i prescribed
ϕ	$\omega - D_i n_i = 0$	OR	ϕ prescribed
P_i	$\xi_{ji}n_j = 0$	OR	P_i prescribed

1. Conversion to 2D Coordinate System

The following phase-field modeling work was conducted in the $(1\bar{1}0)_c$ plane belonging to the $\{1\bar{1}0\}_c$ family. Each plane in this family contains variants of the three phases of interest: with

two tetragonal (T) variants, two orthorhombic (O) variants, and four rhombohedral (R) variants. The variants contained in the $(1\bar{1}0)_c$ plane are listed in Table 3-3. Figure 4-1 shows how the $(1\bar{1}0)_c$ plane and phase directions fits in the cubic coordinate system.

Table 4-3: Phases and variants in the $(1\bar{1}0)_c$ plane

Phase	Variants
T	$[001], [00\bar{1}]$
O	$[110], [\bar{1}\bar{1}0]$
R	$[111], [\bar{1}\bar{1}\bar{1}], [11\bar{1}], [\bar{1}\bar{1}1]$

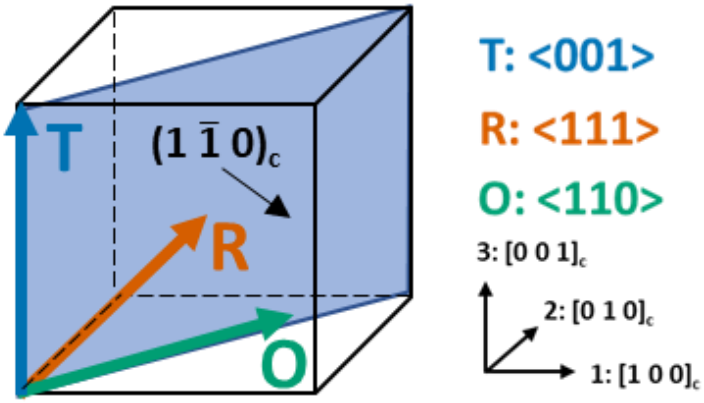

Figure 4-1: Cubic coordinate system showing the $(1\bar{1}0)_c$ plane containing the T, O, and R variants.

Figure 4-2 shows a 2D representation of the $(1\bar{1}0)_c$ plane and the conversion from 3D cubic coordinate system to 2D coordinate system, with x pointing out of plane. For this work, the alphabetical indices ($\alpha = y, z$) refer to the rotated 2D coordinate system. A lower-case p was also used to distinguish more readily the rotated and unrotated polarizations.

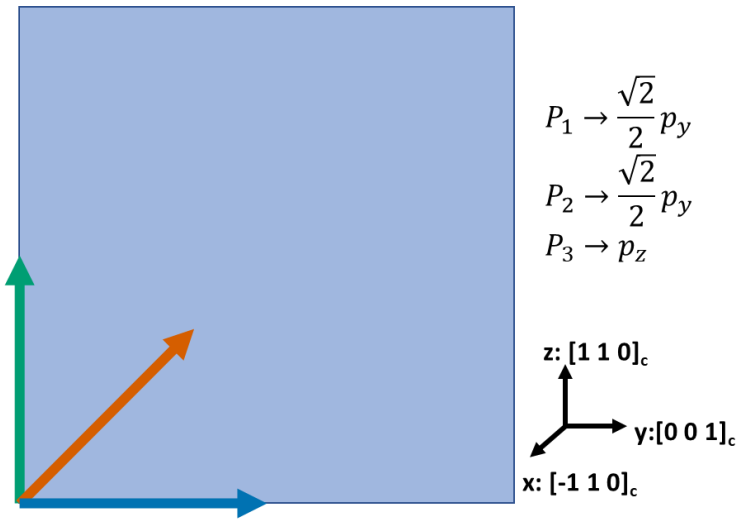

Figure 4-2: 2D coordinate system in $(1\bar{1}0)_c$ plane and conversion.

In this plane, the polarizations in the energy and governing equations can be transformed to the local coordinate system by relationships by substituting:

$$P_1 = P_2 = \frac{\sqrt{2}}{2} p_y \tag{4-17}$$

$$P_3 = p_z \tag{4-18}$$

In the 2D coordinate system, the Landau-Devonshire energy in Equation 4-3 becomes:

$$\begin{aligned} f_{LD} = {} & \alpha_1(p_y^2 + p_z^2) + \frac{1}{2}\alpha_{11}(2p_y^4 + p_z^4) + \frac{1}{4}\alpha_{111}(4p_y^6 + p_z^6) + \frac{1}{4}\alpha_{112}(4p_y^4p_z^2 + p_z^6 + 2p_y^2p_z^4) \\ & + \frac{1}{4}\alpha_{123}p_y^2p_z^4 + \frac{1}{8}\alpha_{1111}(8p_y^8 + p_z^8) + \frac{1}{8}\alpha_{1112}(2p_y^2p_z^6 + p_z^8 + 8p_y^6p_z^2) \\ & + \frac{1}{16}\alpha_{1122}(8p_y^4p_z^4 + p_z^8) + \frac{1}{4}\alpha_{1123}(p_y^4p_z^4 + p_y^2p_z^6) \\ & + \frac{1}{16}\alpha_{11112}(2p_y^2p_z^8 + p_z^{10} + 8p_y^8p_z^2) + \frac{1}{16}\alpha_{11223}(4p_y^4p_z^6 + p_y^2p_z^8) \\ & + \frac{1}{8}\alpha_{11123}(2p_y^6p_z^4 + p_y^2p_z^8) \end{aligned} \tag{4-19}$$

The gradient energy in Equation 4-4 becomes:

$$f_{grad} = \frac{1}{2} G\left(p_{y,y}^2 + p_{z,z}^2 + p_{y,z}^2 + p_{z,y}^2\right) \tag{4-20}$$

The elastic energy in Equation 4-5 becomes:

$$f_{elastic} = \frac{1}{2} C'_{11}\left(\varepsilon_{yy}^{el}\right)^2 + \frac{1}{2} C'_{22}(\varepsilon_{zz}^{el})^2 + C'_{23}\varepsilon_{yy}^{el}\varepsilon_{zz}^{el} + 2C'_{44}\left(\varepsilon_{yz}^{el}\right)^2 \tag{4-21}$$

where C'_{ij} are the rotated stiffness coefficients and $\varepsilon_{\alpha\beta}^{el}$ are the rotated elastic strains

$$\varepsilon_{\alpha\beta}^{el} = \frac{1}{2}\left(u_{\alpha,\beta} + u_{\beta,\alpha}\right) - \varepsilon_{\alpha\beta}^{0} \tag{4-22}$$

The spontaneous strains $\varepsilon_{\alpha\beta}^{0}$ are:

$$\begin{gathered} \varepsilon_{yy}^{0} = Q_{13}p_z^2 + Q_{33}p_y^2 \\ \varepsilon_{zz}^{0} = \frac{1}{2}(Q_{13} + Q_{33} + Q_{44})p_z^2 + Q_{13}p_y^2 \\ \varepsilon_{yz}^{0} = Q_{44}p_y p_z \end{gathered} \tag{4-23}$$

The unrotated stiffness and electrostrictive coefficeints in Voigt notation are listed in Table 4-4 below.

Table 4-4: Stiffness and Electrostrictive Coefficients

Parameter	Value	Units
C_{11}	120	GPa
C_{12}	100	GPa
C_{44}	60	GPa
Q_{33}	0.066	m^4/C^2
Q_{13}	-0.032	m^4/C^2
Q_{44}	0.023	m^4/C^2

The electric energy in Equation 4-7 becomes:

$$f_{elec} = -E_y p_y - E_z p_z - \frac{1}{2}\kappa_0\left(E_y^2 + E_z^2\right) \tag{4-24}$$

The electric field is related to the electric potential ϕ by

$$E_y = -\phi_{,y} \text{ and } E_z = -\phi_{,z} \tag{4-25}$$

The transformed governing equations from Equations 4-8 become:

$$\begin{gathered} \sigma_{\alpha\beta,\beta} = 0 \\ D_{\alpha,\alpha} = 0 \\ \frac{\partial p_\alpha}{\partial t} = -L\left(\frac{\partial f_{total}}{\partial p_\alpha} - \frac{\partial}{\partial x_\beta}\left(\frac{\partial f_{total}}{\partial p_{\alpha,\beta}}\right)\right) \end{gathered} \tag{4-26}$$

B. Boundary Conditions

Boundary conditions for a few example cases are illustrated below. For the problem to be well-defined, each boundary must have BCs to satisfy Equations 4-14, 4-15, and 4-16. Table 4-5 is the 2D version of

Table 4-2 with Greek indices $\alpha = y, z$ summarizing the natural and essential boundary conditions for a well-defined problem.

Table 4-5: Summary of Boundary Conditions (2D)

Variable	Natural		Essential
u_α	$t_\alpha - \sigma_{\beta\alpha} n_\beta = 0$	OR	u_α prescribed
ϕ	$\omega - D_\alpha n_\alpha = 0$	OR	ϕ prescribed
P_α	$\xi_{\beta\alpha} n_\beta = 0$	OR	P_α prescribed

1. Example: Periodic Representative Volume Element (RVE)

Consider a material that is under a compressive traction preload t_0 and an applied electric field $E_{app}(t)$ across the top and bottom surfaces. This can be modeled as a RVE with periodic boundary conditions. Figure 4-3 shows a schematic of the RVE. The figure also illustrates how corresponding points on opposite boundaries of the RVE are coupled.

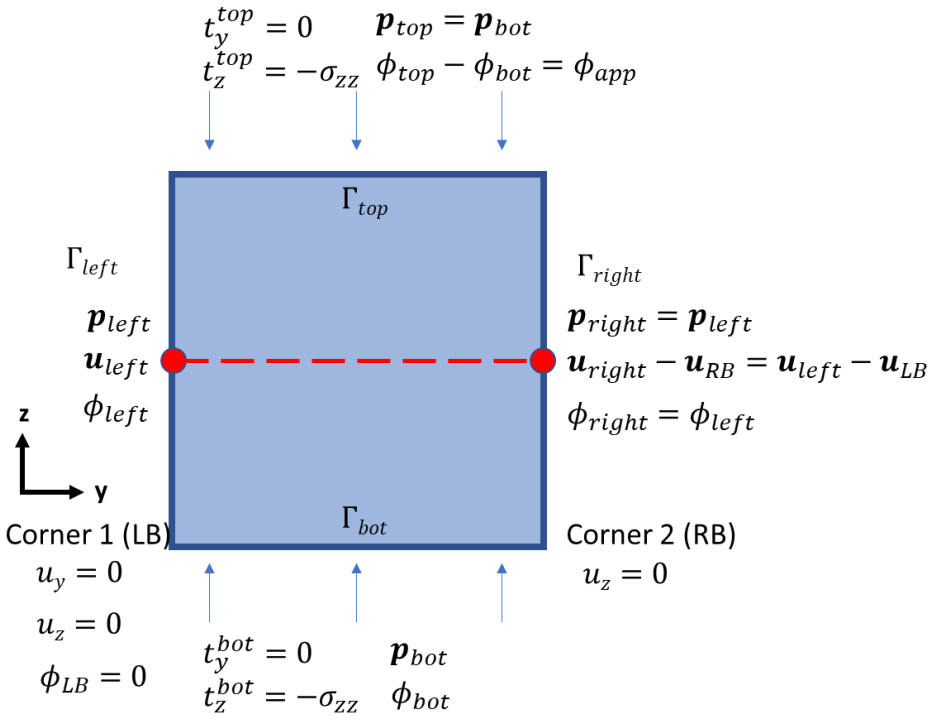

Figure 4-3: Schematic of an example RVE used in this work. Boundary conditions for the displacement and electric potential need to be chosen to allow for periodicity without artificially pinning the system. The dashed line shows how points on the right and left boundaries correspond to each other.

For polarization, standard periodic conditions are respectively used to map the polarizations for each point along the right/top boundaries to corresponding points on the left/bottom boundaries:

$$\boldsymbol{p}_{left} = \boldsymbol{p}_{right} \tag{4-27}$$

$$\boldsymbol{p}_{bot} = \boldsymbol{p}_{top} \tag{4-28}$$

Similarly, for the electric potential ϕ, standard periodic conditions are applied on the left and right boundaries:

$$\phi_{left} = \phi_{right} \tag{4-29}$$

However, applying this type of periodic condition for the top and bottom boundaries would be inconsistent with the applied electric field. Instead, the following relationship is used to prescribe the potential difference ϕ_{app} across the bottom and top boundaries for the applied electric field E_{app}:

$$\phi_{top} - \phi_{bot} = \phi_{app} = E_{app} \cdot h_{RVE} \tag{4-30}$$

where h_{RVE} is the distance between the bottom and top boundaries of the RVE.

For displacements, standard periodic conditions result in the zero strain conditions, so periodic conditions that allow for nonzero strains based on [29] (Smit et al 1998) are necessary. These periodic boundary conditions are applied to the left and right boundaries as:

$$\boldsymbol{u}_{left} - \boldsymbol{u}_{LB} = \boldsymbol{u}_{right} - \boldsymbol{u}_{RB} \tag{4-31}$$

where $\boldsymbol{u}_{left/right}$ are the displacements that corresponding to the left and right sides, $\boldsymbol{u}_{LB}$ is the displacement of the left bottom corner, and $\boldsymbol{u}_{RB}$is the displacement of the right bottom corner. Similar displacement boundary conditions would be used to prescribe displacements for the top and bottom boundaries if the tractions are not known:

$$\boldsymbol{u}_{bot} - \boldsymbol{u}_{LB} = \boldsymbol{u}_{top} - \boldsymbol{u}_{LT} \tag{4-32}$$

where $\boldsymbol{u}_{LT}$ is the displacement of the top/left corner.

To satisfy the natural boundary condition for displacement,

$$t_\alpha = \sigma_{\beta\alpha} n_\beta \tag{4-33}$$

In this case, the normal vectors are $\boldsymbol{n}^{top} = \begin{bmatrix} 0 \\ 1 \end{bmatrix}$ and $\boldsymbol{n}^{bot} = \begin{bmatrix} 0 \\ -1 \end{bmatrix}$. For periodicity, the tractions on opposite boundaries of the RVE should have the same magnitude and opposite signs ($t_z^{top} = -t_0$ and $t_z^{bot} = t_0$ for compression in z).

The following pointwise constraints on the bottom left (LB) and bottom right (RB) corners were added to prevent free translation and rotations:

$$\boldsymbol{u}_{LB} = \mathbf{0} \tag{4-34}$$

$$u_y^{RB} = 0 \tag{4-35}$$

2. Example: Non-RVE at surface.

Consider a section at the surface of the material under loading in the y ([001]) direction as described by Figure 4-4.

For polarization, the same periodic conditions are used in z to relate the top and bottom surfaces. For the right boundary, the polarizations are assumed to be free. For the left boundary, the vertical component of polarization is assumed to be free, but the normal component is zero. This is to satisfy continuity in the normal component of the electric displacement across boundary.

For electric potential, all boundaries are assumed to have the same potential since there is no electric field applied in either direction.

For displacements, the bottom left corner is fixed in both directions to prevent translation, and the bottom right corner is fixed in z to prevent rotations. The left boundary is fixed in y, but free along z.

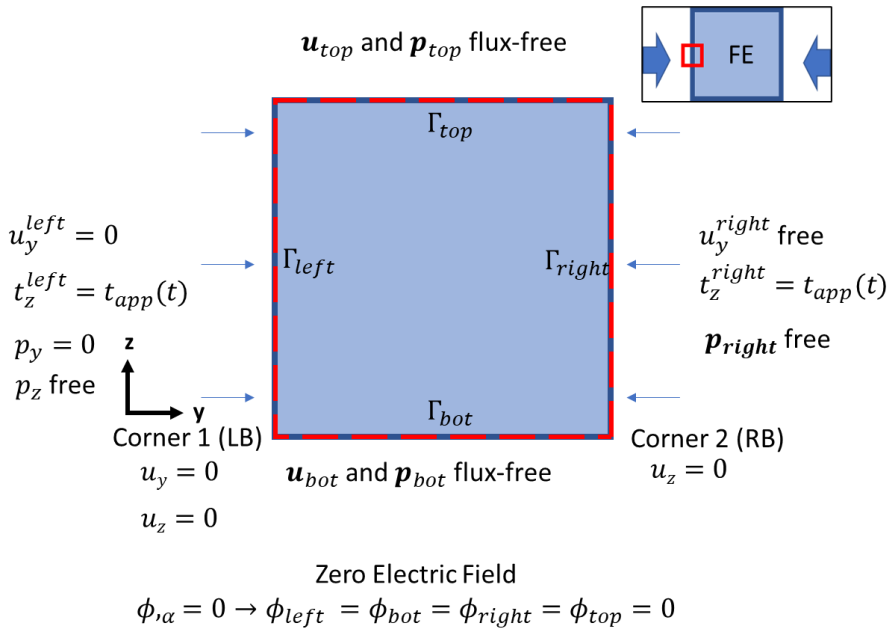

Figure 4-4: Schematic of a material under mechanical loading along y, where Γ_{left} is the surface of the material.

C. Local Fluctuations, Random Fields, and Biases

Chapter 3 showed that energy fluctuations or biases may be necessary for models to reproduce certain hysteresis phase transition trends. Ferroelectric phase field models often introduce small-amplitude noise terms during initialization to help the model escape unstable equilibrium states/phases (such as the cubic phase). However, though these small-amplitude noise terms may allow models to escape unstable equilibrium states, they are not sufficiently large enough for the model to cross the energy barrier necessary to escape metastable states.

These effects can be implemented in a variety of ways. For example, through a time-varying thermal noise or localized random fields throughout the material.

1. Time-varying Noise (added to TDGL)

A time-varying noise would more closely simulate the effects of thermal fluctuations. Prior works have introduced a noise term to the TDGL (or Allen-Cahn) equation based on thermal lattice vibrations following statistical mechanics-based approach [14,30–32]. Stochastic phase field models have been used to model the microstructural evolution in magnetic materials [33], effects grain boundary motion on material properties in crystalline materials [34], and earlier domain nucleation and polarization reversal in polycrystalline PZT [14].

The noise term η^{noise} is added to the TDGL equation:

$$\frac{\partial P_\alpha}{\partial t} = -L\left(\frac{\partial f_{total}}{\partial P_\alpha} - \frac{\partial}{\partial x_\beta}\left(\frac{\partial f_{total}}{\partial P_{\alpha,\beta}}\right)\right) + \eta_\alpha^{noise} \tag{4-36}$$

For the noise to be uncorrelated in space and time, the variance of this noise term was determined by Indergand to follow [14]:

$$|\eta|^2 = \frac{2k_B T}{\mu V_{char}\Delta t} \tag{4-37}$$

where k_B is the Boltzmann constant, T is the temperature, μ is the inverse mobility, $V_{char}$is the characteristic volume of the perovskite's unit cell, and Δt is the time step size.

2. Static Random Field and Biases

Relaxor behavior in ferroelectric materials is often attributed to local short-range order throughout the material. Quenched electric fields have been theorized and confirmed to exist [35], but the exact origins/mechanisms of relaxor ferroelctricity are still under debate. Relaxor phase-field models typically account for these variations in one of two ways: 1) random field (RF) theory and 2) polar nanoregions (PNR). These two cases are illustrated by Figure 4-5. In RF theory, local electric fields are assumed to exist throughout the material due to order-disorder of inherent to

materials like PMN. Models that use RF theory apply static electric fields locally where each node has a random magnitude and direction following a Gaussian distribution. In contrast to this, PNR traditionally assumes there are nanodomains fixed within a nonpolar matrix. This has been modeled by applying a different set of material parameters for the polar nanoregions. (Molecular dynamics simulations by Takenaka et al. [21,22] showed a lack of a major nonpolar matrix, but clusters of dynamic polar nanodomains throughout the materials.) This work does not weigh in on the debate but adopts an approach that can be adapted to either explanation.

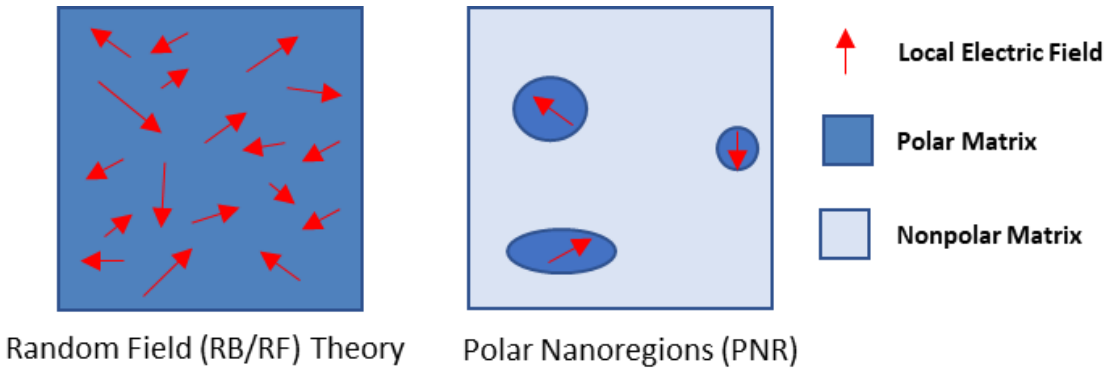

Figure 4-5: Local electric fields for RF (Left) and PNR (Right).

Similar to Ref. [23], the electric field in Equation 4-25 is modified to include random contributions to the electric field E_α^{rand} or other local biases E_α^{bias}.

$$E_\alpha = \phi_{,\alpha} + E_\alpha^{rand} + E_\alpha^{bias} \tag{4-38}$$

$$E_\alpha^{rand}(y,z) = E_0(y,z) \cdot Rn_i(y,z) \tag{4-39}$$

where E_0^2 is the variance of the electric field and Rn_i is a random function with Gaussian distribution centered about 0 and standard deviation of 1. A Gaussian distribution can be obtained following the Box-Muller formula [36] (Box and Muller 1958) using random values U_1 and U_2 with uniform distribution on interval (0,1):

$$Rn_x = (-2\log_e U_1)^{\frac{1}{2}} \cos 2\pi U_2 \tag{4-40}$$

$$Rn_y = (-2\log_e U_1)^{\frac{1}{2}} \sin 2\pi U_2 \tag{4-41}$$

In [23], the field changes at each node, which makes the results mesh-dependent and harder to evaluate mesh convergence. Instead, a parameter for region size was introduced to the model and the electric field was evaluated for a given region. Figure 4-6 and Figure 4-7 both show an example of the local random electric field distribution for a 10 nm x 10 nm RVE for two mesh sizes. In Figure 4-6, the random fields are evaluated for each node for mesh sizes of 2.5 and 1.25 squares. While the finer mesh shares all the fields of the larger mesh at the common nodes, it also introduces significantly distinct fields at all the other points. Contrast this with Figure 4-6 which evaluates the random field in regions about 2.5 nm in size for mesh sizes of 1.25 and 0.5 nm. Though there may be slight differences, the distributions largely remain the same even when changing the mesh density.

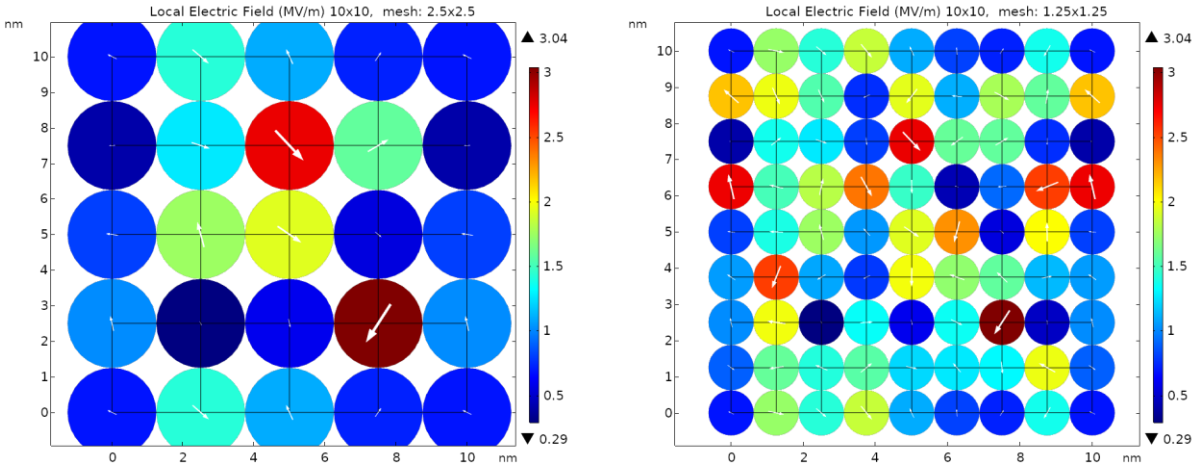

Figure 4-6: Local random field distribution for case for two mesh sizes evaluated at each node.

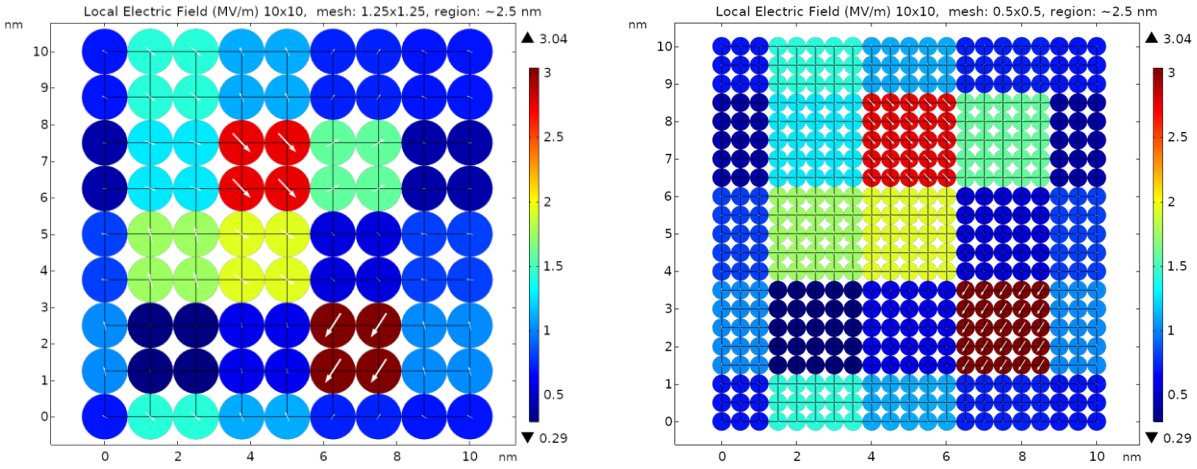

Figure 4-7: Local random fields distribution for two mesh sizes evaluated by regions.

For a nonpolar matrix, a multiplier can also be used to zero the electric field depending on volume fraction of the polar and non-polar matrices.

III. Results

A. Baseline: Hysteresis Without Fluctuation or Local Biases

Figure 4-8 shows the electric displacement's D_z hysteresis loop as an electric field E_z is applied across the material from without accounting for any biases or fluctuations. This case is used as a baseline to compare the effects of including fluctuations or local biases into the phase field model. An RVE is used for a stress-free single domain crystal. The model is first initialized in the rhombohedral phase and allowed to relax in a prior step before cycling through the electric field (in MV/m) from $0 \rightarrow 10 \rightarrow -10 \rightarrow 0$ twice.

The crystal is predicted to transition from R to O around 1.9 MV/m, and then switch from one O variant to another at around -3.5 MV/m. Comparing this hysteresis curve to the one constructed by analyzing stable/metastable wells in Chapter 3 (Figure 3-8). While the switching from R to O occurs around the same electric field (both around 1.8-1.9 MV/m), the predicted switching between the two O variants is not close at all (-1.6 MV/m compared to -3.5 MV/m with

a discrepancy of 1.9 MV/m). This discrepancy may be due to equilibrium states that are neither stable nor metastable. Examples of unstable equilibrium states would be at a local maximum or saddle point. Some sort of perturbation would be required.

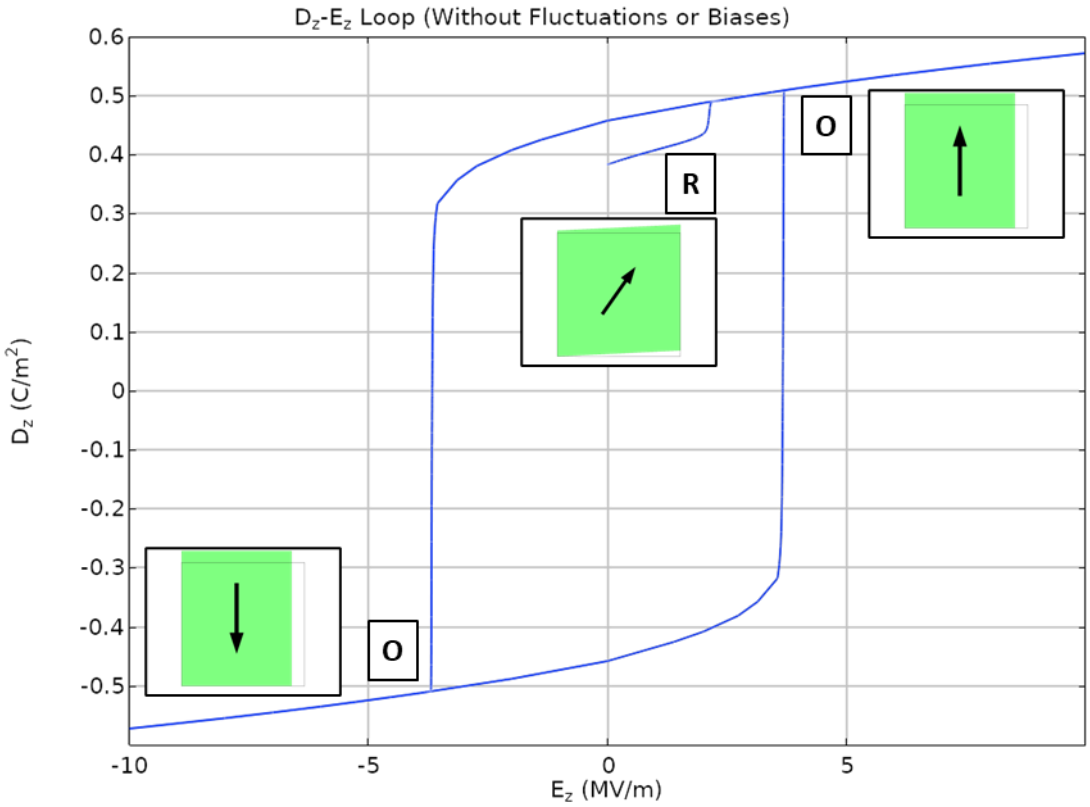

Figure 4-8: DE hysteresis loop without including local biases or fluctuations.

B. Time-varying Noise Term to TDGL

The effect of introducing the noise on the model was assessed using a RVE of a single crystal without preload or an applied electric field. The model was first initialized in the orthorhombic phase and allowed to relax. Figure 4-9 shows the polarization history of the RVE (averaged over RVE). For the simulation, the variance of the polarization noise from Equation was scaled down by two orders of magnitude to behave more similarly to a "slush" phase of the coexistence of frozen and dynamic domains in Takenaka's analogy with water phases [22].

Without scaling the fluctuation down, the model would constantly fluctuate between the different phases and behave more similarly to H-bonded water which also has fluctuating domain formation and changes in size.

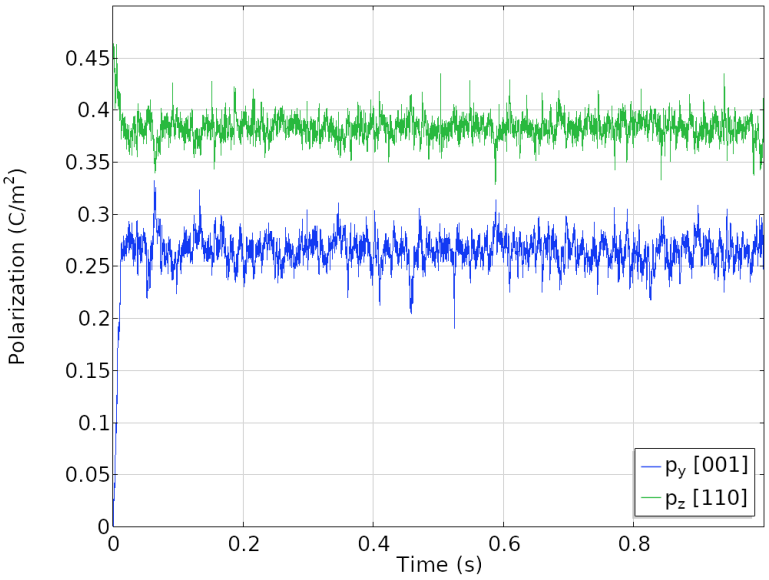

Figure 4-9: Polarization history of a single crystal RVE with time-varying noise.

After the RVE was allowed to relax, an electric field was applied to induce an R to O phase transformation and then released for two cycles. In the first cycle, the RVE stayed in the O phase, and only returned to the R phase while unloading in the second cycle.

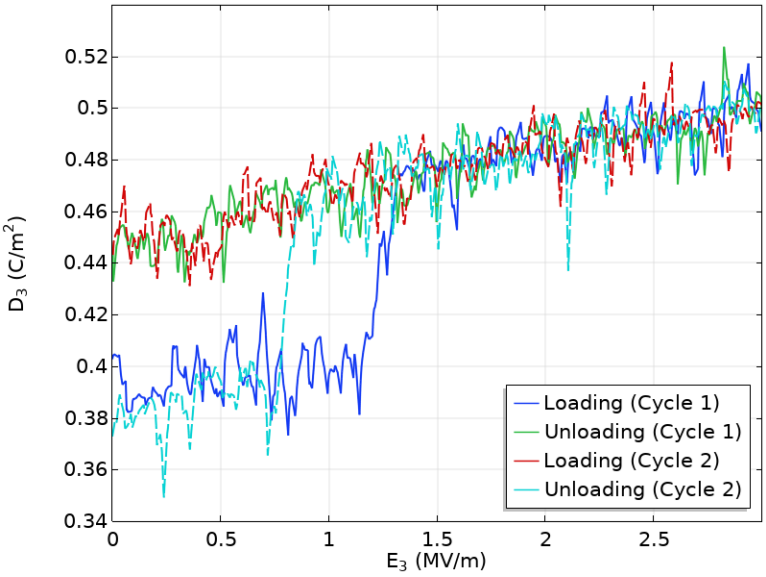

Figure 4-10: Electrically induced phase transformation with time-varying noise. The reversion from O to R occurs in one cycle but not the other due to the random nature.

While the implementing fluctuations in this manner can produce phase transition that is closer to experiments, the model does not reliably switch or change phases and the simulation time is significantly increased. Another implementation of the fluctuation would be necessary for more complex simulations.

C. Local Random Field

Instead of a time varying noise added to the TDGL equation, a local and static random field is used instead. This is simpler for the model in terms of convergence since this field does not vary in time.

1. Uniform Bias Field

Before showing the effect of a random field distribution, the effect of a uniform bias field on the hysteresis is shown.

Figure 4-11 shows the hysteresis loop of a single domain stress-free RVE with (dotted blue) and without (solid black) a bias field of 1 MV/m along the [111] direction. The RVE is first initialized in the rhombohedral phase and then an electric field in the [110] direction is cycled twice from 0 MV/m to 10 MV/m to -10 MV/m to 0 MV/m. Without accounting for any sort of bias or fluctuation, after the model transitions from the R to O phase at around 2.1 MV/m, the model stays and switches in the O phase even after the field is released. The model switches between O variants around +/-2.5 MV/m. In contrast to this, the hysteresis loop changes significantly if there is a bias in the [111] direction. As expected, the center of the hysteresis loop becomes offset, However, the model is now able to return to the R phase from O while the electric field is being released. Taking R^+ to be the starting variant, the phases cycles from $R^+ \rightarrow O^+ \rightarrow R^+ \rightarrow R^- \rightarrow O^- \rightarrow R^- \rightarrow R^+$.

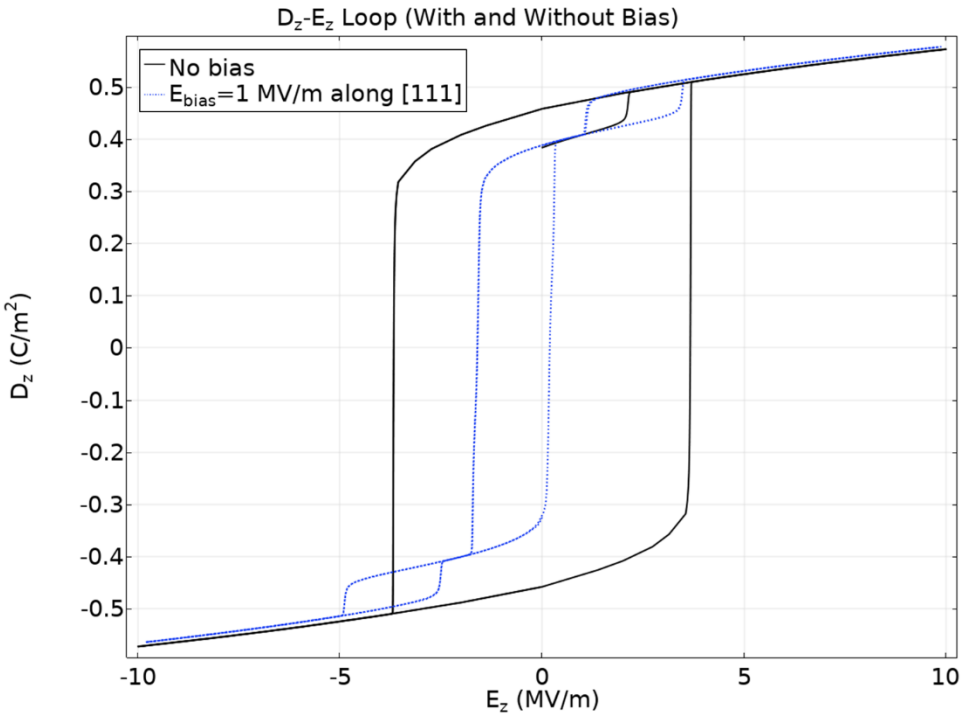

Figure 4-11: D-E hysteresis loop with (dotted blue) and without (solid black) a bias field of 1 MV/m along the [111] direction.

Figure 4-12 shows the D-E hysteresis loop for a bias field along [111] with magnitudes 0.1, 1, and 10 MV/m. The model is initialized in the R phase The case of E_{bias}=0.1 MV/m, is the same as in Figure 4-11. For the case with E_{bias}=0.1 MV/m, the model does not return to the original R variant as, but does transform to the R variant with opposite sign in z. The phases cycle $R^+ \rightarrow O^+ \rightarrow R^- \rightarrow O^- \rightarrow R^+$. For the case with E_{bias}=10 MV/m, the model did not transition to the O phase over the simulated range and cycled from $R \rightarrow T \rightarrow R$ instead due to the strong bias field.

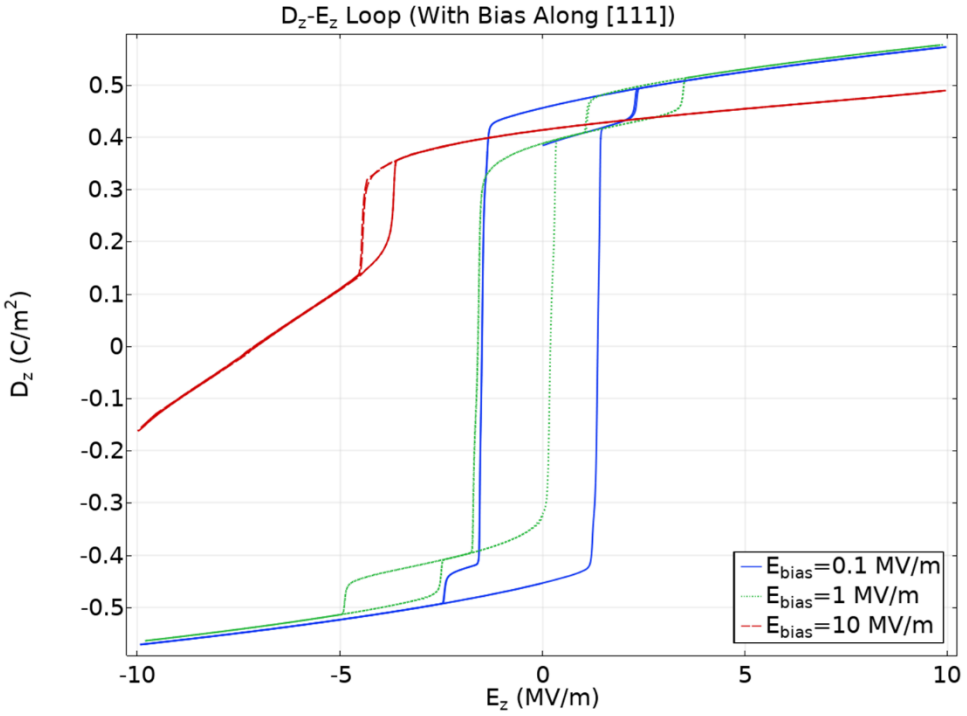

Figure 4-12: D-E hysteresis loop with bias along [111] for E_{bias}=0.1,1, and 10 MV/m (solid blue, dotted green and dashed red respectively).

These simulations show that presence of some bias field allows the model to capture completely different hysteresis behavior.

2. Random Electric Field

a) Relaxor Behavior

The strength of the local electric field is varied to show their effects on relaxor behavior. A 100x100 RVE is modeled with region size of about 10 nm with the variance varying from 0.01 to 50 MV/m. Figure 4-13 shows the distribution for variance of 1 MV/m. Figure 4-14 shows the D-E and e-E hysteresis loops. The electric displacement is averaged over the RVE, while the strain is calculated based on the displacements of the RVE's corners. At low field strengths, the model is unable to escape the metastable wells and largely look similar to the case with no biases present. However, when the local fields are on the order of 1 MV/m, new phase transitions (O to R) appear in the hysteresis loop, but there is still little to no relaxor characteristics appearing in the D-E and e-E loops at this strength. Relaxor characteristics start to appear in the hysteresis loops as the strength of the field is increased further as the variance is increased to 5-10 MV/m. At these strengths, the local field is strong enough for small phases nucleate (similar to polar nanoregions). As an external field is applied, the phase transitions happen locally on the PNR level. In contrast to this, the entire ferroelectric transforms phases uniformly when the field strength is weaker.

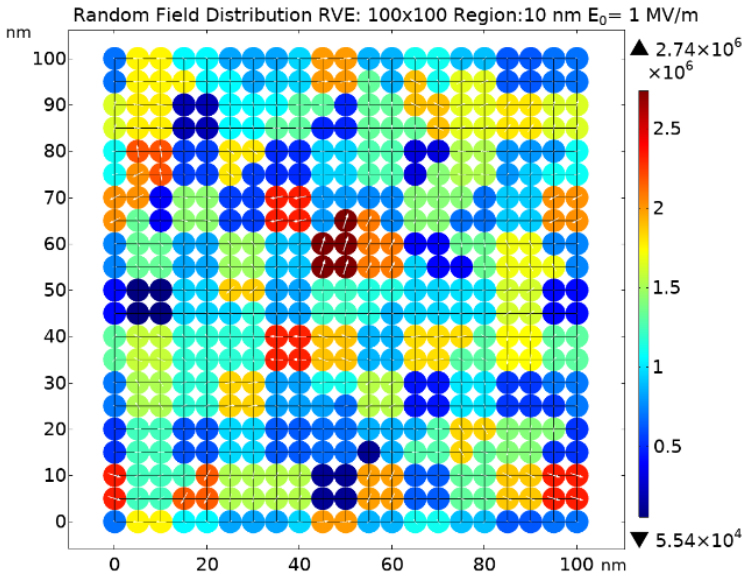

Figure 4-13: Random Field Distribution of 100 nm x100 nm RVE for variance E_0=1MV/m.

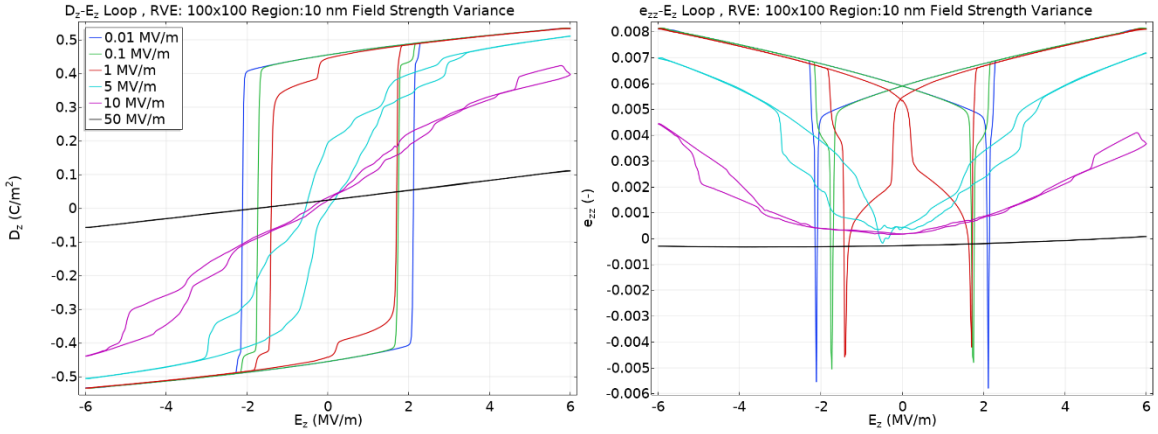

Figure 4-14: D-E and e-E hysteresis loops as the field strength variance is varied from 0.01-5 MV/m.

Figure 4-15 shows the D-E hysteresis loop of a 100 nm x 100 nm RVE for region sizes between 2-20 nm. For each case, the mesh size is half the region size. The electric field is cycled from +6 MV/m to -6 MV/m. Comparing this to Figure 4-14, decreasing the region size seems to have a similar effect as decreasing the field strength. Increasing the region size is similar to

increasing the field strength up until the local random field is strong enough to cause domain pinning or nucleation. Increasing the region size while keeping the same field strength variance does not introduce relaxor characteristics into the model as increasing the field strength did when the region size was kept the same. This is because as the region size of the random field increases, the field will look more uniform across the RVE and cause the RVE to transition simultaneously. For relaxor behavior to appear in the model, the phase transitions need to occur locally and gradually. This suggests there can be a balance in tuning the region size and field strength depending on what hysteresis charactersistics are desired.

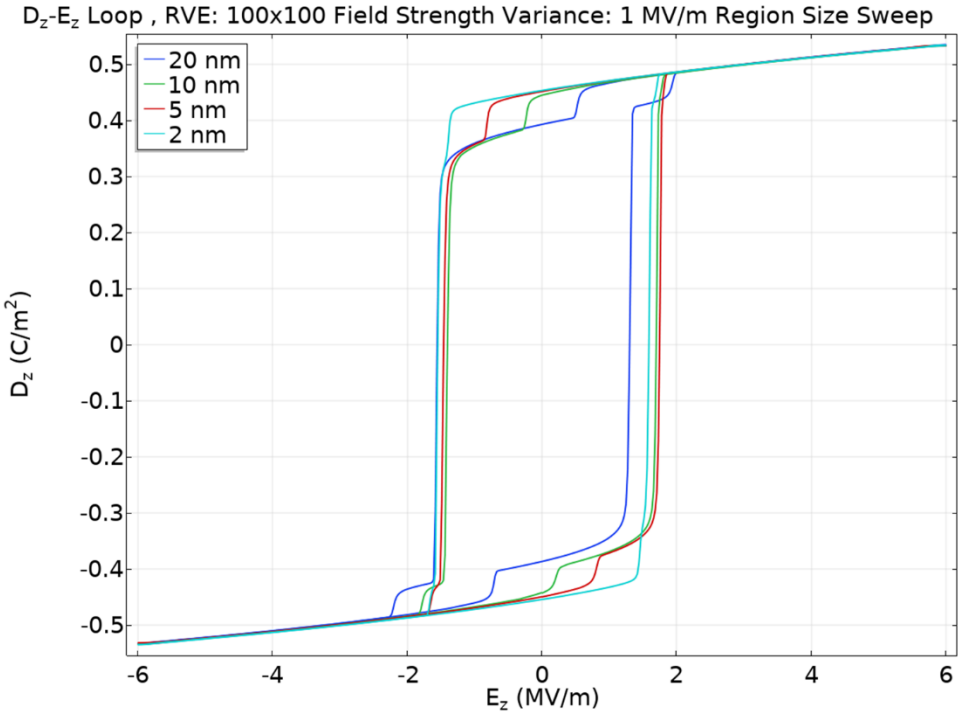

Figure 4-15: D-E hysteresis loops for region sizes of 2-20 nm with electric field variance 1 MV/m.

b) Strain Variation

Figure 4-16 shows the distributions of change in the strain differential between $\varepsilon_{yy} - \varepsilon_{zz}$ as an electric field of 0.72 MV/m is applied alon [110] for the cases of with and without random

fields. The RVE is 100 nm x 100 nm with region size of 10 nm and local field variance of 1 MV/m. In the case of no random fields, the strain distribution is uniform across the RVE. However, if random fields are added, there is now local variation across the RVE on the order of 100 microstrain. This variation is on the same order of magnitude as the strains reported by Lo Conte [37].

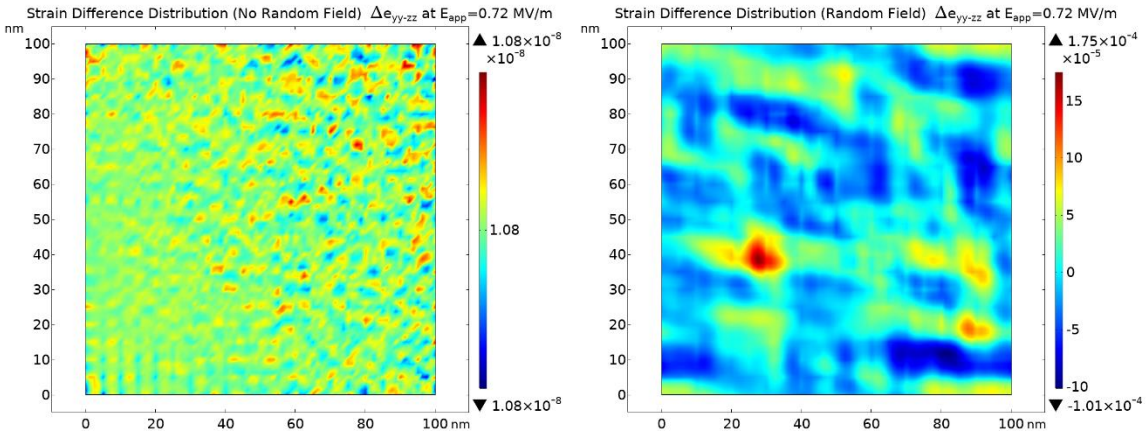

Figure 4-16: Local strain changes as electric is applied. Without accounting for fluctuations or biases, the strain distribution is completely uniform. With a random field, there are local variations on the order of about 100 u.

c) Random Seed Study

For local electric field distributions with random magnitude and directions, the simulated results are dependent on the random seed at initialization. The effect of the random seeds is demonstrated using an RVE of size 10 nm x 10 nm and region size of 2 nm. Figure 4-17 and Figure 4-18 show the electric displacement's evolution in time as an electric field is applied and released initialized with six different random seeds. The phase transformations do not happen simultaneously. Additionally, only some of the random seeds returned to the rhombohedral phase as the electric field was released. Figure 4-18 shows there can be a large spread in at which the R

to O transition happens (from around 1.4 MV/m to 3 MV/m). The boxed R to O transitions show three of the six seeds transitioned around 1.2-1.5 MV/m while loading, while the boxed O to R transition shows that two of the six seeds transitioned around 0.5-0.8 MV/m while unloading.

Although the periodic conditions effectively introduce long-range order, these cases can still provide some insight. Due to the stochastic nature of these fields, it is assumed that a seed configuration describes some local area of the overall material. When some critical field is reached across the material, there will be enough local areas with enough energy to transition and overcome the "inertia" from the rest of the material. In this scenario, the material would transform simultaneously.

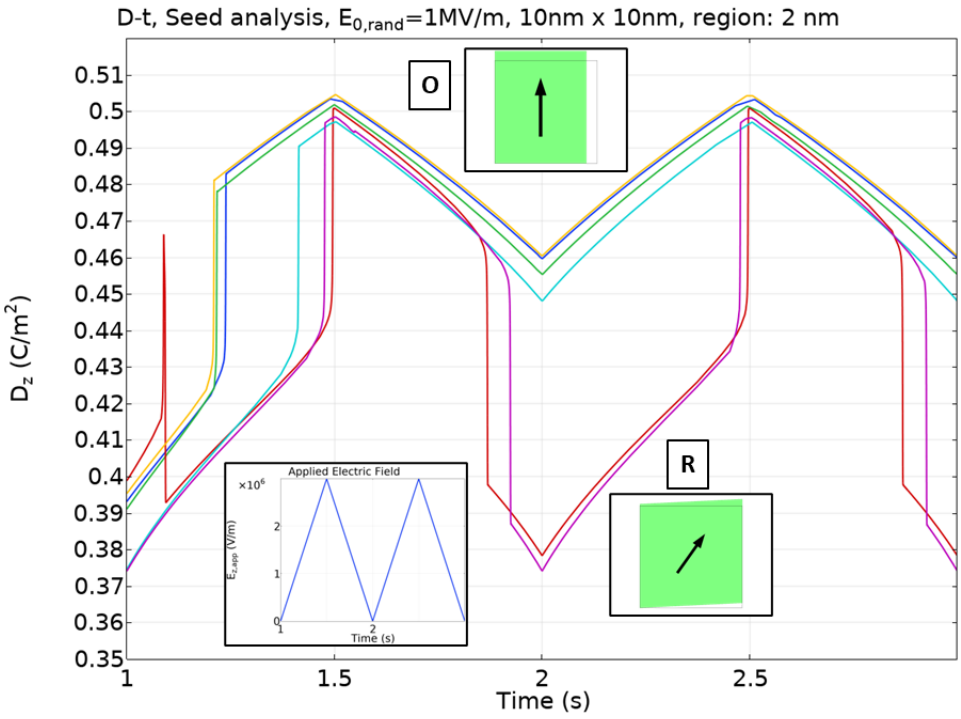

Figure 4-17: D_z-t evolution as electric field applied and released for different random initializations.

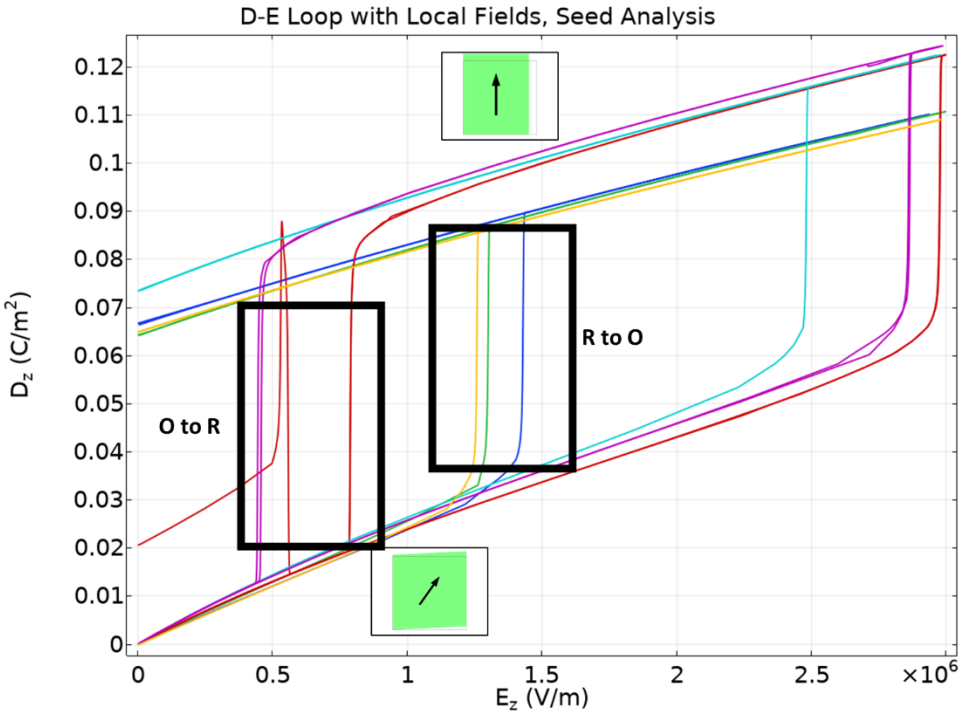

Figure 4-18: ΔD-E Loop with local random fields initialized with different random seeds.

In addition to strain variation within an RVE, there may be variation throughout the material. The difference between the maximum and minimum strains of a 5 nm x 5 nm RVE with and without random fields are plotted below in Figure 4-19 for different initial seeds without an applied field. In the case without random fields, the difference between seeds is effectively zero. In the case with random fields, the plot shows the strain difference within an RVE and between seeds are both on the order of 100 microstrains. This also supports the nonuniform strain field reported by Lo Conte [37].

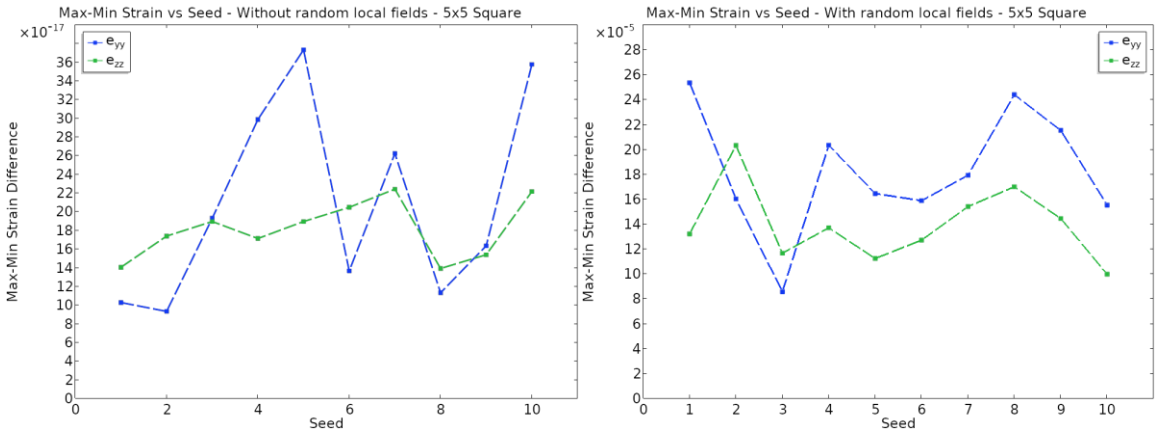

Figure 4-19: Difference between maximum and minimum strains within a 5x5 RVE with and without random local fields for 10 random seeds.

d) Electrically induced phase transformation with preload

Figure 4-20 shows the D-E and D-t history of an RVE with preload and an applied electric field along z [110] for two seeds. Preload is in y [001] and constant within a simulation. Each cycle consists of loading and unloading the electric field from 0 to 3 to 0 MV/m. In general, the hysteresis loops shift towards the left with increasing compressive load. This is consistent with the trends observed experimentally by [24].

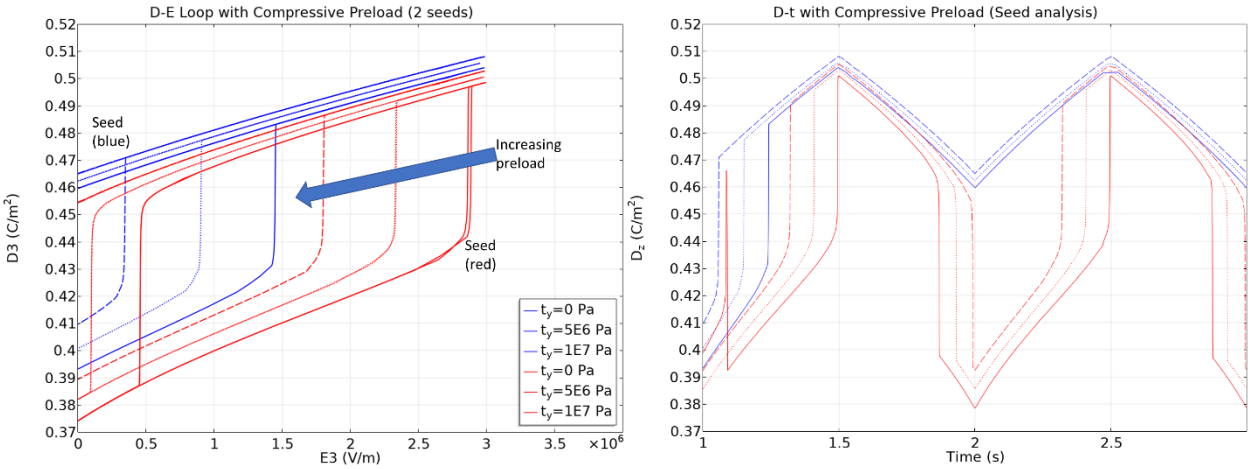

Figure 4-20: D-E phase transition loop with various preloads. Blue and red colors correspond to different random seeds.

3. Stress-induced phase transformation

Figure 4-21 shows the electric displacement evolution in time for a stress-induced phase transformation such as in experiments by Liu et al [25]. The model size is a 200 nm x 200 nm with region size of about 20 nm for the local random field and field variance of 2 MV/m. The stress is gradually loaded and unloaded from 0 to 70 MPa. The model is first poled under a strong electric field in the [110] direction before releasing and allowed to relax. As the load is applied in the [001] direction, the R domains are pressed into the O phase and return to the R domains as the load is released. The model yields similar results when the region size is decreased from 20 nm to 10 nm or from 2 MV/m to 1 MV/m.

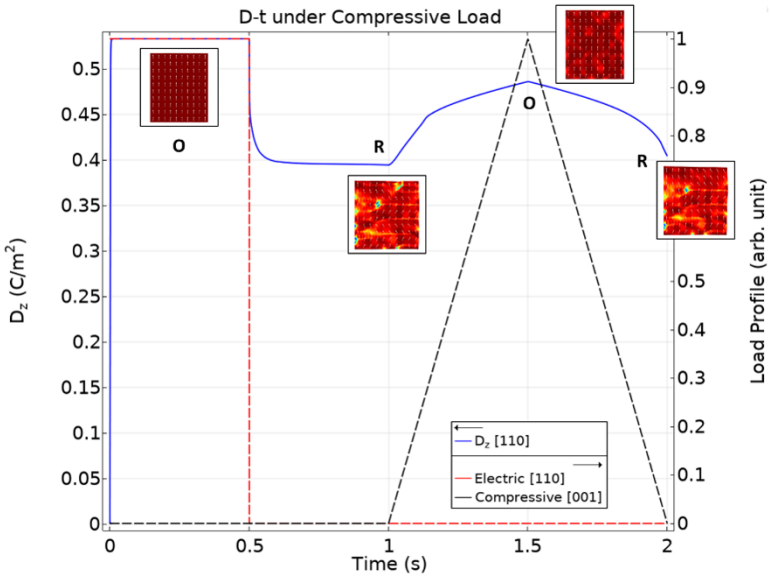

Figure 4-21: Average electric displacement for stress-induced phase transformation.

IV. Conclusion

This chapter investigated the effect of fluctuations and local biases on phase transformations in ferroelectrics were investigated using a phase field model. Chapter 2 concluded that that to model phase transitions in ferroelectric materials, some sort of perturbation is required to escape a metastable or unstable equilibrium.

The fluctuation or local biases were primarily modeled as static local fields. A time-varying noise term to the TDGL equation was also considered and can allow the model to escape a metastable state. However, this implementation is not recommended for modeling phase transitions because the time-varying nature of the noise prevents the model from reaching convergence and makes the transitions inconsistent between cycles.

The transitions observed in this study can be broadly categorized into two cases depending on the strength of the local electric fields. If the local electric fields are relatively weak (i.e. does not nucleate into nanodomains), an RVE of a single crystal will transition phases simultaneously.

However, if the local fields are strong enough for nanoregions or nanodomains to nucleate, the crystal will gradually transition from one phase to another starting from these nucleation zones through domain wall motion. This gradual transition corresponds to the material's relaxor behavior.

Accounting for these physics allowed the model to escape metastable and unstable equilibrium states and show more similar hysteresis behavior to experiments. The predicted coercive switching fields to be more in line with experimental measurements, and various trends and behaviors from experiments reported in literature can now be reproduced using a phase field model. This includes electrically-induced and stress-induced phase transformations, as well as the shift in the hysteresis loop with increasing compressive preload.

V. References

[1] Devonshire, A. F. "XCVI. Theory of Barium Titanate." *The London, Edinburgh, and Dublin Philosophical Magazine and Journal of Science*, Vol. 40, No. 309, 1949, pp. 1040–1063. https://doi.org/10.1080/14786444908561372.

[2] Amin, A., Haun, M. J., Badger, B., Mckinstry, H., and Cross, L. E. "A Phenomenological Gibbs Function for the Single Cell Region of the PbZrO3:PbTiO3 Solid Solution System." *Ferroelectrics*, Vol. 65, No. 1, 1985, pp. 107–130. https://doi.org/10.1080/00150198508008964.

[3] Zhang, H., Lu, X., Wang, R., Wang, C., Zheng, L., Liu, Z., Yang, C., Zhang, R., Yang, B., and Cao, W. "Phase Coexistence and Landau Expansion Parameters for a 0.70Pb(M G1/3 N B2/3) O3-0.30PbTi O3 Single Crystal." *Physical Review B*, Vol. 96, No. 5, 2017, pp. 1–9. https://doi.org/10.1103/PhysRevB.96.054109.

[4] Lv, P., Wang, L., and Lynch, C. S. "A Phenomenological Thermodynamic Energy Function for PIN-PMN-PT Relaxor Ferroelectric Single Crystals." *Acta Materialia*, Vol. 137, 2017, pp. 93–102. https://doi.org/10.1016/j.actamat.2017.07.031.

[5] Chen, L. Q., and Shen, J. "Applications of Semi-Implicit Fourier-Spectral Method to Phase Field Equations." *Computer Physics Communications*, Vol. 108, Nos. 2–3, 1998, pp. 147–158. https://doi.org/10.1016/s0010-4655(97)00115-x.

[6] Schrade, D., Mueller, R., Xu, B. X., and Gross, D. "Domain Evolution in Ferroelectric Materials: A Continuum Phase Field Model and Finite Element Implementation." *Computer Methods in Applied Mechanics and Engineering*, Vol. 196, Nos. 41–44, 2007, pp. 4365–4374. https://doi.org/10.1016/j.cma.2007.05.010.

[7] Su, Y., and Landis, C. M. "Continuum Thermodynamics of Ferroelectric Domain Evolution :

Theory, Finite Element Implementation, and Application to Domain Wall Pinning." *Journal of the Mechanics and Physics of Solids*, Vol. 55, 2007, pp. 280–305. https://doi.org/10.1016/j.jmps.2006.07.006.

[8] Hu, H. L., and Chen, L. Q. "Computer Simulation of 90° Ferroelectric Domain Formation in Two-Dimensions." *Materials Science and Engineering A*, Vol. 238, No. 1, 1997, pp. 182–191. https://doi.org/10.1016/S0921-5093(97)00453-X.

[9] Hu, H.-L., and Chen, L.-Q. "Three-Dimensional Computer Simulation of Ferroelectric Domain Formation." *Journal of American Ceramic Society*, Vol. 81, 1998, pp. 492–500. https://doi.org/10.1111/j.1151-2916.1998.tb02367.x.

[10] Choudhury, S., Li, Y. L., Krill, C. E., and Chen, L. Q. "Phase-Field Simulation of Polarization Switching and Domain Evolution in Ferroelectric Polycrystals." *Acta Materialia*, Vol. 53, No. 20, 2005, pp. 5313–5321. https://doi.org/10.1016/j.actamat.2005.07.040.

[11] Zhang, W., and Bhattacharya, K. "A Computational Model of Ferroelectric Domains. Part I: Model Formulation and Domain Switching." *Acta Materialia*, Vol. 53, No. 1, 2005, pp. 185–198. https://doi.org/10.1016/j.actamat.2004.09.016.

[12] Song, Y. C., Soh, A. K., and Ni, Y. "Phase Field Simulation of Crack Tip Domain Switching in Ferroelectrics." *Journal of Physics D: Applied Physics*, Vol. 40, No. 4, 2007, pp. 1175–1182. https://doi.org/10.1088/0022-3727/40/4/040.

[13] Wang, D., Wang, L., and Melnik, R. "Vibration Energy Harvesting Based on Stress-Induced Polarization Switching: A Phase Field Approach." *Smart Materials and Structures*, Vol. 26, No. 6, 2017. https://doi.org/10.1088/1361-665X/aa6e46.

[14] Indergand, R., Vidyasagar, A., Nadkarni, N., and Kochmann, D. M. "A Phase-Field

Approach to Studying the Temperature-Dependent Ferroelectric Response of Bulk Polycrystalline PZT." *Journal of the Mechanics and Physics of Solids*, Vol. 144, 2020. https://doi.org/10.1016/j.jmps.2020.104098.

[15] Kingsland, M., Fthenakis, Z. G., and Ponomareva, I. "Role of Depolarization in the Polarization Reversal in Ferroelectrics." *Physical Review B*, Vol. 100, No. 2, 2019, p. 24114. https://doi.org/10.1103/PhysRevB.100.024114.

[16] Cohen, R. E. "Relaxors Go Critical." *Nature*, No. 441, 2006, pp. 941–942. https://doi.org/https://doi.org/10.1038/441941a.

[17] Kleemann, W. "RANDOM FIELDS IN RELAXOR FERROELECTRICS — A JUBILEE REVIEW." Vol. 2, No. 2, 2012, pp. 1–13. https://doi.org/10.1142/S2010135X12410019.

[18] Pramanick, A., and Nayak, S. "Perspective on Emerging Views on Microscopic Origin of Relaxor Behavior." *Journal of Materials Research*, Vol. 36, No. 5, 2021, pp. 1015–1036. https://doi.org/10.1557/s43578-020-00010-7.

[19] Li, F., Zhang, S., Yang, T., Xu, Z., Zhang, N., Liu, G., Wang, J., Wang, J., Cheng, Z., Ye, Z., Luo, J., Shrout, T. R., and Chen, L. "The Origin of Ultrahigh Piezoelectricity in Relaxor-Ferroelectric Solid Solution Crystals." *Nature Communications*, Vol. 7, 2016, pp. 1–9. https://doi.org/10.1038/ncomms13807.

[20] Li, F., Lin, D., Chen, Z., Cheng, Z., Wang, J., Li, C., Xu, Z., Huang, Q., Liao, X., Chen, L. Q., Shrout, T. R., and Zhang, S. "Ultrahigh Piezoelectricity in Ferroelectric Ceramics by Design." *Nature Materials*, Vol. 17, No. 4, 2018, pp. 349–354. https://doi.org/10.1038/s41563-018-0034-4.

[21] Takenaka, H., Grinberg, I., and Rappe, A. M. "Anisotropic Local Correlations and Dynamics in a Relaxor Ferroelectric." *Physical Review Letters*, Vol. 110, No. 14, 2013.

https://doi.org/10.1103/PhysRevLett.110.147602.

[22] Takenaka, H., Grinberg, I., Liu, S., and Rappe, A. M. “Slush-like Polar Structures in Single-Crystal Relaxors.” *Nature*, Vol. 546, No. 7658, 2017, pp. 391–395. https://doi.org/10.1038/nature22068.

[23] Wang, S., Yi, M., and Xu, B. X. “A Phase-Field Model of Relaxor Ferroelectrics Based on Random Field Theory.” *International Journal of Solids and Structures*, Vol. 83, 2016, pp. 142–153. https://doi.org/10.1016/j.ijsolstr.2016.01.007.

[24] Gallagher, J. A., Tian, J., and Lynch, C. S. “Composition Dependence of Field Induced Phase Transformations in [0 1 1]C PIN-PMN-PT Relaxor Ferroelectric Single Crystals with D322 Piezoelectric Mode.” *Acta Materialia*, Vol. 81, 2014, pp. 512–523. https://doi.org/10.1016/j.actamat.2014.06.062.

[25] Liu, Y., Xia, J., Finkel, P., Moss, S. D., Liao, X., and Cairney, J. M. “Real-Time Observation of Stress-Induced Domain Evolution in a [011] PIN-PMN-PT Relaxor Ferroelectric Single Crystal.” *Acta Materialia*, Vol. 175, 2019, pp. 436–444. https://doi.org/10.1016/j.actamat.2019.06.023.

[26] Lv, P., and Lynch, C. S. “Phase-Field Simulation of Domain Walls in Rhombohedral Ferroelectric Single Crystals.” *Acta Materialia*, Vol. 155, 2018, pp. 245–252. https://doi.org/10.1016/j.actamat.2018.06.016.

[27] Gurtin, M. E. “Generalized Cahn-Hilliard Equations Based on a Microforce Balance.” *Physica D: Nonlinear Phenomena*, Vol. 92, Nos. 3–4, 1996, pp. 178–192. https://doi.org/https://doi.org/10.1016/0167-2789(95)00173-5.

[28] Carka, D., and Lynch, C. S. *Ferroelectric and Ferromagnetic Phase Field Modeling*.

[29] Smit, R. J. M., Brekelmans, W. A. M., and Meijer, H. E. H. “Prediction of the Mechanical

Behavior of Nonlinear Heterogeneous Systems by Multi-Level Finite Element Modeling." *Computer Methods in Applied Mechanics and Engineering*, Vol. 155, Nos. 1–2, 1998, pp. 181–192. https://doi.org/10.1016/S0045-7825(97)00139-4.

[30] Funaki, T. "The Scaling Limit for a Stochastic PDE and the Separation of Phases." *Probability Theory and Related Fields*, Vol. 102, No. 2, 1995, pp. 221–288. https://doi.org/10.1007/BF01213390.

[31] Shardlow, T. "Stochastic Perturbations of the Allen-Cah Equation." *Electronic Journal of Differential Equations*, Vol. 2000, No. 47, 2000, pp. 1–19.

[32] Rolland, J., Bouchet, F., and Simonnet, E. "Computing Transition Rates for the 1-D Stochastic Ginzburg–Landau–Allen–Cahn Equation for Finite-Amplitude Noise with a Rare Event Algorithm." *Journal of Statistical Physics*, Vol. 162, No. 2, 2016, pp. 277–311. https://doi.org/10.1007/s10955-015-1417-4.

[33] Koyama, T. "Phase-Field Modeling of Microstructure Evolutions in Magnetic Materials." *Science and Technology of Advanced Materials*, Vol. 9, No. 1, 2008. https://doi.org/10.1088/1468-6996/9/1/013006.

[34] Baruffi, C., Finel, A., Le Bouar, Y., Bacroix, B., and Salman, O. U. "Overdamped Langevin Dynamics Simulations of Grain Boundary Motion." *Materials Theory*, Vol. 3, No. 1, 2019, pp. 1–26. https://doi.org/10.1186/s41313-019-0016-1.

[35] Rodriguez, B. J., Jesse, S., Bokov, A. A., Ye, Z. G., and Kalinin, S. V. "Mapping Bias-Induced Phase Stability and Random Fields in Relaxor Ferroelectrics." *Applied Physics Letters*, Vol. 95, No. 9, 2009, pp. 15–18. https://doi.org/10.1063/1.3222868.

[36] Box, G. E. P., and Muller, M. E. "A Note on the Generation of Random Normal Deviates." *The Annals of Mathematical Statistics*, Vol. 29, No. 2, 1958, pp. 610–611.

https://doi.org/https://doi.org/10.1214/aoms/1177706645.

[37] Lo Conte, R., Xiao, Z., Chen, C., Stan, C. V., Gorchon, J., El-Ghazaly, A., Nowakowski, M. E., Sohn, H., Pattabi, A., Scholl, A., Tamura, N., Sepulveda, A., Carman, G. P., Candler, R. N., and Bokor, J. "Influence of Nonuniform Micron-Scale Strain Distributions on the Electrical Reorientation of Magnetic Microstructures in a Composite Multiferroic Heterostructure." *Nano Letters*, Vol. 18, No. 3, 2018, pp. 1952–1961. https://doi.org/10.1021/acs.nanolett.7b05342.

Chapter 5: Modeling Novel Synthetic Jet Actuators

I. Introduction

A synthetic jet actuator (SJA) is a device that blows puffs of air through a small orifice into the boundary layer of a flow field. This alters the flow and can reduce drag. SJAs have three main components whose functions are coupled through fluid motion: 1) a cavity, 2) an orifice, and 3) an oscillating diaphragm. Air is suctioned into and expelled from the cavity through the orifice as the diaphragm oscillates. SJAs (also called zero-net mass flux jet actuators) are named for their ability to synthesize jet flow using fluid from the surrounding environment, eliminating the need to provide a fluid source and the necessary piping to create the jet. SJAs have potential commercial applications in both the automotive and aerospace industries if they can achieve high enough jet velocities to be effective while meeting constraints on power consumption and geometry. Additionally, SJAs have also found applications in areas including active-flow control [1–3], mixing [4,5] and heat transfer/cooling [6,7]. As applications are being developed, models that can be used to explore wide design spaces are needed to help optimize their design and performance.

SJA models do exist, but typically require fitting at least two parameters that directly affect the amplitude and shape of the predicted response: 1) the diaphragm's deformation (through the force or electroacoustic transduction of the diaphragm) and 2) the loss coefficient *K*. Reliance on these fitting parameters significantly limits their ability to quickly explore new designs.

Furthermore, many SJA models directly use a Helmholtz resonance assumption, which casts doubt on their ability to model cavities that deviate from the Helmholtz idealization. Van Buren's experiments [8,9] on flat and thin "pancake-shaped" SJAs showed velocities as high as $211\ m/s$ and momentum $0.654\ kg \cdot m/s$. Because of this, these pancake-shaped cavities are of great interest due to the potential of reaching extremely high velocities and momentum relative to

previous designs. However, the Helmholtz frequency can overpredict the cavity resonances by more than 130% depending on the geometry [10]. Figure 5-22 shows examples of an ideal Helmholtz resonator (characterized by a large cavity and small orifice) and the non-Helmholtz "pancake"-shaped resonator used as a synthetic jet actuator that is addressed in the dissertation.

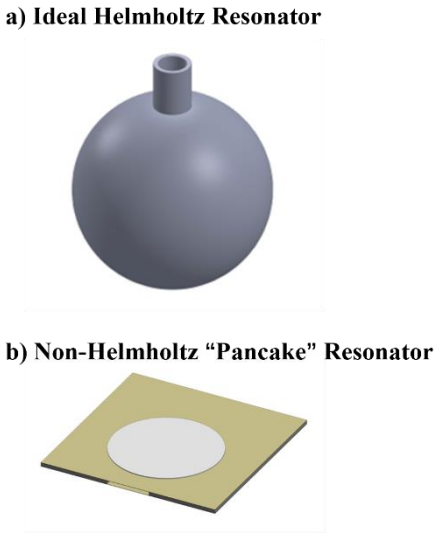

Figure 5-22: Example of a) an ideal Helmholtz and b) a non-Helmholtz "pancake"-shaped resonator.

One of the goals was to develop SJA modeling tools capable of exploring novel geometric and material configurations, including "pancake"-shape cavities with large orifices. Lumped-element models reported in literature largely follow the Helmholtz resonator idealization which limits the model to geometries with large cavities and small orifices. Full-ordered models (full multiphysics finite element models), while capable of modeling a broad range of designs, can be prohibitively computationally expensive. A middle ground between LEMs and full-ordered models was needed.

This chapter first explores the history of SJAs, traditional SJA LEM models, and the current challenges to modeling novel designs. It is followed by a description of three models: an

electromechanics FEM diaphragm model, a pressure acoustics FEM cavity model, and a hybrid finite-element/lumped-element model that couples the diaphragm model with LEM-based equations. The FEM cavity-orifice acoustics model provides a characteristic resonance used in place of the Helmholtz resonance for the LEM equations. The use of finite elements to model the diaphragm physics reduces the need for the fitting parameters used by some previous models. The hybrid model is compared to and validated by experimental measurements conducted by Actasys. This is followed by further discussion of the cavity resonance.

II. History and Background

Synthetic jets were observed by Ingard & Labate in 1950 using acoustically driven standing waves in a cylindrical tube as they studied the acoustical streaming phenomena around the orifice [11]. Smith & Glezer [12] later demonstrated the utility of synthetic jets for flow control, leading to a substantial body of research into using SJAs to enhance lift and/or reduce drag.

Lumped-element models (LEMs) have been developed that fall into two categories: 1) circuit-analogy based [13–15] and 2) fluid-dynamics based [16–18]. In the circuit-analogy based, an equivalent electrical circuit is found for each component (cavity, orifice, diaphragm) of the SJA, while the fluid-dynamics based LEMs directly apply the continuity and Bernoulli equations. One of the first LEMs developed for SJAs was McCormick's [15] electroacoustic model for an acoustically driven SJA that was able to relate a voltage input with a velocity output. Expanding on this, Gallas et al. [13] developed a model for a piezoelectrically-driven SJA, and borrowed Prasad et al.'s [19] LEM work on axisymmetric piezoelectric composite plates. Sharma [16] developed an alternative to the circuit-based models to additionally model the cavity pressure fluctuations and the phase relationships between the different variables using a fluid-dynamics approach. Using Sharma's work as its basis, de Luca et al. [17] worked to better characterize the

SJA's frequency response and developed simple relationships to predict deviation of the coupled peaks from the component Helmholtz and diaphragm resonances. Works by de Luca and Chiatto [20–22] have sought to better understand the effects nonlinear losses have on the resonance.

Sharma's work [16] defined the loss coefficient as the sum of the geometric head losses and the inverse contraction ratio between the vena contracta A_{vc} and the orifice exit A_o areas. However, this definition of K results in a value greater than 1 for all resonators, and close to 1.42 for ideal Helmholtz resonators. Sharma's own work suggested loss coefficients ranging between 0.42 and 1.0, and models reported in literature [13,16,17] have used values ranging between from 0.78 to 1.14.

With proper fitting, these models can obtain good agreement with experimental results, however this agreement is still largely limited to ideal Helmholtz resonator geometries. Housley et al. [18] developed a model for SJAs with circular piezoelectrical bimorphs and experimented with various cavity heights. While Housley's model was successful at predicting performance for SJAs with larger cavity heights, the model was unable to capture the performance for SJAs with smaller cavity heights, which Housley attributed to increased acoustic coupling.

Van Buren [10] studied the resonant frequencies of pancake-shaped SJAs and found the Helmholtz resonance idealization to be a poor predictor of the actual resonance frequency and suggested the quarter-wave resonance may be more appropriate for pancake-shaped cavities. Van Buren concluded that current LEMs are unable to accurately predict the performance of SJAs with that geometry.

Predicting the resonance frequency of a SJA is a critical part of the design and determining its operating frequency. The Helmholtz resonator idealization identifies the resonance frequency from the cavity volume and orifice size. The Helmholtz resonator is often represented by a spring-

mass system where the mass of air in the orifice oscillates against the stiffness of the cavity. End corrections to the orifice length are used to account for the additional mass of air that oscillates outside the orifice and depend on whether the pipe is flanged or not [23]. There have been many works dedicated to improve characterization of the Helmholtz frequency [10,24–29]. Alster [24] developed an extended theory to better account for the air vibrating inside the cavity and linked the quarter-wave and Helmholtz resonances to the same the underlying physics. More recently, Gil [29] investigated the impact that changing various geometric parameters has on the Helmholtz Resonance frequency in an SJA.

III. Cavity Resonances

The cavity-orifice acoustics play a significant role in determining the performance and operating range of an SJA. Past models have typically used a Helmholtz idealization, though the quarter-wave idealization has also been suggested for certain geometries [10]. Both idealizations are summarized and then followed by a description of Alster's expanded theory to the classical Helmholtz frequency formula.

A. Helmholtz Resonator

The Helmholtz frequency appears as the characteristic frequency of a resonator after combining the continuity and Bernoulli equations when several key assumptions are made: 1) having a large cavity and small orifice, and 2) that all dimensions of the resonator are much smaller than the wavelength of the oscillations ($L_{any} \ll \lambda$). Geometries that deviate from these assumptions will have a different characteristic frequency. The FEM pressure-acoustics model of the cavity-orifice was used to calculate the characteristic frequency for these geometries.

An ideal Helmholtz resonator consists of a large spherical cavity with a small neck and orifice. The system can also be represented using a spring-mass analog where the mass is the air oscillating at the orifice and the spring is the resistance/stiffness of the air in the cavity.

$$\omega_h = \sqrt{\frac{k_a}{m_a}} \tag{5-1}$$

The mass of the air m_a in the orifice is the product of the density of air ρ_a and the orifice volume V_o:

$$m_a = \rho_a V_o = \rho_a A_o l_e \tag{5-2}$$

where A_o is the orifice cross-sectional area and l_e is the effective orifice neck length.

An end correction Δl to the nominal neck length l_n is commonly used to reconcile the difference between the theoretical and observed resonance frequencies for resonators including the Helmholtz resonators. This accounts for an additional mass of air oscillating outside the orifice. The effective neck length l_e can be expressed as

$$l_e = l_n + \Delta l \tag{5-3}$$

where Δl depends on the pipe's cross-section.

For example, the end correction at the open end of an unflanged pipe was theoretically calculated by Levine & Schwinger to be 0.6133 of the radius $\Delta l = 0.6133$. For more complex geometries where this correction is not sufficiently accurate, the end correction is typically determined through experimentation.

The stiffness of the air k_a in the cavity can be obtained using Hooke's law:

$$k_a = -\frac{dF}{dx} = -\frac{A_o dP}{dx}\frac{A_o}{A_o} = -A_o^2 \frac{dP}{dV} \tag{5-4}$$

where dF is the force acting on the air caused by a pressure differential dP across the orifice.

Assuming an isentropic process, $\frac{dP}{dV}$ can be found by taking the derivative of the following relation:

$$PV^{\gamma} = constant \tag{5-5}$$

$$V^{\gamma}dP + \gamma PV^{\gamma-1}dV = 0 \tag{5-6}$$

where P is pressure, V is volume, and γ is the specific heat ratio.

For small changes in pressure and volume,

$$\frac{dP}{dV} = -\frac{\gamma P}{V} \approx -\frac{\gamma P_0}{V_c} \tag{5-7}$$

where P_0 is the ambient pressure and V_c is the cavity volume.

Using Equation 5-7, the stiffness in Equation 5-4 becomes

$$k_a = \frac{\gamma A_o^2 P_0}{V_c} \tag{5-8}$$

Combining Equations 5-2 and 5-8 with Equation 5-1, the formula for the Helmholtz resonance frequency becomes:

$$\omega_H = \sqrt{\frac{k_a}{m_a}} = \sqrt{\frac{\gamma A_o^2 P_0/V_c}{\rho_a A_o l_e}} = \sqrt{\frac{\gamma P_0}{\rho_a}}\sqrt{\frac{A_o}{l_e V_c}} = U_s\sqrt{\frac{A_o}{l_e V_c}} = 2\pi f_H \tag{5-9}$$

where $U_s = \sqrt{\frac{\gamma P_0}{\rho_a}}$ is the speed of sound in air.

B. Quarter-wave Resonator

A quarter-wave resonator is a pipe which is closed on one end and open on the other. The conditions for standing waves in this pipe require there to be a node at the closed end and an anti-

node (maximum) at the open end. With these constraints, the length of the pipe is a quarter of the wavelength at the fundamental frequency.

$$L_{total} = \frac{1}{4}\lambda_{QW} \tag{5-10}$$

The formula for the quarter-wave resonance frequency is:

$$f_{QW} = \frac{\nu_{QW}}{\lambda_{QW}} = \frac{U_s}{4L_{total}}$$

$$\omega_{QW} = 2\pi f_{QW} \tag{5-11}$$

where L_{total} is the total length of the quarter-wave resonator accounting for any end correction.

IV. Methodology

This section will first describe the experimental work conducted by Actasys that will be used to develop and validate the model. Then, several models developed as part of this work are presented and discussed.

A. Experimental Work

Actasys provided the frequency response for several SJA configurations with flat cavities and large orifices. The SJAs consisted of two piezoelectrically-driven diaphragms. The diaphragms were bound to the sides of a cavity/orifice plate. Each diaphragm was a bimorph consisting of a substrate G10/FR4 glass epoxy composite actuated by two CTS 3195HD PZT-5A disks, one centered on each side. A sinusoidal waveform with average voltage $V_{RMS} = 120$ V was used such that the two bimorphs would work to expand and contract the cavity in unison. The data collected included the flow velocity, at the orifice exit, measured using hotwire anemometry and the displacement at the center of the diaphragm measured using a laser vibrometer.

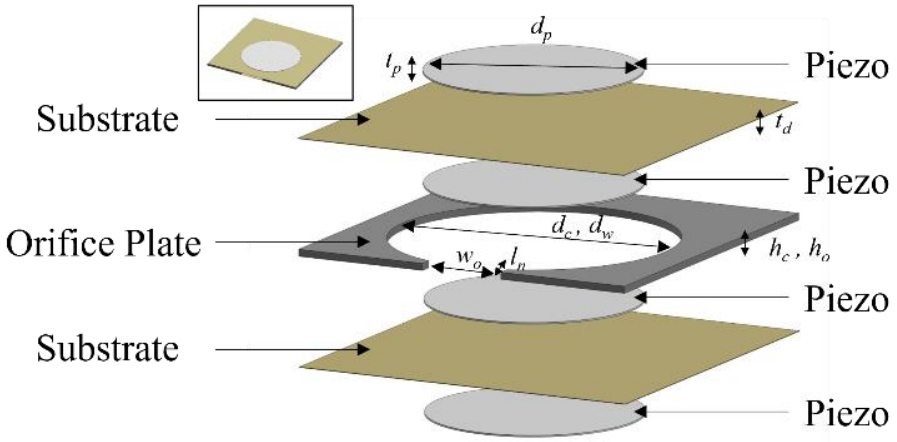

Figure 5-23: Exploded view of SJA with parts and geometric parameters labelled.

Data was provided for the configurations described by Table 5-1-Table 5-4. See Figure 5-23 for an exploded view of the SJA with the described parameters and parts labelled. The configurations included two cavity diameters: $d_c = 80$ mm (described here as Cavity A) and $d_c = 94$ mm (Cavity B). The orifice neck length $l_n = 0.4$ mm, piezoelectric disk diameter $d_p = 64$ mm, piezoelectric disk thickness $t_p = 0.5$ mm, and substrate thickness $t_w = 0.4$ mm were not varied between configurations. The cavity height h_C and orifice width w_o were varied. The orifice had the same height as the cavity ($h_o = h_c$), and the substrate had the same diameter as the cavity $d_w = d_c$. The nominal geometric parameters for h_c and w_o are given in Table 5-1 and Table 5-2. All dimensions are in mm. Data was collected at 10 Hz increments for frequencies between 100-1200 Hz for Cavity A and 10-500 Hz for Cavity B.

Table 5-1: Cavity A.1-A.5 Geometries (d_c=80 mm)

A - Cavity Diameter 80 mm					
Parameter	**A.1**	**A.2**	**A.3**	**A.4**	**A.5**
h_o, h_c	2.37	3.43	2.41	2.4	1.41
w_o	18	18	24	6	18

Table 5-2: Cavity B.1-B.5 Geometries

B - Cavity Diameter 94 mm					
Parameter	**B.1**	**B.2**	**B.3**	**B.4**	**B.5**
h_o, h_c	2.2	3.2	1.7	3.2	3.2
w_o	18	18	18	24	12

The nominal material parameters of the piezoelectric disk are summarized in Table 5-3. The properties are taken from the material data sheet for CTS 3195HD (PZT-5A).

Table 5-3: Piezoelectric Disk Material Properties

Piezoelectric		
ρ_p	7.95	g/cm^3
S_{11}	1.51E-11	1/Pa
S_{12}	-4.80E-12	1/Pa
S_{13}	-7.60E-12	1/Pa
S_{33}	1.51E-11	1/Pa
S_{44}	4.00E-11	1/Pa
d_{31}	-1.71E-10	C/N
d_{33}	3.74E-10	C/N
d_{15}	5.84E-10	C/N
k_1	1600	-
k_3	1900	-
$\tan\delta$	0.02	-

where ρ is the density, S_{ij} are components of the compliance matrix using Voigt notation, d_{ij} are the piezoelectric coefficients, k_{ii} are the relative dielectric permittivity coefficients, and $\tan\delta$ is the loss tangent. The loss tangent $\tan\delta$ is a measure of the energy lost as heat in a dielectric material and modifies the permittivity to $k'_{ii} = k_{ii}(1 - j\tan\delta)$. The compliance matrix $[S_{ij}]$ is the inverse of the stiffness matrix $[C_{ij}]$. The subscripts 1, 2, and 3 indicate principal direction coupling, and subscripts 4, 5, and 6 indicate shear direction coupling. Couplings between directions not listed are either zero or identical to another parameter above.

The substrate was a weaved G10/FR-4 composite and modeled as an isotropic material with the material properties listed in Table 5-4. This model does not account for the effects of the epoxy used to bind the substrate and piezoelectric disks together.

Table 5-4: Substrate Material Properties

	Substrate	
ρ_w	1.97	g/cm^3
E_w	20	GPa
ν	0.127	-

where $E_w$is the elastic modulus, and ν is Poisson's ratio.

B. Uncoupled Models

The overall SJA frequency response is a combination of the cavity's acoustic and diaphragm's mechanical frequency responses. If the two resonances are sufficiently far apart, the system could be considered uncoupled, and the overall response would closely follow the superposition of the two. Otherwise, the system behaves as a coupled oscillators system. The overall response is not simply a superposition of the component responses, and the location of the peaks in the overall response may also shift due to the coupling.

While a coupled model would be necessary to accurately predict the amplitude of outputs such as the jet velocity, uncoupled models can still be useful to predict the approximate locations of the peaks. Assuming an absence of damping effects, de Luca et al. [17] provided a relationship to predict the shifted peaks based on the Helmholtz resonance ω_H, diaphragm's structural resonance ω_w, and the resonance of the pneumatic spring ω_{wp} of the diaphragm and assuming a closed cavity.

$$\omega_{1,2}^2 = \frac{-\left(\omega_w^2 + \omega_{wp}^2 + \omega_H^2\right) \pm \sqrt{\left(\omega_w^2 + \omega_{wp}^2 + \omega_H^2\right)^2 - 4\omega_w^2\omega_H^2}}{2} \tag{5-12}$$

Where ω_{wp} is a function of the diaphragm area A_w and mass m_w:

$$\omega_{wp} = \sqrt{\frac{k_{wp}}{m_w}} = \sqrt{\frac{\gamma A_w^2 P_0 / V_c}{m_w}} \tag{5-13}$$

Equation 5-13 was modified to account for the two diaphragms.

$$\omega_{wp} \approx \sqrt{\frac{\frac{\gamma A_w P_0}{V_c}}{m_w}} \tag{5-14}$$

Conveniently, the formula has the same form after accounting that the actual volume deformation peaks are closer to $\frac{1}{2} A_w \Delta w_{amp}$ at the resonance peaks instead of the assumption $\Delta V \approx A_w \Delta w$, where w is center displacement of the diaphragm.

The resulting coupled natural frequencies are based on the imaginary component of $\omega_{1,2}$

$$f_{1,2} = \frac{\omega_{1,2}^i}{2\pi} \tag{5-15}$$

de Luca et al. [17] defined a coupling ratio CR based on the ratio of the pneumatic spring and diaphragm resonances:

$$CR = \left(\frac{\omega_{wp}}{\omega_w}\right)^2 \tag{5-16}$$

If $CR = 0,$ the diaphragm and cavity acoustic resonances are completely decoupled, and $\omega_{1,2}$ will return ω_H and ω_w. Generally, de Luca observed that the coupling ratio increased as the cavity size decreased, and that increased coupling caused the peaks to shift further away from the center.

1. Electromechanical Diaphragm Model

The diaphragm's displacement w and overall volume displacement ΔV are calculated through the finite element method (FEM) using COMSOL Multiphysics® simulation software. The solid mechanics, electrostatics, and piezoelectric modules in COMSOL were used to model the piezoelectric bimorph diaphragm, solving for the displacements and electric potential. The

diaphragm consisted of a substrate layer and a piezoelectric disk on each side. The diaphragm was modeled as axisymmetric in 2D as shown in Figure 5-24 to reduce the computational costs of the model. 2D axisymmetric models yield identical results as a 3D model when the problem is axisymmetric. Although there is a section of the circumference that is not bound by the cavity plate, this effect on the diaphragm's overall deformation is assumed to be small. A 3D diaphragm model can easily be substituted in place of the 2D axisymmetric model to analyze non-axisymmetric configurations such as noncircular electrodes or diaphragms, disk offsets, etc.

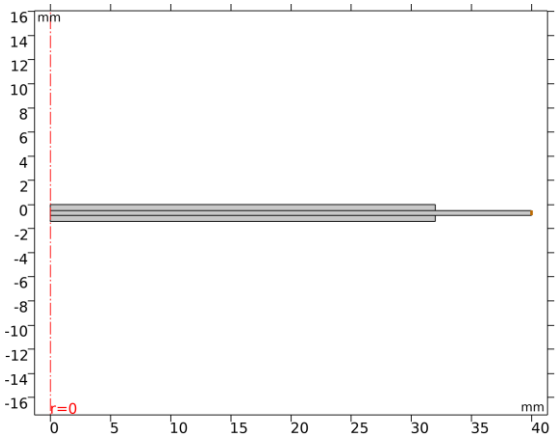

Figure 5-24: Geometry of the SJA diaphragm in the FEM model.

The solid mechanics module solves the equilibrium equation, the linear stress-strain constitutive law, and assumes small strain.

$$\sigma_{ij,j} + b_i = \rho a_i \tag{5-17}$$

$$\sigma_{ij} = C_{ijkl}\epsilon_{kl} \tag{5-18}$$

$$\epsilon_{ij} = \frac{1}{2}\left(u_{i,j} + u_{j,i}\right) \tag{5-19}$$

where σ is stress, b is body force, ρ is density, a is acceleration, C is stiffness, ϵ is strain, and u is displacement.

The electrostatic module solves the differential form of Gauss's law, a linear electric displacement-electric field constitutive law, and the definition of electric field in terms of an electric potential.

$$D_{i,i} = \rho_v \tag{5-20}$$

$$D_i = \epsilon = k_0 k_{ij}^r E_i \tag{5-21}$$

$$E_i = -\phi_{,i} \tag{5-22}$$

where D is the electric displacement, k_0 is the permittivity of free space, k_{ij}^r is the relative permittivity, E_i is the electric field, and ϕ is the electric potential.

In the piezoelectric disks, the solid mechanics and electrostatics are coupled through the piezoelectric strain-charge constitutive relationship:

$$\boldsymbol{\epsilon} = \boldsymbol{s_E \sigma} + \boldsymbol{d^T E} \tag{5-23}$$

$$\boldsymbol{D} = \boldsymbol{d\sigma} + k_0 \boldsymbol{k^r E} \tag{5-24}$$

where s_E is the compliance matrix, and d is the piezoelectric coupling matrix. This constitutive relationship is written in Voigt notation.

For boundary conditions: A fixed constraint was applied to the boundary where the diaphragm meets the cavity plate. The boundary between the piezoelectric disk and the substrate layer was prescribed as the ground, and an electric potential was prescribed on the other side of the disk. If known, a boundary load based on the pressure differential between inside and outside of the cavity can be applied to one side. This pressure differential can be approximated or used to interface with external model or experimental data. The pressure differential and volume change described below are used to couple the FEM electromechanical diaphragm model with a LEM.

The change in volume (also called the volume displacement) is calculated from the diaphragm displacement:

$$\Delta V = \int_A w \, dA \tag{5-25}$$

where w is the out of plane displacement of the diaphragm. If the SJA has multiple diaphragms as in Figure 5-25, then the summed total of the volume displacements is used instead ($\Delta V \rightarrow n\Delta V$ for n identical diaphragms).

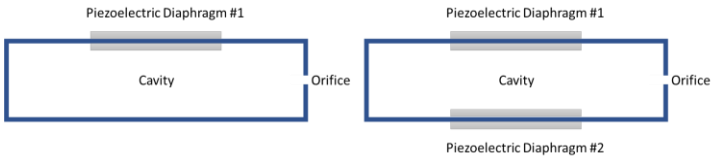

Figure 5-25: SJA with one diaphragm (left) and two diaphragm (right).

Assuming the cavity and diaphragm resonances are uncoupled, a rough approximation of the average jet velocity can be obtained from the operating frequency, the total volume displaced during the maximum-minimum strokes and the orifice area:

$$\overline{U} \approx \frac{1}{f}\frac{(V_{\max} - V_{min})}{A_o} \tag{5-26}$$

2. Cavity-Orifice Acoustics Model

The first eigenfrequency predicted using a pressure acoustic FEM model was assumed to be the cavity-orifice's characteristic resonance. The orifice exit was prescribed to have zero differential pressure, while all remaining surfaces were modeled as hard walls.

In time-domain, the wave equation governs the pressure waves in a lossless medium [30]:

$$\frac{1}{\rho_0 c^2}\ddot{p} + \nabla \cdot \left(-\frac{1}{\rho_0}(\nabla p - q_d)\right) = Q_m \tag{5-27}$$

where $\rho_0$is the density of the fluid, c is the speed of sound, q_d is the dipole domain source, and Q_m is the monopole domain source. Domain sources q_d and Q_m are assumed not to be present.

If the pressure and source terms are assumed to have the same harmonic dependence, the wave equation becomes the inhomogeneous Helmholtz equation:

$$\nabla \cdot \left(-\frac{1}{\rho_0} (\nabla p - q_d) \right) - \frac{\omega^2 p}{\rho_0 c} = Q_m \tag{5-28}$$

a) Validation of Cavity-Orifice Acoustics FEM Model

The acoustic FEM model was validated against an ideal Helmholtz resonator and an ideal Quarter-wave resonator. The resonator geometry consisted of two concentric cylinders corresponding to the cavity and orifice. The orifice's diameter $d_o$was increased to the cavity diameter d_c from $\beta = \frac{d_o}{d_c} \approx 0$ to $\beta = 1$, which correspond to the ideal Helmholtz and Quarter-wave resonators respectively. This was done for cavity heights $h_c = 10, 50, 100$ mm, while keeping the cavity's diameter $d_c = 160$ mm and orifice's neck height $h_n = 5$ mm constant.

Figure 5-26 shows the numerically calculated fundamental acoustic mode of a cavity and orifice as the ratio between the orifice and cavity increases from $\beta = \frac{d_o}{d_c} \approx 0$ to $\beta = 1$. The frequencies are normalized to the quarter-wave frequency calculated using the total length of the cavity and orifice. An end correction to the orifice $\Delta l = 0.61 d_o$ was used to calculate the Helmholtz frequency. For each cavity height, the FEM results matched the resonance frequency described by Equation 5-9 for Helmholtz resonators while the orifice cross-section was much smaller than the cavity cross-section. As the orifice diameter increases, the resonator deviates from the ideal Helmholtz resonator and eventually starts to look more like a quarter-wave resonator.

When the orifice's cross section is the same as the cavity's cross section, the FEM prediction matches the quarter-wave frequency described by Equation 5-11.

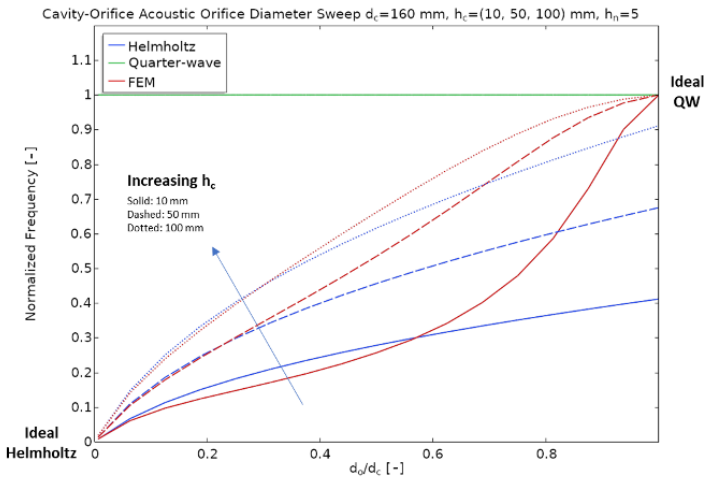

Figure 5-26: Numerically calculated resonance frequency compared with the quarter-wave and Helmholtz frequencies as the diameter of the orifice increases for cavity-orifice with d_c=160 mm, h_c=10,50,100 mm, and h_n=5 mm.

The acoustics model was also validated against measurements from Van Buren's study [10] on cavities that deviate greatly from an ideal Helmholtz resonator. The FEM model predicted the resonances found in the fifth figure within about 3.62%, 0.31% and 0.28% for Apparatus A and 3.50%, 6.56% and 5.71% for Apparatus B, validating the acoustics model for geometries with flat cavities and wide orifices.

C. Coupled Model

The fluid dynamics approach used in this coupled model closely follows Sharma's LEM [16] which was derived from the unsteady continuity and Bernoulli's equations. Instead of modeling the deformation of the diaphragm as a single degree-of-freedom system, the FEM diaphragm model described previously is used to find the diaphragm's deformation. The cavity is

also not assumed to be large relative to the orifice. Occurrences of the Helmholtz frequency are replaced with a more general characteristic frequency ω_{ch}. Accounting for these changes, the two fluid dynamics-based differential equations are solved simultaneously with the FEM model of the diaphragm:

$$\frac{V_c}{\gamma P_0}\dot{p}_i - \Delta\dot{V} = -A_o U \tag{5-29}$$

$$\ddot{U} + \frac{K}{l_e}|U|\dot{U} + \omega_{ch}^2 U = \frac{\Delta\dot{V}}{A_o}\frac{\gamma A_o P_0}{\rho_a l_e V_c} = \frac{\Delta\dot{V}}{A_o}\omega_{ch}^2 \tag{5-30}$$

where V_c is the nominal cavity volume, γ is the specific heat ratio, P_0 is the ambient pressure, p_i is the pressure difference between the cavity and ambient pressures, ΔV is the change in volume, A_o is the area at orifice exit, U is the jet velocity at the orifice exit, K is the loss coefficient, l_e is the effective neck length, ω_{ch} is the characteristic resonance frequency of the cavity-orifice, and ρ_a is the density of air. The model assumes that the air undergoes isentropic contractions and expansions in the cavity, and that the changes in internal cavity pressure, air density, and cavity volume are relatively small. For SJA models assuming a large cavity and small orifice, the characteristic frequency is the Helmholtz frequency ω_H. Depending on the shape of the cavity and orifice, the oscillations cannot always be assumed to be restricted to the neck/orifice of the resonator [24]. To account for these cases, the acoustics FEM model described previously is used to calculate a numerical characteristic frequency ω_{FEM}. Like before, the change in volume is calculated from the diaphragm's displacement:

$$\Delta V = n\int_A w\, dA \tag{5-31}$$

Assuming harmonic behavior for the pressure and volume displacement, Equations 5-29 and 5-30 are rewritten in the frequency domain:

$$i\omega\left(\frac{V_c}{\gamma P_0}p_i - \Delta V\right) = -A_o U \tag{5-32}$$

$$-\omega^2 U + i\omega\frac{K}{l_e}|U|U + \omega_H^2 U = i\omega\frac{\Delta V}{A_o}\omega_H^2 \tag{5-33}$$

1. Estimating the Loss Coefficient K

In Sharma's model, the unsteady Bernoulli's equation was applied to the region between a point sufficiently far inside the cavity (where flow velocity was assumed to be negligible) and the vena contracta (where the flow's cross-section is at a minimum). This would result in a loss coefficient defined by:

$$K = C_L + \frac{1}{C_c^2} \tag{5-34}$$

where C_L is the geometric loss due to sudden contraction of the flow between the cavity and orifice, while $C_c = \frac{A_{vc}}{A_o}$ is the contraction ratio between the cross-sectional area at the vena contracta and the orifice exit. While K is called the loss coefficient in this model, the change in the flow's kinetic energy is also grouped into this term.

Since the vena contracta is defined to be at the flow's smallest cross-section, this definition of the loss coefficient always results in a value greater than 1. However, Sharma suggested a loss coefficient ranging between 0.42 and 1.0, while models reported in literature [13,16,17] have used values ranging between from K= 0.78 to K=1.14.

Figure 5-27 shows the frequency response of Cavities A.1 and A.4 for various values of K. Typical values of K used or suggested by models in literature would result in predictions that were overly damped compared to experimental results. A good estimate for the loss coefficient should provide a value close to $K \approx 0.2$ for Cavity A.1 and $K \approx 0.42$ for Cavity A.4. Both values are much lower than what Sharma's formula suggests [16] and values of K on this order are considered

to be mostly non-physical by [20]. The first peak is much more sensitive to K at lower values, after which the most significant changes are seen with the gradual frequency shift downwards of the second peak as the damping coefficient is increased. Similar observations have been noted by [13,14,20–22].

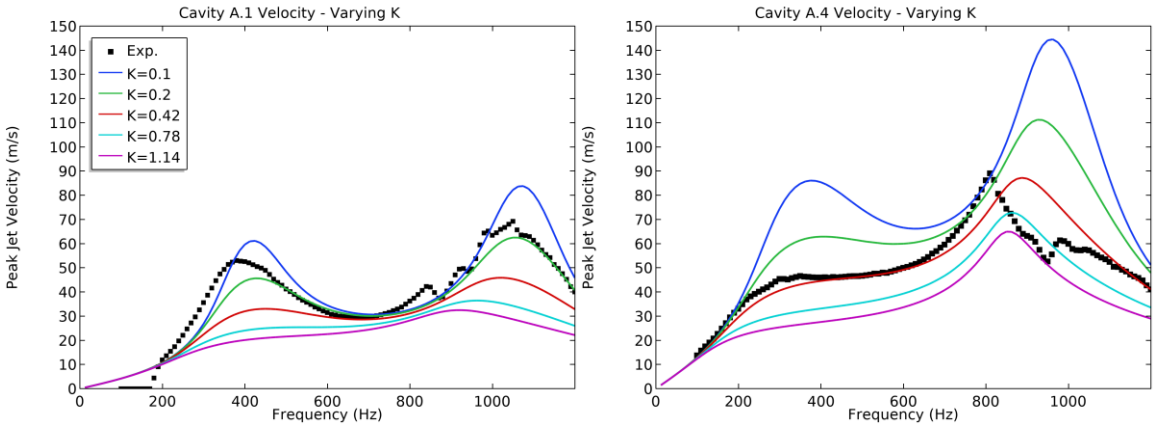

Figure 5-27: Effect of the Loss Coefficient K on the peak jet velocity of Cavities A.1 (left) and A.4 (right).

Sharma's application of the unsteady Bernoulli's equation between a point where the flow velocity is negligible and the vena contracta does not provide an accurate estimate of the loss coefficient even for the SJAs studied by Sharma. To better account for the low values of K expected for these actuators, the unsteady Bernoulli's equation is instead applied to a point inside the cavity with flow velocity U_i, and at the orifice exit instead of the vena contracta:

$$P_i + \frac{1}{2}\rho U_i^2 = \rho \int_{s1}^{s2} \frac{\partial U}{\partial t} ds + P_0 + \frac{1}{2}\rho U_o^2 + Losses \tag{5-35}$$

Pressure and velocity terms are grouped together to define the pressure differential p_i, and the work to change the streamline's momentum can be rewritten as $\rho l_e \dot{U}$ instead of the integral form:

$$P_i - P_0 = \rho l_e \dot{U} + \frac{1}{2}\rho U_o^2 - \frac{1}{2}\rho U_i^2 + \frac{1}{2}\rho \sum K_{geo} U_o^2 \tag{5-36}$$

where the head losses are described by $\frac{1}{2}\rho\sum K_{geo}U_o^2$.

Multiplying $\frac{1}{2}\rho U_i^2$ by U_o^2/U_o^2 and gathering like terms becomes:

$$p_i = \rho l_e \dot{U} + \frac{1}{2}\rho K U_o^2 \tag{5-37}$$

Where the loss coefficient is

$$K = \sum K_{geo} + 1 - \frac{U_i^2}{U_o^2} \tag{5-38}$$

This loss coefficient includes both the head losses and kinetic recovery. Equation 5-38 similar form to Sharma's equation, except it allows values of $K < 1$. Although the velocity at the inner point is not known, the ratio U_i^2/U_o^2 is assumed to be some function of the area/diameter ratio $\beta = \sqrt{\frac{A_o}{A_i}} = \frac{d_o}{d_i}$. The center of the cavity (also the maximum cross-section) is used for d_i. With this, the loss coefficient becomes:

$$K = \sum K_{geo} + 1 - f(\beta) \tag{5-39}$$

The function $f(\beta) = \beta^2$ was chosen for this model. With this definition, $f(\beta) \to 0$ for geometries where the orifice's cross-section is much smaller than the cross-section of the cavity. This corresponds to the case where the velocity in the cavity is negligible and becomes identical to Sharma's loss coefficient based on an ideal Helmholtz resonator. If the cavity and exit cross-sections are the same (such as in a quarter-wave resonator), then $f(\beta) = 1$. This corresponds to the case where the velocity inside the cavity is the same as the exit velocity (in reality, the velocity of the air should decrease the deeper inside the resonator).

The sum of geometric losses $\sum K_{geo}$ accounts for energy losses due to the geometry of the cavity and orifice as the air flows in and out. While the transition between the cavity and orifice in

the SJA geometries studied is technically not a sudden/sharp contraction, this study assumes it can be approximated as a sudden contraction from the maximum cross-section of the cavity to the orifice. The losses due to sudden contraction has been empirically found to follow the following equation based [31] form:

$$K_{SC} \approx \begin{cases} 0.42(1-\beta^2) & for\ \beta \leq 0.76 \\ (1-\beta^2)^2 & \beta > 0.76 \end{cases} \tag{5-40}$$

Since the cross-sections of the orifice and cavity are not circular, the hydraulic diameter d_H is used to calculate β:

$$d_H = \frac{4\mathrm{A}}{\mathrm{P}} \tag{5-41}$$

where A is the area and P is the wetted perimeter of the cross-section. The hydraulic diameter is often used for non-circular pipes and has also been used for SJA models [7,32]. Although not part of the SJAs studied here, head losses due to friction in long orifices or due to bends can be included in $\sum K_{geo}$.

2. Validation of replacing ω_H with ω_{FEM} in SJA model

Most modeling tools for SJAs use the Helmholtz frequency as the characteristic frequency, however, Van Buren noted that the Helmholtz resonance may not always be appropriate such as when the assumptions of a large cavity and small orifice are broken. The effects of using the Helmholtz ω_H, quarter-wave ω_{QW}, and numerically calculated ω_{FEM} resonance frequencies in place of the characteristic frequency are compared to experiments for Cavities A.1 and A.4. Cavity A.4 was chosen due to the shape of its frequency responses being distinct from A.1.

In Figure 5-28 and Figure 5-29, Cavity A.1 and A.4's frequency responses for flow and diaphragm displacement are plotted changing only the characteristic resonance frequency

($\omega_H, \omega_{QW}, \omega_{FEM}$). The locations of the uncoupled Helmholtz, quarter-wave and numerical frequencies are plotted as blue, green, and red vertical dotted lines for f_H, f_{QW}, and f_{FEM} respectively. The diaphragm resonance f_w calculated from the uncoupled structural model is designated by the black vertical dashed line. In Figure 5-28a, the frequency shifts between the uncoupled and coupled resonances are pointed out by the colored arrows. Each choice was able to yield the two peaks seen in the experimental data for Cavity A.1; while for Cavity A.4, only $\omega_{FEM}$was able to capture the shape of the experimental data for both the velocity and displacement. The calculated values of the loss coefficient K for Cavities A and F are 0.20 and 0.65 respectively using Equation 5-38.

Since the shape of the frequency response is primarily determined by the loss coefficient K as shown by Figure 5-27, the suitability of each of the three frequencies will be assessed by the frequency of the peaks rather than the magnitude. The peaks are not expected to shift as much frequency-wise compared to the amplitude due to the value of K. This metric was chosen to limit bias when assessing the use of ω_H, ω_{QW} and ω_{FEM} since K is a tuning parameter in other models and the values of K used here were estimated using an equation developed for this work.

The structural resonance peaks were predicted within 160-180 Hz (42%-55%) using ω_H, within 80-100 Hz (24%-27%) using ω_{QW}, and within 20-50 Hz (7%-14%) using ω_{FEM}. The acoustic resonance peaks were predicted within 50-1000+ Hz (6%-100+%) using ω_H, within 10-150 Hz (2%-15%) using ω_{QW}, and within 10-60 Hz (2%-8%) using ω_{FEM}. In addition to predicting the resonance frequencies the best of the three, the relative shapes of the frequency responses using ω_{FEM} were also close to the experimental measurements using the estimated loss coefficients. In the case of the displacements for A.4, using the Helmholtz resonance resulted in an absent peak despite being present using the other two resonances.

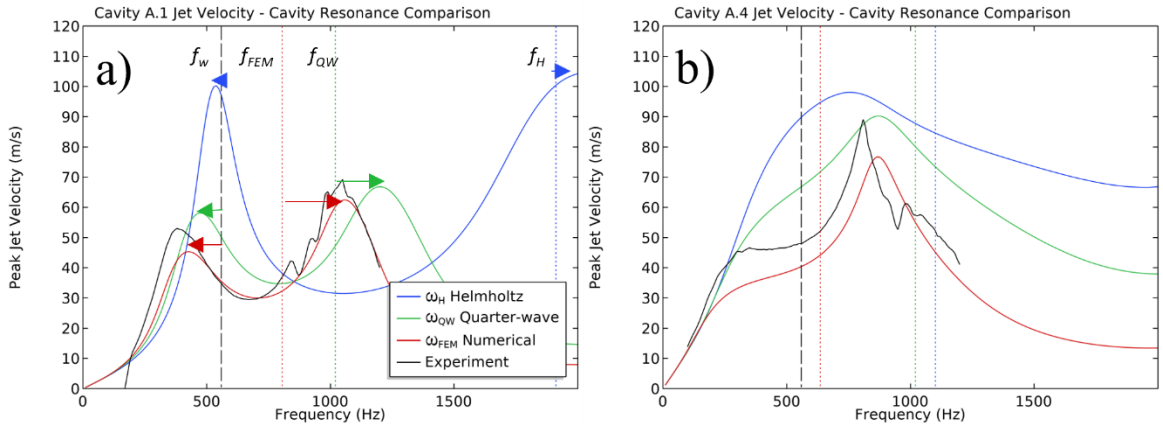

Figure 5-28: Effect of the cavity resonance on the frequency response (peak jet velocity) for Cavities A.1 (a) and A.4 (b).

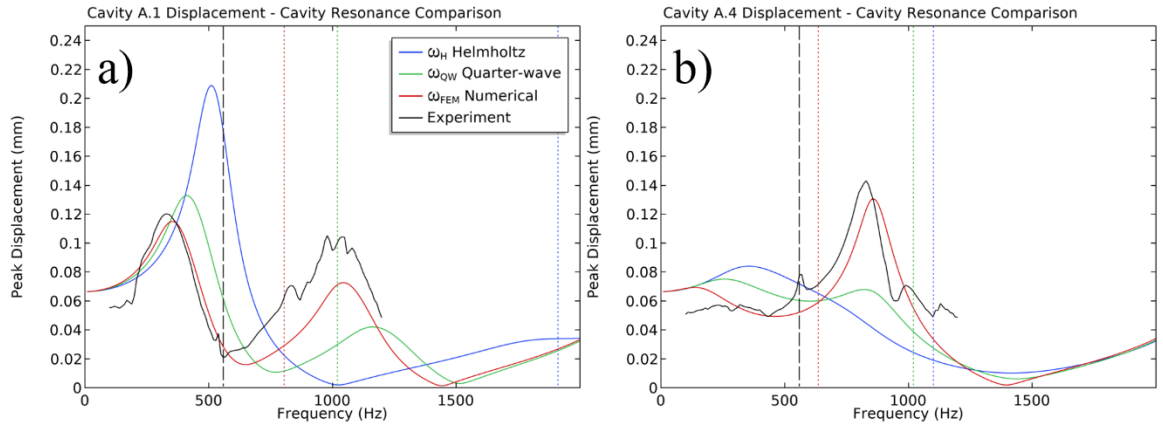

Figure 5-29: Effect of the cavity resonance on the frequency response (center displacement) for Cavities A.1 (a) and A.4 (b).

V. Results

A. Experiment vs. Coupled Model

Table 5-5 and Table 5-6 below respectively list the resonance frequencies of Cavities A.1-A.5 and Cavities B.1-B.5 predicted by the FEM model, the Helmholtz frequency equation, and the quarter-wave frequency equation, and the loss coefficient *K*. Because there is not an established

effective length for these geometries, The Helmholtz frequency listed in the table uses the nominal orifice length without end correction. There is a shift downwards of about 100-300 Hz for f_H using both the typical definitions and the fitted formula by [29]. In general, f_H is about two to three times the numerical f_{FEM}, whereas f_{QW} did not change based on the orifice cross-section for the same cavity diameters. The frequencies in Table 5-5 and Table 5-6 account for the space occupied by the piezoelectric disks inside the cavity.

Table 5-5: Cavity A Acoustic Resonances (Hz) and Loss Coefficient

Cavity	A.1	A.2	A.3	A.4	A.5
f_{FEM}	805.5	791.7	854.3	636.2	821.1
f_{H}	1911.8	1811.3	2200.8	1101.2	2210.3
f_{QW}	1020.8	1020.8	1020.8	1020.8	1020.8
K	0.20	0.29	0.14	0.65	0.12

Table 5-6: Cavity B Acoustic Resonances (Hz) and Loss Coefficient

Cavity	B.1	B.2	B.3	B.4	B.5
f_{FEM}	665.6	656.7	672.0	698.1	601.8
f_{H}	1564.7	1503.2	1630.0	1735.8	1227.4
f_{QW}	875.0	875.0	875.0	875.0	875.0
K	0.20	0.28	0.15	0.20	0.44

1. Cavities A.1-A.4

Figure 5-30 and Figure 5-31 show the frequency responses of Cavities A.1-A.4 for the jet velocity and the center displacement respectively. Results from Cavity A.5 are presented separately in a later section. A breakdown of the frequencies and amplitudes are listed in Table 5-7 and Table 5-8. The model uses the numerically calculated resonance from Table 5-5 and estimates the loss coefficient using Equation 5-38. The model was stepped at 10 Hz increments to construct the frequency response from 0 to 1200 Hz. Model predictions are shown with solid lines and measured data with points. There are common irregularities in the measured frequency responses at around

550 Hz, 830 Hz, 950 Hz and 1100 Hz. These irregularities are attributed to the resonant modes of the stand holding the SJAs during experiments.

The frequencies of the peak jet velocity were predicted within 10-60 Hz (2%-14%), and the peak jet velocity amplitudes within 2-13 m/s (5%-24%). The frequencies of the peak displacement were predicted within 10-30 Hz (2-9%), and the displacements amplitudes within 0.005-0.41 mm (5-41%). A closer look shows that the displacements for the first peak were predicted within 0.005-0.022 mm (5-15%). For the second peak, Cavities A.1-A.3 underpredicted by about 0.03-0.04 mm (30-40%) and Cavity A.4 underpredicted by 0.015 mm (8.4%). Vibrations from the stand around the second peak would be consistent with this discrepancy. Cavity A.4's sharp decline is also likely due to destructive interference from those vibrations.

Using Cavity A.1 and Equations 5-12 - 5-15 as an example to calculate the shifted resonances using the uncoupled models: the diaphragm's structural resonance is $\omega_w = 2\pi \cdot 560Hz$, the cavity's acoustic resonance $\omega_{ch} = 2\pi \cdot 805\ Hz$, and diaphragm-cavity pneumatic resonance $\omega_{wp} = \sqrt{\frac{\gamma A_w^2 P_0/V_c}{m_w}} = \sqrt{\frac{1.4(5\times10^{-3}m^2)^2(1.01\times10^5 Pa)/(8.70\times10^{-6}\ m^3)}{0.03kg}} = 2\pi \cdot 586Hz$. The resonances ω_w and ω_H were found using the two uncoupled diaphragm and cavity models to the nearest 10 Hz.

$$\omega_{1,2}^2 = (2\pi)^2 \frac{-(1.31\times10^6) \pm \sqrt{(1.31\times10^6)^2 - 8.13\times10^{11}}}{2} Hz^2 \tag{5-42}$$

$$f_{1,2} = \frac{\omega_{1,2}^i}{2\pi} = \begin{cases} 424\ Hz \\ 1063\ Hz \end{cases} \tag{5-43}$$

Note that frequencies of the peaks f_1^U and f_2^U (model:430 Hz and 1060 Hz) for Cavity A.1 agrees very well with example above and shows that the model handles the coupling between the cavity and diaphragm consistently with other models in literature [17].

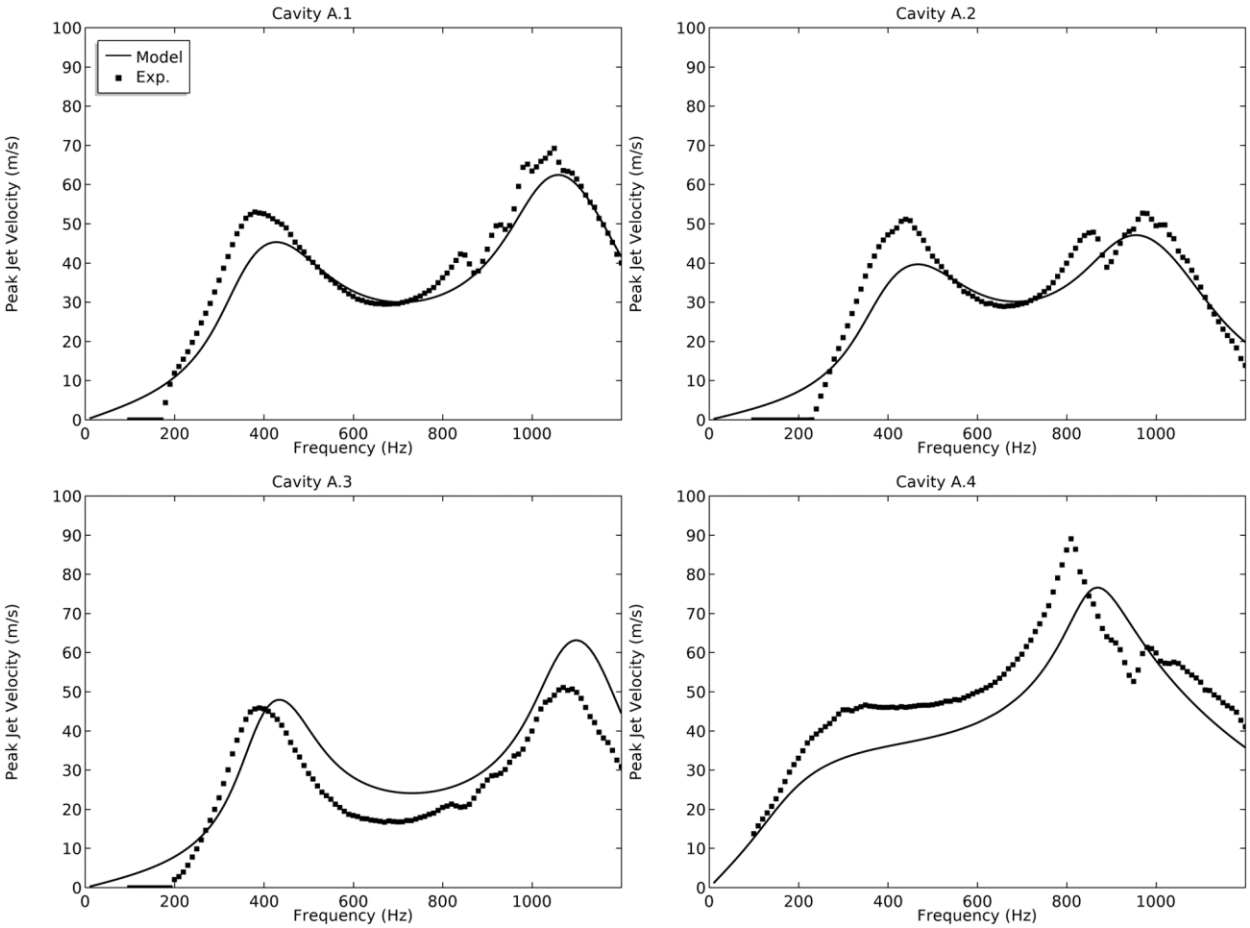

Figure 5-30: Frequency response for the peak jet velocity of Cavities A.1-A.4. (Solid: Model; Points: Experiment)

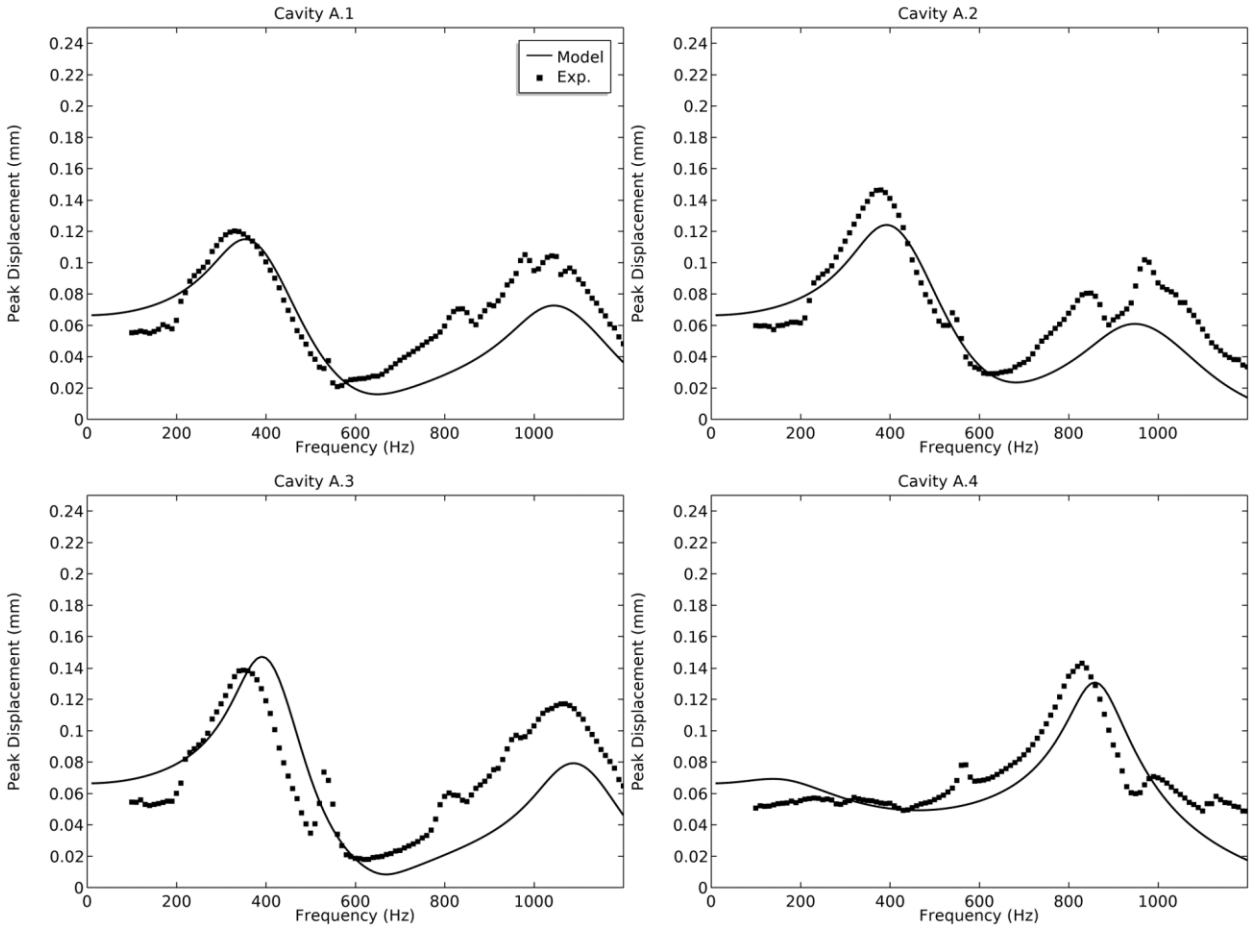

Figure 5-31: Frequency response for the peak center displacement of Cavities A.1-A.4. (Solid: Model; Points: Experiment)

Table 5-7: Cavity A Resonance (Hz) and Flow Velocity (m/s)

		A.1	A.2	A.3	A.4
Exp.	f_1^U(Hz)	380	440	390	-
	U_{f_1}(m/s)	53.1	51.2	45.9	-
	f_2^U(Hz)	1050	970	1070	810
	U_{f_2}(m/s)	69.2	52.8	51.1	89.1
Model	f_1^U	430	470	430	-
	U_{f_1}	45.4	39.7	48.0	-
	f_2^U	1060	960	1100	870
	U_{f_2}	62.5	47.1	63.2	76.7
% Diff.	f_1^U(%)	13.2	6.8	10.3	-
	U_{f_1}	-14.5	-22.5	4.5	-
	f_2^U	1.0	-1.0	2.8	7.4
	U_{f_2}	-9.8	-10.7	23.6	-13.9

Table 5-8: Cavity A Resonance (Hz) and Center Displacement (mm)

		A.1	A.2	A.3	A.4
Exp.	f_1^w(Hz)	330	380	360	-
	w_{f_1}(mm)	0.120	0.146	0.139	-
	f_2^w	1010*	970	1070	830
	w_{f_2}	0.105	0.102	0.117	0.143
Model	f_1^w	350	390	390	-
	w_{f_1}	0.115	0.124	0.147	-
	f_2^w	1040	950	1090	860
	w_{f_2}	0.073	0.061	0.079	0.131
% Diff.	f_1^w(%)	6.1	2.6	8.3	-
	w_{f_1}	-4.4	-15.3	6.0	-
	f_2^w	3.0	-2.1	1.9	3.6
	w_{f_2}	-30.6	-40.1	-32.6	-8.4

*Averaged between 970 Hz and 1050 Hz.

2. Cavities B.1-B.5

The frequency response for Cavities B.1-B.5 were similarly modeled for frequencies between 0 to 600 Hz at 10 Hz increments. Table 5-9 lists the frequency and amplitude of the flow velocity and displacement at the peaks. The model predicted the resonance frequency within 30

Hz (14%) for each of these cavities. The flow velocity was predicted within about 10 m/s (33%), The displacements were predicted within about 0.02 mm (15%).

Table 5-9: Cavity B Resonance (Hz), Flow Velocity (m/s) and Center Displacement (mm)

		B.1	B.2	B.3	B.4	B.5
Exp.	f_U(Hz)	210	230	180	230	230
	U (m/s)	34.1	35.0	33.8	35.0	34.1
	f_w(Hz)	160	200	140	220	180
	w (mm)	0.133	0.146	0.104	0.165	0.117
Model	f_U	190	210	170	210	210
	U	28.0	25.5	29.7	27.7	23.0
	f_w	160	180	140	190	150
	w	0.127	0.142	0.119	0.184	0.107
% Diff.	f_U(%)	-9.5	-8.7	-5.6	-8.7	-8.7
	U	-17.9	-27.1	-12.1	-20.9	-32.6
	f_w	0.0	-10.0	0.0	-13.6	-16.7
	w	-4.8	-2.9	14.1	11.4	-8.6

B. Thin Cavities and Model Limitations

For the thin SJAs studied in this work, even the space occupied by the piezoelectric disks can affect the SJA response. This is mostly due to the small cavity size, which affects both the stiffness of the cavity and the mass of oscillating air. The volume V_c appears in the LEM equations directly and through the characteristic resonance. Figure 5-32 and Figure 5-33 respectively show the jet velocity and displacement frequency responses for (a) Cavity A.1 and (b) Cavity A.5. The solid lines take the nominal cavity volume to be $V_{c,0} = A_w h_c$, whereas the dashed lines account for the volume occupied by the two piezo disks inside the cavity $V_c = V_{c,0} - 2V_{piezo}$. For Cavity A.1, though the predicted responses are quite similar, there is a slight but measurable shift towards the experimental curve. The trough between the peaks and the decay after the second peak match almost exactly in the velocity frequency response. For Cavity A.5, there is a decrease in the predicted jet velocity amplitude after accounting for volume occupied by the piezoelectric disks, even though the predicted displacements remain similar.

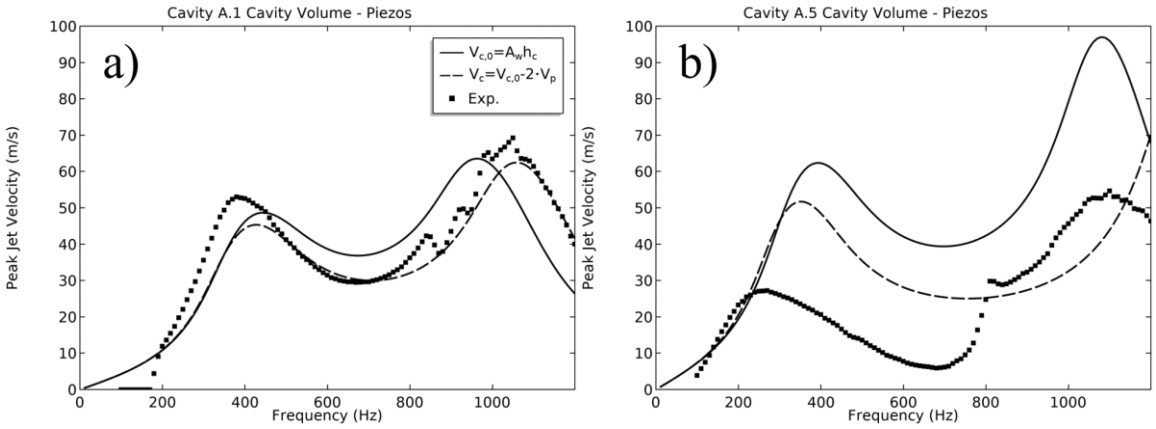

Figure 5-32: Effect of cavity volume on the velocity for a) Cavity A.1 and b) Cavity A.5.

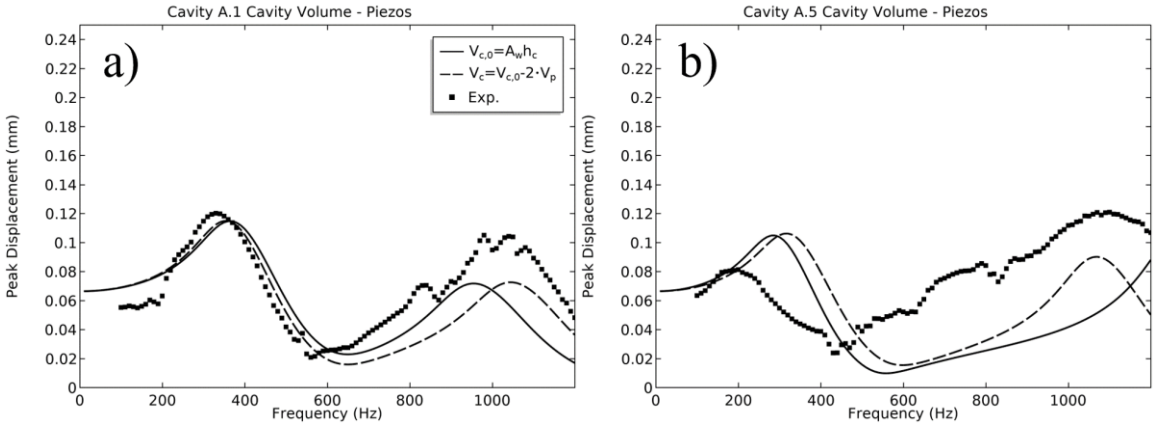

Figure 5-33: Effect of cavity volume on the displacement for a) Cavity A.1 and b) Cavity A.5.

Compared to the other cavities which had good agreement with the model, Cavity A.5 was an outlier in terms of model agreement before and after considering the reduced cavity volume. This cavity was the thinnest among the cavities studied with a height of 1.41 mm. The jet velocity did not increase as expected for a smaller orifice but decreased drastically instead. Even after accounting for the volume decrease, the frequencies for the first velocity and displacement peaks are still overpredicted by about 80 Hz (30%) and 120 Hz (60%), the flow velocity's amplitude by about 24 m/s (100%), and the displacement by about 0.03 mm (30%). Most importantly, the model was able to partially capture the reduced jet velocity of Actuator A.5 as the orifice area shrank. The

remaining discrepancy is suspected to be due to violations of the model's assumption that the change in cavity volume is relatively small compared to the original volume as the diaphragm oscillates.

When modeling novel geometries, checks should be done post-simulation to check if the original assumptions are still valid. Also, if there is a significant difference in the model predictions before and after accounting for the piezoelectric disk volumes, that is a sign the assumptions of small volume changes are no longer valid.

The reduced cavity volume of Cavity A.5 is about 3870 mm^3 with volume changes of about +/- 250 mm^3 for each diaphragm. This corresponds to a volume change of about +/-13% from the nominal volume while oscillating (or about 25-30% between the minimum to maximum cavity volumes after deformation). The next thinnest cavity tested was Cavity B.3 with a cavity height of 1.7 mm. The reduced cavity volume was still much larger at 8580 mm^3 with volume changes about +/- 400 mm^3 for each diaphragm, corresponding to about +/- 9% (or about 17-20% change from minimum to maximum) from nominal. Some other cavities have similar sizes and volume changes to Cavity B.3, so the assumption for small cavity changes still seems to be valid for volume changes under 9%. While the difference between 9% and 13% seems small, this corresponds about a 50% increase in the relative volume displaced.

VI. Further Discussion

A. Characteristic Frequency

It was shown in Section IV-C-2 for Cavities A.1 and A.4 that the locations of the predicted peaks were better aligned to the experimental measurements when using the numerically calculated resonances compared to using the Helmholtz or quarter-wave resonances. Additionally, Section IV-B-2a showed that for a cavity and orifice made up of concentric cylinders, the

numerically calculated resonance frequency was identical to the Helmholtz and quarter-wave frequencies at the extreme cases ($\beta = \frac{d_o}{d_c} \approx 0$ and $\beta = 1$). Since the Helmholtz resonance naturally appeared in the development of the LEM, this implies that another characteristic resonance should naturally appear instead of the Helmholtz resonance without those assumptions. This is consistent with Alster's theory that connected the two cases to the same underlying physics.

Recall the Helmholtz resonance equation. This assumed that the oscillating mass of air is largely restricted to orifice and the spring to the cavity. This no longer holds for geometries that deviate greatly from the Helmholtz resonator, and it may be helpful to consider Alster's theory which accounted for additional mass inside the resonator instead.

B. Alster's Extended Theory for Helmholtz Resonators

In Alster's theory, a form factor l_v was defined based on the cavity geometry:

$$l_v = \int_x \frac{A_o}{A(x)} \frac{V(x)^2}{V_c^2} dx \approx \frac{A_o}{V_c l_c} \int_0^{l_c} \frac{xV(x)}{A(x)} dx \tag{5-44}$$

where $V(x)$ is the volume inside the cavity from the origin to position x and $A(x)$ is the cross-sectional area at x. This accounts for oscillating air inside the resonator that is typically neglected in the end corrections used to correct for the Helmholtz frequency. For the derivation, see this chapter's Appendix.

Alster provides several formulas for the resonance of various fundamental shapes (e.g. sphere, prism, cone) using the approximation $\frac{V(x)}{V} \approx \frac{x}{l_c}$ for one set of the ratios to simplify the integration. These formulas can still be quite complicated, and the simplification also obscures any physical meaning that can be gleamed from the formulas. To get a more intuitive understanding

what is happening physically, the form factor is calculated for a simple geometry without assuming one of the volume ratios $\frac{V(x)}{V}$ as $\frac{x}{l_c}$.

Consider a system where the cavity and orifice each have a constant cross-section (such as in the case of the cavity and orifice being concentric cylinders). The cavity has a cross-section A_c and length l_c, while the orifice has a cross-section A_o and nominal neck length l_n.

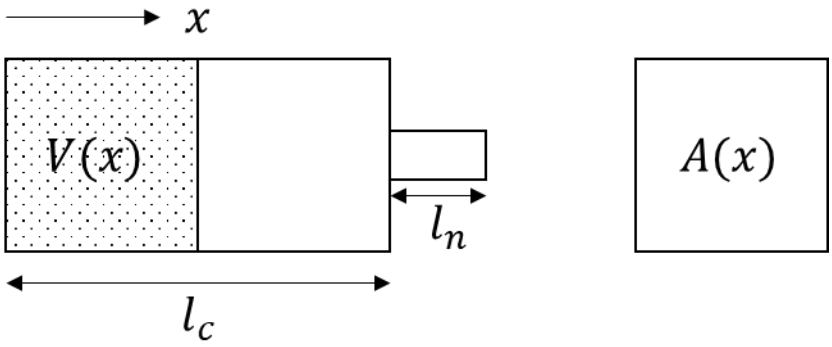

Figure 5-34: Illustration of resonator with cavity length l_c and neck length l_n.

The form factor needs to be calculated for both the cavity and orifice, so Equation 5-44 becomes:

$$l_{v-n} = \int_0^{L=l_c+l_n} \frac{A_N}{A(x)} \frac{V(x)^2}{(V_c+V_o)^2} dx \tag{5-45}$$

where

$$A(x) = \begin{cases} A_c & 0 \le x \le l_c \\ A_o & l_c \le x \le l_c + l_n \end{cases} \tag{5-46}$$

and

$$V(x) = \begin{cases} A_c x & 0 \le x \le l_c \\ A_c l_c + A_o(x-h) & l_c \le x \le l_c + l_n \end{cases} \tag{5-47}$$

The resulting integrations becomes:

$$l_{v-n} = \frac{A_o}{A_c} \frac{A_c^2 \cdot \frac{l_c^{\,3}}{3}}{(V_c+V_o)^2} + \frac{A_c^2 l_c^2 l_n + A_c l_c A_o l_n^2 + \frac{A_o^2 l_n^3}{3}}{(V_c+V_o)^2} \tag{5-48}$$

$$l_{v-n} = \beta^2 \frac{\frac{V_c^2}{3}}{(V_c + V_o)^2} l_c + \frac{V_c^2 + V_c V_o + V_o^2 \frac{1}{3}}{(V_c + V_o)^2} l_n = l_{v-n}^{(1)} + l_{v-n}^{(2)} \tag{5-49}$$

where $l_{v-n}^{(1)}$ and $l_{v-n}^{(2)}$ can be considered the contributions from the cavity and neck respectively. The cavity and orifice neck lengths are modified by area and volume ratios depending on the geometry. Contributions from outside the resonator are added separately to form the effective neck length but are not considered here. Some test scenarios are described below:

- The orifice is much smaller than the cavity ($V_o \ll V_c$)) and $\beta \to 0$, $l_{v-n} = l_n$ since $l_{v-n}^{(1)} \to 0$ and $l_{v-n}^{(2)} \to l_n$. This corresponds to the Helmholtz resonator.
- The orifice volume is small ($V_o \ll V_c$) but the area ratio is not ($\beta \approx 0$), then $l_{v-n} = \frac{1}{3}\beta^2 l_c + l_n$ since $l_{v-n}^{(1)} \to \frac{1}{3}\beta^2 l_c$ and $l_{v-n}^{(2)} \to l_n$.
- The orifice volume is small ($V_o \ll V_c$) and $\beta = 1$, $l_{v-n} \approx \frac{1}{3} l_c$. This corresponds to the quarter-wave resonator.

The overall form factor is some function of the area ratio, cavity and orifice volumes, and cavity and orifice neck lengths. Having a large orifice area means more that the contribution from inside the cavity are significant. Notice that the neck's contribution $l_{v-n}^{(2)}$ can also be rewritten as:

$$l_{v-n}^{(2)} = \frac{V_c^2 + 2V_c V_o + V_o^2 - V_c V_o - \frac{2}{3} V_o^2}{(V_c + V_o)^2} l_n = \left(1 - \frac{V_c V_o + \frac{2}{3} V_o^2}{(V_c + V_o)^2}\right) l_n \tag{5-50}$$

In this arrangement, it is easier to see that as the volume of the orifice increases from $\beta = 0$, the ratio will decrease slightly. Unless the orifice neck is long, this decrease is likely to be small for most resonator geometries and dominated by the increase from $l_{v-n}^{(1)}$.

VII. Conclusion

A reduced-ordered model was developed for a piezoelectrically-driven SJA by combining finite-element and lumped-element techniques. LEM models for SJAs typically require fitting parameters to the loss coefficient K and the diaphragm deformation to achieve good agreement with experimental data. The reliance on these parameters limits the predictive capabilities of existing LEMs for new configurations without requiring extensive fitting. Fitted parameters become less reliable the more the modeled SJA differs from the fitted data's original configuration. LEMs are sensitive to the choice of the characteristic frequency and the loss coefficient, so accurate estimates of the two are needed. SJA models are also sensitive to the choice of the characteristic frequency which can be significantly different from the Helmholtz frequency for certain geometries.

The experimental results were able to be predicted successfully by replacing the Helmholtz resonance frequency in the LEMs with a more generic characteristic frequency and deriving an estimate for the loss coefficient. Aside from one cavity, the locations of most peaks were predicted within about 17%. The amplitudes of the jet velocities were predicted within 25.4% with most predictions being within 5-10 m/s of the measured data. This is a significant improvement from using the Helmholtz resonance, which differed as high as 55%-100+% depending on the parameter and cavity geometry.

The presented model was able to capture the shape of the frequency responses as well as the relative shifts as parameters were varied. Compared to prior models, this is a huge improvement in capturing the behavior of SJAs with small cavities and/or large orifices. This methodology will be helpful to predict and optimize performance of the SJAs in unexplored design spaces. The

diaphragm FEM model can easily be adapted to other materials, from 2D to 3D, and even to different actuation mechanism.

).

VIII. Appendix

Alster developed a theory to calculate the resonance frequency of resonators for several fundamental shapes. The formula was developed for an axially symmetric resonator, but was also applied to moderately non-symmetric shapes.

While classical theory has considered end correction to the neck length to account for mass oscillating near the neck/orifice, Alster deviates from the classical theory by assuming there is air oscillating throughout the inside of the resonator. For simplicity, the velocity is assumed to be constant within a given cross-section.

Derivation

Consider a small volume dV within the cavity. The mass dM for that volume is

$$dM = \rho\, dV \tag{5-A-1}$$

where ρ is the air's density.

Assuming an adiabatic process, the relationship between the change of pressure due to a change in volume can be derived from Poisson's Law:

$$pV^k = constant \tag{5-A-2}$$

This leads to

$$V^k dp + pkV^{k-1} dV = 0 \tag{5-A-3}$$

$$dp = -\frac{pk}{V} dV = -\frac{pk}{V} A dx \tag{5-A-4}$$

The mass at any cross section $A(x)$ also works against the stiffness of the air between it and the wall.

Assuming the same change in pressure in the neck and within in the cavity:

$$dp = -\frac{pk}{V} A_N dx_N = -\frac{pk}{V(x)} A(x) dx \tag{5-A-5}$$

$$dx = \frac{A_N}{A(x)}\frac{V(x)}{V}\,dx_N \tag{5-A-6}$$

Taking the time derivative of

$$\frac{d}{dt}dx = \frac{d}{dt}\left(\frac{A_N}{A(x)}\frac{V(x)}{V}\,dx_N\right) = \frac{A_N}{A(x)}\frac{V(x)}{V}\frac{d}{dt}\,dx_N + dx_N\frac{d}{dt}\left(\frac{A_N}{A(x)}\frac{V(x)}{V}\right) \tag{5-A-7}$$

If the changes in $V(x)$ and $A(x)$ are slow, then the time derivative can be approximated as

$$u = \frac{A_N}{A(x)}\frac{V(x)}{V}\,u_N \tag{5-A-8}$$

The kinetic energy at a cross section can be expressed as:

$$dW = \frac{1}{2}\rho A(x)dxu(x)^2 \tag{5-A-9}$$

This can be written in terms of the exit velocity using the ratio in Equation 5-A-8.

$$dW = \frac{1}{2}\rho A(x)dx\left(\frac{A_N}{A(x)}\frac{V(x)}{V}\,u_N\right)^2 = \frac{1}{2}\rho\frac{A_N^2}{A(x)}\frac{V(x)^2}{V^2}u_N^2dx \tag{5-A-10}$$

The total kinetic energy can be expressed as the integral

$$W = \int dW = \int_x \frac{1}{2}\rho\frac{A_N^2}{A(x)}\frac{V(x)^2}{V^2}u_N^2dx = \frac{1}{2}\rho u_N^2\int_x\frac{A_N^2}{A(x)}\frac{V(x)^2}{V^2}dx \tag{5-A-11}$$

An equivalent length l_v Alster calls the form factor can be used to account for the additional mass inside the cavity:

$$W = \frac{1}{2}\rho l_v A_N u_N^2 \tag{5-A-12}$$

where

$$l_v = \int_x\frac{A_N}{A(x)}\frac{V(x)^2}{V^2}dx \tag{5-A-13}$$

Alster approximates one of the volume ratios $\frac{V(x)}{V}$ with $\frac{x}{L}$ and multiplies the form factor by a coefficient to reduce the error introduced by the approximation from Equation 5-A-8. The

formulas for various fundamental resonator shapes were provided in Alster's paper. However, these formulas can still be quite complicated, and the simplification also obscures physical meaning that can be gleamed from the formulas. To get a better qualitative understanding of the underlying physics, Equation 5-A-13 is applied to a cavity and orifice that can be easily integrated without those modifications.

Application to Simple Geometry without Alster's Approximation

Consider a system where the cavity and orifice each have a constant cross-section (such as a concentric cylindrical). The cavity has a cross-section A_c and length l_c (referred to as height h in Alster's work), while the orifice has a cross-section A_o and nominal neck length l_n.

When Equation 5-A-13 is applied to both a cavity and orifice, the equation becomes:

$$l_{v-n} = \int_0^{L=l_c+l_n} \frac{A_N}{A(x)} \frac{V(x)^2}{(V_c+V_o)^2} dx \tag{5-A-14}$$

$$A(x) = \begin{cases} A_c & 0 \le x \le l_c \\ A_o & l_c \le x \le l_c + l_n \end{cases} \tag{5-A-15}$$

and

$$V(x) = \begin{cases} A_c x & 0 \le x \le l_c \\ A_c l_c + A_o(x-h) & l_c \le x \le l_c + l_n \end{cases} \tag{5-A-16}$$

Substituting $A(x)$ and $V(x)$

$$l_{v-n} = \int_0^{l_c} \frac{A_o}{A(x)} \frac{V(x)^2}{(V_c+V_o)^2} dx + \int_{l_c}^{l_n} \frac{A_o}{A(x)} \frac{V(x)^2}{(V_c+V_o)^2} dx \tag{5-A-17}$$

$$l_{v-n} = \int_0^{l_c} \frac{A_o}{A_c} \frac{(A_c x)^2}{(V_c+V_o)^2} dx + \int_{l_c}^{l_c+l_n} \frac{A_o}{A_o} \frac{(A_c l_c + A_o(x-h))^2}{(V_c+V_o)^2} dx \tag{5-A-18}$$

$$l_{v-n} = \frac{A_o}{A_c} \frac{A_c^2 \cdot \frac{{l_c}^3}{3}}{(V_c+V_o)^2} + \frac{A_c^2 l_c^2 l_n + A_c l_c A_o l_n^2 + \frac{A_o^2 l_n^3}{3}}{(V_c+V_o)^2} \tag{5-A-19}$$

Since $V_c = A_c l_c$ and $V_o = A_o l_n$:

$$l_{v-n} = \frac{A_o}{A_c} \frac{\frac{V_c^2}{3}}{(V_c + V_o)^2} l_c + \frac{V_c^2 + V_c V_o + V_o^2 \frac{1}{3}}{(V_c + V_o)^2} l_n \tag{5-A-20}$$

This form factor is a function of the orifice and cavity cross-sections and volumes. When $A_o \ll A_c$ and $V_o \ll V_c$, the oscillating mass inside the cavity become negligible and l_{v-n} reduces to l_n.

When $A_o \ll A_c$ no longer holds but $V_o \ll V_c$ is still true, Equation 5-A-20 becomes:

$$l_{v-n} = \frac{A_o}{A_c} \frac{l_c}{3} + l_n \tag{5-A-21}$$

The quarter-wave resonator corresponds to the case where $A_o \to A_c$. Ignoring end correction, the formula for the quarter-wave frequency equation is:

$$f_{QW} = \frac{1}{4} \frac{U_s}{l_c} \tag{5-A-22}$$

Calculating the resonance frequency using the form factor:

$$f = \frac{U_s}{2\pi} \sqrt{\frac{A_o}{V_c (l_{v-n})}} = \frac{U_s}{2\pi} \sqrt{\frac{A_o}{A_o l_c \left(\frac{l_c}{3}\right)}} = \frac{\sqrt{3}}{2\pi} \frac{U_s}{l_c} \approx 0.276 \frac{U_s}{l_c} \tag{5-A-23}$$

The frequency from this theory overestimates the quarter-wave frequency by about 10%. The correction by Alster was used to reconcile this.

Although the example assumed both the cavity and orifice to each have a constant cross-section, the formulas for $l_{v-n}^{(1)}$ and $l_{v-n}^{(2)}$

For a cavity with constant cross-section (even if the orifice is not):

$$l_{v-n}^{(1)} = \frac{A_o}{A_c} \frac{\frac{V_c^2}{3}}{(V_c + V_o)^2} l_c \tag{5-A-24}$$

For an orifice with cross-section is constant (even if the cavity is not):

$$l_{v-n}^{(2)} = \frac{V_c^2 + V_c V_o + V_o^2 \frac{1}{3}}{(V_c + V_o)^2} l_n \tag{5-A-25}$$

IX. References

[1] Rathnasingham, R., and Breuer, K. S. “Coupled Fluid-Structural Characteristics of Actuators for Flow Control.” *AIAA Journal*, Vol. 35, No. 5, 1997, pp. 832–837. https://doi.org/10.2514/2.7454.

[2] Glezer, A., and Amitay, M. “Synthetic Jets.” *Annual Review of Fluid Mechanics*, Vol. 34, 2002, pp. 503–529. https://doi.org/https://doi.org/10.1146/annurev.fluid.34.090501.094913.

[3] Zong, H., Chiatto, M., Kotsonis, M., and de Luca, L. “Plasma Synthetic Jet Actuators for Active Flow Control.” *Actuators*, Vol. 7, No. 4, 2018, pp. 1–34. https://doi.org/10.3390/act7040077.

[4] Davis, S. A., and Glezer, A. “Mixing Control of Fuel Jets Using Synthetic Jet Technology: Velocity Field Measurements.” *37th Aerospace Sciences Meeting and Exhibit*, No. c, 1999. https://doi.org/10.2514/6.1999-447.

[5] Wang, P., and Shen, C. “Characteristics of Mixing Enhancement Achieved Using a Pulsed Plasma Synthetic Jet in a Supersonic Flow.” *Journal of Zhejiang University: Science A*, Vol. 20, No. 9, 2019, pp. 701–713. https://doi.org/10.1631/jzus.A1900130.

[6] Arshad, A., Jabbal, M., and Yan, Y. “Synthetic Jet Actuators for Heat Transfer Enhancement – A Critical Review.” *International Journal of Heat and Mass Transfer*, Vol. 146, 2020, p. 118815. https://doi.org/10.1016/j.ijheatmasstransfer.2019.118815.

[7] Sharma, P., Singh, P. K., Sahu, S. K., and Yadav, H. “A Critical Review on Flow and Heat Transfer Characteristics of Synthetic Jet.” *Transactions of the Indian National Academy of Engineering*, Vol. 7, No. 1, 2022, pp. 61–92. https://doi.org/10.1007/s41403-021-00264-5.

[8] Van Buren, T. “SYNTHETIC JET ACTUATOR PERFORMANCE.” Vol. 2013, No. April, 2013.

[9] Van Buren, T., Whalen, E., and Amitay, M. “Achieving a High-Speed and Momentum Synthetic Jet Actuator.” *Journal of Aerospace Engineering*, Vol. 29, No. 2, 2016, pp. 1–16. https://doi.org/10.1061/(ASCE)AS.1943-5525.0000530.

[10] Van Buren, T., Whalen, E., and Amitay, M. “Synthetic Jet Actuator Cavity Acoustics : Helmholtz Versus Quarter-Wave Resonance.” *Journal of Vibration and Acoustics*, Vol. 137, No. October 2015, 2015, pp. 1–5. https://doi.org/10.1115/1.4030216.

[11] Ingård, U., and Labate, S. “Acoustic Circulation Effects and the Nonlinear Impedance of Orifices.” *The Journal of the Acoustical Society of America*, Vol. 22, No. 2, 1950, pp. 211–218. https://doi.org/https://doi.org/10.1121/1.1906591.

[12] Smith, B. L., and Glezer, A. “Jet Vectoring Using Synthetic Jets.” *Journal of Fluid Mechanics*, Vol. 458, 2002, pp. 1–34. https://doi.org/10.1017/S0022112001007406.

[13] Gallas, Q., Holman, R., Nishida, T., Carroll, B., Sheplak, M., and Cattafesta, L. “Lumped Element Modeling of Piezoelectric-Driven Synthetic Jet Actuators.” *AIAA Journal*, Vol. 41, No. 2, 2003, pp. 240–247. https://doi.org/10.2514/2.1936.

[14] Persoons, T. “General Reduced-Order Model to Design and Operate.” *AIAA Journal*, Vol. 50, No. 4, 2012, pp. 916–927. https://doi.org/10.2514/1.J051381.

[15] McCormick, D. C. “Boundary Layer Separation Control with Directed Synthetic Jets.” *38th Aerospace Sciences Meeting and Exhibit*, No. January, 2000. https://doi.org/10.2514/6.2000-519.

[16] Sharma, R. N. “Fluid-Dynamics-Based Analytical Model for Synthetic.” *AIAA Journal*, Vol. 45, No. 8, 2007, pp. 1841–1847. https://doi.org/10.2514/1.25427.

[17] de Luca, L., Girfoglio, M., and Coppola, G. “Modeling and Experimental Validation of the Frequency Response of Synthetic Jet Actuators.” *AIAA Journal*, Vol. 52, No. 8, 2014, pp.

1733–1748. https://doi.org/10.2514/1.J052674.

[18] Housley, K. W., Clingman, D. J., and Amitay, M. Development of Piezoelectric-Based Membranes for Synthetic Jet Actuators: Experiments and Modeling. No. 9801, S. F. Griffin, ed., 2016, pp. 1–12.

[19] Prasad, S. A. N., Sankar, B. V, Cattafesta, L. N., Horowitz, S., Gallas, Q., Sheplak, M., and Denver, A. "Two-Port Electroacoustic Model of an Axisymmetric Piezoelectric Composite Plate 43rd AIAA / ASME / ASCE / AHS / ASC Structures , Structural Dynamics , and Materials Conference." *Methods*, No. April, 2002, pp. 0–9.

[20] de Luca, L., Girfoglio, M., Chiatto, M., and Coppola, G. "Scaling Properties of Resonant Cavities Driven by Piezo-Electric Actuators." *Sensors and Actuators, A: Physical*, Vol. 247, 2016, pp. 465–474. https://doi.org/10.1016/j.sna.2016.06.016.

[21] Chiatto, M., Capuano, F., Coppola, G., and de Luca, L. "LEM Characterization of Synthetic Jet Actuators Driven by Piezoelectric Element : A Review." *Sensors*, Vol. 17, No. 6, 2017. https://doi.org/10.3390/s17061216.

[22] Chiatto, M., Palumbo, A., and de Luca, L. "Design Approach to Predict Synthetic Jet Formation and Resonance Amplifications." *Experimental Thermal and Fluid Science*, Vol. 107, No. May, 2019, pp. 79–87. https://doi.org/10.1016/j.expthermflusci.2019.05.013.

[23] Rayleigh, J. W. S. B. Theory of Resonators. In *The Theory of Sound*, 1896, pp. 170–235.

[24] Alster, M. "Improved Calculation of Resonant Frequencies of Helmholtz Resonators." *Journal of Sound and Vibration*, Vol. 24, No. 1, 1972, pp. 63–85. https://doi.org/https://doi.org/10.1016/0022-460X(72)90123-X.

[25] Tang, P. K., and Sirignano, W. A. "Theory of a Generalized Helmholtz Resonator." *Journal of Sound and Vibration*, Vol. 26, No. 2, 1973, pp. 247–262. https://doi.org/10.1016/S0022-

460X(73)80234-2.

[26] Panton, R. L., and Miller, J. M. “Resonant Frequencies of Cylindrical Helmholtz Resonators.” *Journal of the Acoustical Society of America*, Vol. 57, No. 6, 1975, pp. 1533–1535. https://doi.org/10.1121/1.380596.

[27] Chanaud, R. C. “Effects of Geometry on the Resonance Frequency of Helmholtz Resonators.” *Journal of Sound and Vibration*, Vol. 178, No. 3, 1994, pp. 337–348. https://doi.org/10.1006/jsvi.1994.1490.

[28] Dickey, N. S., and Selamet, A. “HELMHOLTZ RESONATORS: ONE-DIMENSIONAL LIMIT FOR SMALL CAVITY LENGTH-TO-DIAMETER RATIOS.” *Journal of Sound and Vibration*, Vol. 195, No. 3, 1996, pp. 512–517. https://doi.org/https://doi.org/10.1006/jsvi.1996.0440.

[29] Gil, P., and Wilk, J. “Helmholtz Resonance Frequency of the Synthetic Jet Actuator.” *Applied Sciences*, 2021, pp. 1–17. https://doi.org/https://doi.org/10.3390/app11125666.

[30] COMSOL Multiphysics® v. 5.4. Introduction to the Acoustics Module. https://doc.comsol.com/5.4/doc/com.comsol.help.aco/IntroductionToAcousticsModule.pdf.

[31] White, F. M. Viscous Flow in Ducts. In *Fluid Mechanics* (J. P. Holman and J. Lloyd, eds.), McGraw-Hill, 1998, pp. 371–373.

[32] Persoons, T., Donovan, T. S. O., Persoons, T., and Donovan, T. S. O. “A Pressure-Based Estimate of Synthetic Jet Velocity.” *Physics of Fluids*, Vol. 19, No. 12, 2007. https://doi.org/10.1063/1.2823560.

Chapter 6: Conclusion

This chapter summarizes the dissertation's key research findings and contributions. This dissertation addressed key issues for modeling ferroelectric materials and synthetic jet actuators. Ferroelectric materials have electromechanical coupling that allows them to function as transducers, actuators, and sensors necessary for many devices. Relaxor ferroelectrics like PMN-PT and PIN-PMN-PT can exhibit especially high dielectric and electromechanical properties that make them desirable for applications that require greater output than conventional ferroelectrics such as PZT. However, ferroelectric phase field models have been unable to accurately capture certain phenomena such as polarization reorientation and phase transitions. This work offers potential solutions on how to improve ferroelectric phase field models (both relaxor and non-relaxor) without becoming computationally cost-prohibitive.

Chapter 3 of the dissertation analyzed the effect of fluctuations/biases, energy barriers and metastability on phase transformations. As part of this work, an improved energy function was developed for a composition of rhombohedral PIN-PMN-PT near the MPB that remains thermodynamically stable for large values of polarization. Landau coefficients were fitted to material data reported in literature for various compositions of room temperature PIN-PMN-PT. Multiple fitting parameters were needed to simulate the phase transitions at the desired temperatures. Using this new energy function, the hysteresis behavior was constructed by analyzing the stable points in the energy landscape under a given load. For the purposes of the study, a metastable well was considered stable if the energy barrier between neighboring wells was higher than the fluctuation energy. This work showed that by accounting for fluctuations (on the order of 1E+4 to 1E+5 J/m^3 for PIN-PMN-PT), the simulated hysteresis based on stable wells predict behavior similar to what has been observed experimentally. This included the lower

coercive field for switching and the forward and reverse phase transformations as a load is applied and released that have been reported in literature.

Chapter 4 applied the findings of Chapter 3 to a finite-element phase-field model and sought evaluate various ways to implement fluctuations and/or biases that would allow the model to escape metastable wells. A couple models have reported closer agreement with predicted and measured switching fields after accounting for defects and thermal noise. Two main methods of implementation for the fluctuations/biases were evaluated: 1) as time-varying noise and 2) as static random electric fields. Adding fluctuations as a time-varying noise to the TDGL equation did allow for the model to escape metastable states but introduced issues with reproducibility and significantly increased computational time because the model does not reach convergence even for simple cases. For these reasons, this approach is not recommended unless the purpose of a study is primarily to investigate time-dependent effects of fluctuations. In contrast, implementing fluctuations as static electric fields on the order of 1 MV/m allowed the model to escape the metastable and unstable equilibrium states that models typically get trapped in. With this implementation, the model was able to reproduce the electric-induced and stress-induced phase transformations observed in experiments by adjusting the size and strength of the random fields. Relaxor characteristics arise when the local random fields are both strong and small in size relative to the RVE. Nanodomains are more likely to nucleate from these areas and there is a more gradual phase transition starting from these nucleation points. On the other hand, if the local random fields are weak and large relative to the RVE, there will be relatively little relaxor characteristics in the mode. The local fields do not overcome the penalty introduced by the gradient energy, and the RVE will uniformly transition once a critical external field is reached. Based on this work, it is suggested to implement fluctuations as weak random fields with some long range order. The

longer-range effects introduced by the fields in an RVE can be compensated during if the bias introduced is known or averaged by simulating many random seeds. Implementing fluctuations in this manner may help material scientists engineer hysteresis loops for specific applications if the density, strength, direction of local fields can be manipulated in the crystal.

Chapter 5 shifted from modeling ferroelectric materials on the mesoscale level to the macroscale (bulk) level in a piezoelectrically-driven synthetic jet actuator device. This work identified and addressed key issues in modeling synthetic jet actuators, particularly for SJAs that deviate from the ideal Helmholtz resonator. Large discrepancies have been reported between the predicted and measured performance of thin piezoelectric SJAs. While LEMs have been shown to be capable of good agreement with ideal Helmholtz resonators, these models require fitting multiple parameters for the diaphragm and losses to the experimental data and were restricted to ideal Helmholtz resonators. Current models lack predictive capabilities for modeling novel diaphragm or cavities. This was addressed by combining FEM and LEM techniques. Bulk properties are used in the FEM model to predict the piezoelectric diaphragm's deformation and a formula was derived to estimate the loss coefficient. A separate FEM acoustics model was used to calculate the cavity's acoustic resonance that should be used in place of the Helmholtz resonance in the lumped equations. This method was shown to provide good agreement with experimental results for the SJA geometries tested. Furthermore, it showed that the volume occupied by the piezoelectric disks in the cavity has a significant effect on the performance of ultrathin SJAs. This combined model provides a way to more accurately and efficiently explore novel diaphragm and cavity designs without resorting to full-ordered models that are computationally expensive.

The models presented in this dissertation provide valuable insights into understanding the underlying mechanisms that drive phase transformation in ferroelectric materials and the

performance of piezoelectric synthetic jet actuators. Key contributions of this work for ferroelectric material modeling include:

- An improved energy function that can simultaneously the R, O, and T phases.
- Recommendations to efficiently implement fluctuations in phase-field models.

The combination of these contributions allows the model to simulate phenomena that previously were not successfully captured, particularly the forward and reverse R-O-R phase transformations and hysteresis reported in literature.

Key contributions for synthetic jet actuators modeling:

- An approach to model novel SJAs by combining finite-element and lump-element techniques.
- Formula to estimate the loss coefficient based on the cavity and orifice geometries.

While not part of the scope of this dissertation, this work provides a strong foundation to investigate the following research questions:

- Can the energy function for PIN-PMN-PT be modified to account for composition changes in PIN, PMN, and/or PT?
- How do the stiffness and electrostrictive coefficients affect phase stability and hysteresis? Can these properties be used to tune the hysteresis and other phenomena such as phase coexistence?
- How do the mobility and gradient coefficients affect domain formation and motion in the context of phase transformations?
- How can the nonuniform strains due to local fields/defects be controlled? Can the variations in the phase field model due to random seeds phase field model predict a device's reliability?

- The macro- and meso-scale models can be combined to complement one another for optimization. For example, mesoscale material models can output bulk properties to use in macroscale device models, and vice versa. Macroscale device models can be used to provide goals for material developments.